First-principles study of defects in GaN, AlN and their alloys

Final Report

Period covered: June 2009 – May 2010

Prepared by

Prof. Dr. Sukit Limpijumnong (P.I.)

and graduate students

Suranaree University of Technology,

Nakhon Ratchasima 30000

sukit@sut.ac.th

For the

AFOSR/AOARD

Contract # FA2386-09-1-4106

1. REPORT DATE **31 AUG 2010**	2. REPORT TYPE **FInal**	3. DATES COVERED **07-05-2009 to 06-05-2010**
4. TITLE AND SUBTITLE **First-principles study of defects in GaN, AlN and their alloys**		5a. CONTRACT NUMBER **FA23860914106**
		5b. GRANT NUMBER
		5c. PROGRAM ELEMENT NUMBER
6. AUTHOR(S) **Sukit Limpijumnong**		5d. PROJECT NUMBER
		5e. TASK NUMBER
		5f. WORK UNIT NUMBER
7. PERFORMING ORGANIZATION NAME(S) AND ADDRESS(ES) **National Synchrotron Research Center, Suranaree University of Technology ,P.O. Box 93,Nakhon Ratchasima 30000,Thailand,TH,93**		8. PERFORMING ORGANIZATION REPORT NUMBER **N/A**
9. SPONSORING/MONITORING AGENCY NAME(S) AND ADDRESS(ES) **AOARD, UNIT 45002, APO, AP, 96337-5002**		10. SPONSOR/MONITOR'S ACRONYM(S) **AOARD**
		11. SPONSOR/MONITOR'S REPORT NUMBER(S) **AOARD-094106**

12. DISTRIBUTION/AVAILABILITY STATEMENT **Approved for public release; distribution unlimited**

13. SUPPLEMENTARY NOTES

14. ABSTRACT

We employed first principles calculations with supercell approach to study various defects in AlN, GaN, InN, related wide gap semiconductors, and their alloys. For the exchange and correlation functions, we used both the standard local density approximations (or generalized gradient approximations) and time consuming HSE hybrid functional which can provide electronic band gaps that are much closer to the experimental values. The later is being used when more accurate determination of defect levels is needed. In this program, we also employed the FEFF codes, which is the software specially designed for the simulation of the x-ray absorption spectrum, to allow a direct comparison between our crystal structure models and actual measurements. We have accomplished several important results. a) We reconfirm our earlier calculations that Mg and Be are deep acceptors in AlN by using HSE hybrid functional which does not suffer from band gap underestimation problems. b) We calculated Al Frenkel pairs (interstitial Al and Al vacancy pairs) in AlN. Both the stability and the structure are very similar to the case of Ga Frenkel pairs in GaN that we have studied last year. We also found that the barrier for the pair to recombine is ~0.2 eV which is very small (similar to the case of GaN), making the pairs unlikely to be stable at room temperature. c) We studied the x-ray absorption spectrum of InN and In2O3 alloys. Special attentions have been paid to understand the source of the features in the calculated XANES.

15. SUBJECT TERMS **condensed matter physics, defects in semiconductor, III-N Compounds**

16. SECURITY CLASSIFICATION OF:			17. LIMITATION OF ABSTRACT	18. NUMBER OF PAGES	19a. NAME OF RESPONSIBLE PERSON
a. REPORT **unclassified**	b. ABSTRACT **unclassified**	c. THIS PAGE **unclassified**	**Same as Report (SAR)**	**65**	

<u>Executive summary</u>

We employed first principles calculations with supercell approach to study various defects in AlN, GaN, InN, related wide gap semiconductors, and their alloys. For the exchange and correlation functions, we used both the standard local density approximations (or generalized gradient approximations) and time consuming HSE hybrid functional which can provide electronic band gaps that are much closer to the experimental values. The later is being used when more accurate determination of defect levels is needed. In this program, we also employed the FEFF codes, which is the software specially designed for the simulation of the x-ray absorption spectrum, to allow a direct comparison between our crystal structure models and actual measurements. We have accomplished several important results. a) We reconfirm our earlier calculations that Mg and Be are deep acceptors in AlN by using HSE hybrid functional which does not suffer from band gap underestimation problems. b) We calculated Al Frenkel pairs (interstitial Al and Al vacancy pairs) in AlN. Both the stability and the structure are very similar to the case of Ga Frenkel pairs in GaN that we have studied last year. We also found that the barrier for the pair to recombine is ~0.2 eV which is very small (similar to the case of GaN), making the pairs unlikely to be stable at room temperature. c) We studied the x-ray absorption spectrum of InN and In_2O_3 alloys. Special attentions have been paid to understand the source of the features in the calculated XANES. We found that the XANES spectrum of In in the In_2O_3 structure is very different from that of In in wurtzite. We have also studied the effects of interchanging the anions (O by N or *vice versa*). To understand the source of the changes in the XANES spectra in each case, the decomposed electron density of states were studied. d) We have studied hydrogen in In_2O_3. In most semiconductors, H is amphoteric, i.e. can act as donor or acceptor to counteract leading carriers. However, for In_2O_3, we found that H_i is exclusively a shallow donor (similar to the case of ZnO). In addition, H atoms can also occupy substitutional oxygen sites (H_O) and act exclusively as donors in this configuration. Our findings confirm that hydrogen acts as a source of *n*-type conductivity in In_2O_3. e) The elastic constants and sound velocities in wurtzite GaN and InN as well as other wurtzite semiconductors (SiC, ZnO, and CdSe) as functions of pressure are studied. We showed that the elastic constants are lower in materials with higher ionicity. Generally, the sound

velocities follow the same trend as the elastic constants. f) When ZnO is doped with large group V anions, such as P, As or Sb, phase precipitations might occur. This is mainly because of the large site mismatched and the high concentration of the dopant. We studied the electric properties at the Zn_3P_2 and ZnO interface and found that a layer of hole could be formed. This layer could give the p-type carrier in the measurements. g) Recently, experimentalists measured the local vibration modes of O doped CdTe and found two sets of frequencies, i.e. one line at 350 cm^{-1} and another set of two lines at ~ 1100 cm^{-1}. The 350 cm^{-1} has been assigned to O substituted for Te (O_{Te}) and the high frequency lines (~1100 cm-1) have been assigned to the vibration associated with O_{Te}-V_{Cd} complexes. Our calculations showed that the assignment of the 350 cm^{-1} mode is correct. However, the O_{Te}-V_{Cd} complexes can give the highest frequency of only ~460 cm^{-1}, which is far smaller than the observed 1100 cm^{-1}. Therefore, the 1100 cm^{-1} mode can not come from O_{Te}-V_{Cd} complexes. h) For first principles computations of alloy systems, generally a supercell approach is used. We investigated the size of unit cell that can sufficiently give the reliable results. In this work, the quaternary alloys $Al_xGa_yIn_{1-x-y}P$ are used for the test. We found that at least the supercell size with five cation atoms (including all cell shapes) has to be used to obtain reasonable results.

Publications in refereed journals (6):

1) "*Alternative sources of p-type conduction in acceptor-doped ZnO*"
   S. Limpijumnong, L. Gordon, M. Miao, A. Janotti, and C.G. Van de Walle
   Appl. Phys. Lett. **97**, 072112 (2010).

2) "*Pressure-dependent elastic constants and sound velocities of wurtzite SiC, GaN, InN, ZnO and CdSe and their relation to phase transition: First-principles study*"
   K. Sarasamak, S. Limpijumnong, and W.R. L. Lambrecht
   Phys. Rev. B **82**, 035201 (2010).

3) "*X-ray absorption spectroscopy of indium nitride, indium oxide, and their alloys*"
   J. T-Thienprasert, S. Rujirawat, J. Nukeaw and S. Limpijumnong
   Comput. Mater. Sci. **49**, S37 (2010).

4) "*Vibrational signatures of O_{Te} and O_{Te}-V_{Cd} in CdTe: A first-principles study*"
   J. T-Thienprasert, S. Limpijumnong, A. Janotti, C.G. Van de Walle, L. Zhang, M.-H. Du and D.J. Singh
   Comput. Mater. Sci. **49**, S242 (2010).

5) "*The effects of unit cell size on the bandgap range in the direct enumeration study of $Al_xGa_yIn_{1-x-y}P$ alloys*"
S. Jungthawan, K. Kim and S. Limpijumnong
Comput. Mater. Sci. **49**, S114 (2010).

6) "*Hydrogen doping in indium oxide: An ab initio study*"
S. Limpijumnong, P. Reunchan, A. Janotti, and C.G. Van de Walle
Phys. Rev. B **80**, 193202 (2009).

(Following work schedule and milestones are the same as previously submitted)

Work schedule:

Month 0:

- o Start calculations of V_N and N_i and p-dopants (especially, Mg and Be) in AlN and AlGaN using first principles supercell approach. Mg and Be are potential p-dopant for AlN and AlGaN alloys.

- o Start calculations of defect complexes between native defects and dopants in GaN, AlN, and related wide-gap materials.

- o Investigating various possible defect-complex configurations to identify the most probable ones.

Month 6:

- o Study stable defects and defect complexes in deeper details. Certain signatures of them will be simulated for comparison with experiments.

- o Start calculations of Frenkel pair formation between V_N and N_i by directly calculations of the energy as a function of pair distance using nudge elastic band method.

<u>Milestones:</u>

6 month:

- o Obtained the results of at least one native defect in AlGaN alloy.

- o Obtained the results of at least one defect complex in GaN or AlN or related wide gap materials.

- o Obtained preliminary results on the complex between some native defects and *p*-dopants.

12 month:

- o Complete results on V_N and N_i in AlN and/or AlGaN alloy. Some preliminary results on the V_N and N_i Frenkel pair in AlN will be obtained.

- o Results on the binding energies and stabilities of V_N-N_i Frenkel pairs as a function of the pair-distance.

- o Signatures for comparison with experimental measurements of some interesting defects and dopants in AlN, AlGaN alloys and related wide-gap materials.

Research Activities

Computational methods and codes

To study the electronic as well as other properties of these semiconductor systems, we employed first-principles calculation approach. Most of our calculations are based on density-functional theory and *ab initio* projector-augmented wave potentials as implemented in the VASP code [1]. Generally, either the local density approximation (LDA) or the generalized gradient approximation (GGA) of the Perdew, Burke, and Ernzerhof (PBE) [2] are used for the exchange-correlation functions. These functional are known to greatly underestimate the band gap. In some cases where the more correct electronic band gap is desired, we use the hybrid functional as proposed by Heyd, Scuseria, and Ernzerhof (HSE) [3] which is much more computational demanding. A screening parameter of $\mu = 0.2$ Å^{-1} is used for the screened non-local exchange [4]. The hybrid functional is a mixture of 25% Hartree-Fock exchange functional and 75% PBE exchange functional. For the x-ray absorption spectroscopy (XAS) simulation, we use the *ab initio* multiple scattering code called FEFF (version 8.2) [5]. Because the FEFF code cannot optimize the crystal structures, for the XAS simulation of local structures such as impurities and alloys, it is important that atomic relaxations have to be performed using the first principles calculations (VASP) before importing the coordinates into FEFF. Depending on the nature of each system studied, the specific computational details are varied but can be found in each attached publication.

Computational approach to study defects in semiconductor crystal

Bulk semiconductor crystal is an ideal case for performing calculations because the system can be defined by the smallest possible unit cell that repeated periodically in all directions by the three translation vectors. The highly ordered repetition of the unit cell is an important factor that defines the electronic properties of semiconductor crystals. For bulk systems, the calculations are done at the infinite repetitions of the unit cell. This is highly realistic because in actual crystal systems the number of atoms is in the order of 10^{23}. Although, there is virtually unlimited number of atoms, in practice we do not need to repeat the calculation for every unit cells. We use the Bon von Karman boundary conditions and perform the calculation on only a single unit cell which most of the time composed of 4 atoms or less. For defect or impurity study, the situation is different. Majority of the crystal is still highly periodic with a small number of defects (or impurities) scattered in the crystal interrupting the periodicity. All atoms in the system are no longer equivalent and, in principle, each and every atom has to be calculated separately. This is prohibitively demanding in terms of computation. To reduce the problem into a manageable one, the supercell approach is used.   In the supercell approach, the unit cell is repeated a few times in each direction to create a larger cell (called supercell) which serves as a new unit cell. For example, the 72 atom supercell is a result of the repetition of the 4 atom wurtzite unit cell three times each in $\mathbf{a_1}$ and $\mathbf{a_2}$ directions and two times in $\mathbf{a_3}$ direction; leading to the multiplication factor of $3\times3\times2 =$ 18. This new unit cell has a new three translation vectors, i.e. $3\mathbf{a_1}$, $3\mathbf{a_2}$ and $2\mathbf{a_3}$.   To study a defect, a defect is created in this supercell. Of course, the defect is also repeated as the supercell repeats; resulting in an unusual high defect concentration compared to reality. Therefore, it is desirable to use the supercell size as large as computationally possible to study defects that are generally of low concentrations. In practice, the supercell size as small as 72 or even 36 atom can already provide reasonable results. In this study, we generally use a supercell size of 96 atoms for the wurtzite crystal and 64 atoms for zincblende crystal. We used a set of non-Γ k-points sampling and plane wave cut-off of 400 eV for the plane wave basis set. In supercell calculations, the formation energy of a defect X in charge state q is defined as

$$E^{f}[X^{q}] = E_{tot,SC}(X^{q}) - E_{tot,SC}(bulk) + n_{\alpha}\mu_{\alpha} + qE_{F}, \quad (1)$$

where $E_{tot,SC}(X^{q})$ is the total energy of a supercell containing the defect, $E_{tot,SC}(bulk)$ is the total energy of the same supercell but without any defect. n_{α} is the number of the atoms of specie α being removed from (positive value) or added to (negative value) a bulk supercell to form defect X. μ_{α} is the reservoir energy of specie α (the chemical potential). E_{F} is the Fermi level, referenced to the valence-band maximum of bulk, E_{v}. The chemical potentials in Eq. (1) depend on the growth conditions and constrained by phase precipitation limits.

As an example we can look at the case of Mg substitution Al in AlN. Under Al-rich condition, the chemical potential of Al is set at the highest value possible which is $\mu_{Al} = \mu_{Al[metal]}$ = formation energy of solid metal Al (if μ_{Al} is higher than this value, the Al metal will be form on the sample instead of AlN). In order for AlN to be stable during the growth, it is required that $\mu_{Al} + \mu_{N} = \mu_{AlN}$ = heat of formation of AlN. This fixes $\mu_{N} = \mu_{AlN} - \mu_{Al}$. The chemical potential of Mg is set at the highest value possible, i.e. the formation energy of metal Mg ($\mu_{Mg} = \mu_{Mg[metal]}$). The formation energy of Mg_{Al} in charge state q is defined as

$$E^{f}(Mg_{Al}^{q}) = E_{tot,SC}(Mg_{Al}^{q}) - E_{tot,SC}(bulk) + \mu_{Al} - \mu_{Mg} + qE_{F} \quad \ldots(2)$$

Magnesium and beryllium doped AlN

Group-II metals such as Mg and Be are shallow acceptors when substituting for Ga in GaN. Magnesium has been used successfully to dope GaN into *p*-type; leading to commercial blue lasers in today devices [6-8]. We have previously suggested based on first principles calculations that beryllium is a potentially good *p*-type dopant in GaN [9]. However, beryllium can potentially form interstitial (Be_{int}) and bind with the substitutional acceptor (Be_{Ga}) turning the acceptor into a single donor. Previously, we suggested that if one can overcome interstitial Be problem, beryllium is a potentially better acceptor in GaN than Mg [9]. Currently the interests have shifted to AlN. With a larger band gap of 6.2 eV, AlN is a potential material for UV optoelectronic applications. However, AlN is naturally *n*-type and *p*-type AlN is currently unavailable. Similar to other wide gap semiconductors, AlN also suffers from doping asymmetry, i.e. easy to be doped into one conducting type (*n*-type) than another (*p*-type) [10, 11]. There are also some preliminary theoretical investigations of doping in AlN [12-14]. Because the lattice constant of AlN is very similar to that of GaN, both Mg and Be are potential candidates as for *p*-type doping in AlN. Recent experimental results showed that Mg is a deep acceptor in AlN (with ionization energy of around 0.4 – 0.6 eV) [15]. In our previous program, both Mg and Be as dopants in AlN have been studied by using DFT-LDA. Our results also showed that both Mg and Be are deep acceptor in AlN with the ionization energy of ~0.6 eV. In addition, we also found that interstitial Mg and Be (Mg_{int} and Be_{int}) have rather low formation energy and can cause spontaneous compensation especially for the case of Be. It is known that DFT-LDA or DFT-GGA largely underestimate semiconductor band gaps. This could potentially cause wrong determination of dopant ionization energies. To ensure the validity of the DFT-LDA results, in this program we studied Mg and Be doped AlN by using HSE hybrid functional which gives band gap in good agreement with the experiment.

Table I shows the lattice parameters and band gap values obtained from DFT-LDA, DFT-GGA and HSE in comparison with experiments. All calculations gave reasonable lattice parameters with the experimental values. However, only the HSE calculations gave the electronic band gap in agreement with the experimental values (to

within 10%). As a result, the formation energies as well as the ionization energy of impurities and defects in AlN calculated by HSE are expected to be more reliable.

Table I The equilibrium lattice parameters of wurtzite-AlN (*a* and *c/a*) and the band gap (E_g) given by LDA and GGA-PBE and HSE for the exchange-correlation functional. The experimental values are taken from Ref. [16].

	LDA	GGA-PBE	HSE	Exp.
a (Å)	3.091	3.131	3.102	3.112
c/a	1.600	1.605	1.603	1.609
E_g (eV)	4.37	4.02	5.64	6.20

Figure 1 shows the local atomic structures of Mg_{Al} and Be_{Al} (for the −1 charge state). All four Mg-N bonds have almost the same length of ~2.01 Å which is about 5% larger than the Al-N bond length of 1.89 Å. On the other hand, all four Be-N bonds (~1.83 Å) are slightly smaller than the Al-N bond length. This can be attributed to the fact that Mg atom has larger radii than that of Al atom, making the surrounding N atoms relax outward while Be atom has smaller radii than that of Al atom, making surrounding N atoms relax inward.
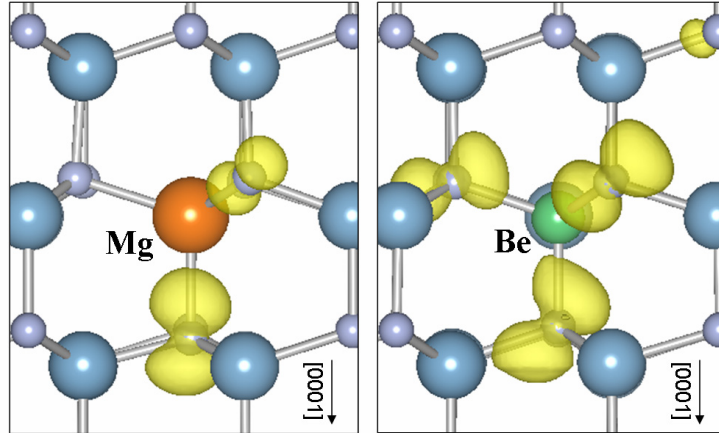

Fig. 1 Local atomic geometry of Mg_{Al} and Be_{Al} in wurtzite AlN. The large blue spheres are Al atoms and the small light blue spheres are N atoms. The isosurface charge density of the Mg and Be related state is also illustrated.

The formation energies of Mg_{Al} and Be_{Al} are shown in Fig 2. The formation energies obtained by HSE calculations are turned out to be in agreement with the values

obtained earlier by using DFT-LDA to within 0.5 eV (not shown). This indicated that our earlier results were sufficiently reliable. The acceptor ionization energy is defined as the value of the Fermi level where the Mg_{Al} (or Be_{Al}) in neutral and -1 charge states have the same formation energy. From HSE calculations, we obtained the ionization energy of 0.43 and 0.72 eV for Mg_{Al} and Be_{Al}, respectively. These reconfirmed that both Mg_{Al} and Be_{Al} are deep acceptors in AlN. Our ionization energies are in a reasonable agreement with the values by Gali *et al.* [14] (0.50 eV for Mg_{Al} and 0.97 eV for Be_{Al}) that are also obtained by HSE calculations but with a different supercell size. At this point, both of experimental and theoretical studies indicated that Mg_{Al} and Be_{Al} are not good candidates for *p*-type doping in AlN. Therefore, different approaches shall be taken. One of the top on the list is by co-doping which Gali et al. already suggested a possible reduction in the ionization energy with Mg and O co-doping that could lead to Mg_{Al}-O_N-Mg_{Al} complexes.
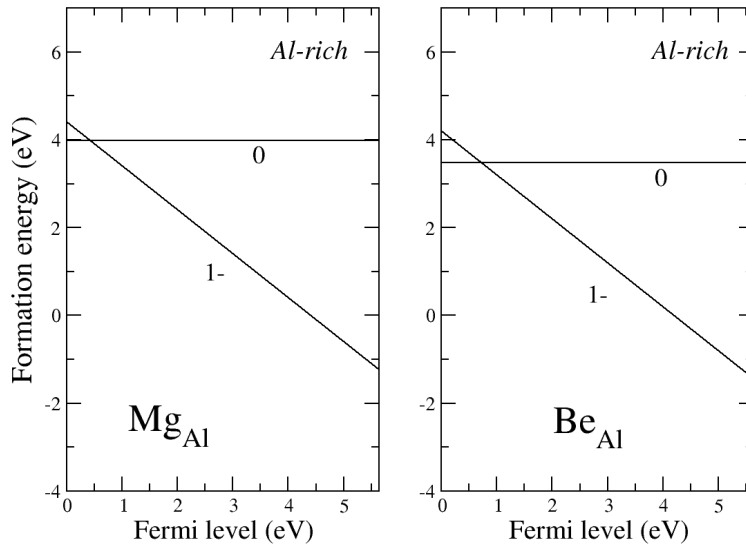

Fig. 2 Formation energy as a function of Fermi level for Mg_{Al} and Be_{Al} in wurtzite AlN under Al-rich conditions. The Fermi level is shown in the range from 0 to 5.64; corresponding to the HSE calculated band gap of AlN. The crossing point between the 0 and -1 charge state defines the ionization energy.

Interstitial aluminum and aluminum vacancy pairs (Al$_i$-V_{Al}) in AlN

        In the previous program, we have studied the similar type of pairs in GaN, i.e. Ga$_i$-V_{Ga}. These types of defect complexes are called Frenkel pairs which are believed to form when the crystals are irradiated by electrons or particles. This is because, after electron irradiation process, interstitials and the corresponding vacancies are expected. Depending on the energy of the irradiated electron, Al or N can be selectively knocked out of their sites. Since Al$_i$ is a positive center and V_{Al} is a negative center, they attract each other. When they are in an appropriate proximity the pair formation could be expected. There are many experimental works on the electronic and optical properties of samples after electron irradiation in GaN. The attempts to detect these defects have been carried out.[17-21] In our previous program, we studied the $Ga_i - V_{Ga}$ pairs in GaN. We found that Ga$_i$ can occur in 3+, 2+, and 1+ charge states, depending on the Fermi energy of the sample. V_{Ga} can occur in 3−, 2−, 1−, and neutral charge states. Because Ga$_i$ and V_{Ga} have opposite charge, they have Coulom attraction to each other. However, if the two defects are placed next to each other, they are spontaneously recombined. Even if Ga$_i$ is placed at the next nearest neighbor of V_{Ga}, Ga$_i$ can still spontaneously diffuse *via* the kick-out mechanism and the defects are annihilated. The first stable $Ga_i - V_{Ga}$ configuration occurs when the pair is separated by ~ 4 Å along the hexagonal channel in which Ga$_i$ is placed at octahedral site. This configuration was called "1st $Ga_i - V_{Ga}$" in the previous program and will be called Ga-FP(1) here. The next stable configuration with the higher energy [Ga-FP(2)] is found when the Ga$_i$ is placed at the next nearest octahedral site along the hexagonal channel with a distance of 6.4 Å away from the ideal V_{Ga} position. These two pairs have the binding energy (compared the energy of the pair to the separated Ga$_i$ and V_{Ga}) of 3.3 and 2.4 eV, respectively. We found that for further separation, the binding energy is immediately reduced to the order of 0.1 eV.

        In this program, we performed similar study in the case of AlN. Electron irradiation experiments are one of the important means to intentionally create defects in nitrides and oxides [17, 22]. Since the created defects can be both interstitials and vacancies, i.e., Al$_i$, N$_i$, V_{Al} and V_N. In this program, we study the Al-Frenkel pairs (Al-

FPs) which consist of Al_i and V_{Al}. We applied the density functional theory (DFT), as implemented in the VASP code [1] with local density approximation (LDA) in our calculations. The interaction between ions and electrons is described using the projector augmented wave method [23]. The cutoff energy for plane-wave expansion of 400 eV is used. The 96-atom supercell is employed for simulation of defects and the shifted 2×2×2 grid of Monk-Horst Pack special k point is used for integrations over the Brillouin zone. All atoms in supercell are relaxed until the residual force is less than 0.01 eV/Å. All calculations were performed at the calculated lattice constant of bulk wurtzite AlN of $a =$ 3.09 Å and $c/a = 1.600$.
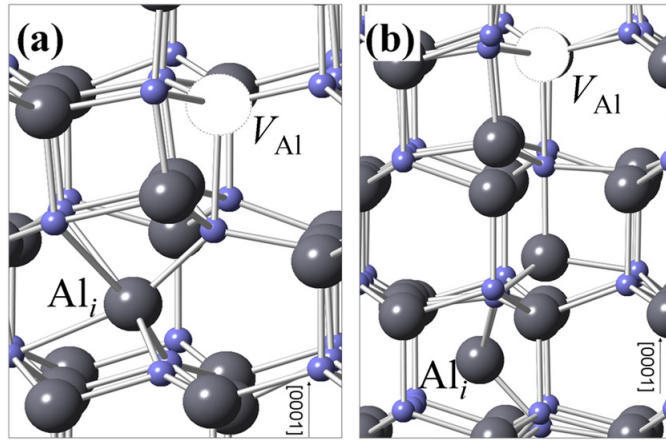

Fig. 3 Local atomic geometry of (a) the closest Al-Frenkel pair [Al-FP(1)] and (b) the further separation Al-Frenkel pair [Al-FP(2)].

Figure 3 (a) shows the local atomic geometry of the first bound Al-Frenkel pair, Al-FP(1) and (b) the second bound Al-Frenkel pair, Al-FP(2) which is slightly higher in energy. The configurations of these two Al-Frenkel pairs are very similar to the corresponding Ga-Frenkel pairs in GaN. Similar to the case of Ga-FP, here, we also observed large relaxations of Al atoms that involve in Frenkel pair stabilization. The formation energies for separated Al_i and V_{Al} as well as Al-FP(1) and Al-FP(2) are shown in Fig. 4. From the formation energy plot, we can see that Al_i is a shallow triple donor. V_{Al} is a deep triple acceptor with the transition levels $\varepsilon(0/-)$, $\varepsilon(-/2-)$ and $\varepsilon(2-/3-)$ at 0.46 eV, 0.82 eV, and 1.22 eV, respectively. The Al-Frenkel pairs can occur in 1+, neutral and 2− charge states. For Al-FP(1), the transition levels $\varepsilon(+/0)$ and $\varepsilon(0/2-)$ are at 0.53 eV and 4.08 eV, respectively. For Al-FP(2), the transition levels $\varepsilon(+/0)$ and $\varepsilon(0/2-)$ are

slightly higher at 0.56 eV and 4.28 eV, respectively. Table II shows the binding energy of Al-Frenkel pairs in neutral charge state. These binding energies are comparable to the case of Ga-FP in GaN. The recombination barrier of Al-FP(1) pair in the neutral charge state is ~0.2 eV which is similar to the recombination barrier for Ga-Frenkel pair in GaN. This suggested that the pair is unstable and would recombine at rather low temperatures.
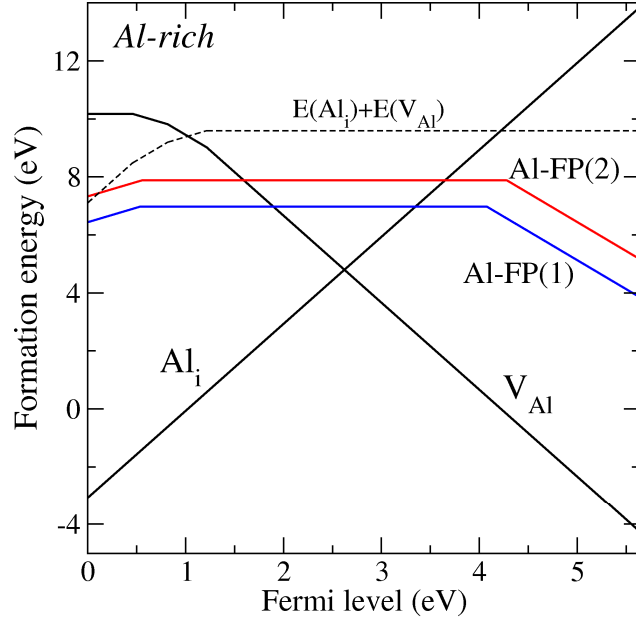

Fig. 4 Formation energies as a function of Fermi level for Al_i, V_{Al}, and Al-Frenkel pairs; Al-FP(1) and Al-FP(2) under Al-rich conditions. The zero of Fermi level corresponds to the top of the valence band. The dash line is the sum of formation energies of the separated Al_i and V_{Al}.

Table II Calculated binding energy of Al-Frenkel pairs (Al-FPs), initial distance (d_{int}) and relaxed distance (d_{rel}) between Al_i and V_{Al} in Al-FP(1) and Al-FP(2)

	E_{bind} (eV)	d_{int} (Å)	d_{rel} (Å)
Al-FP(1)	2.63	3.91	3.78
Al-FP(2)	1.71	6.26	6.16

Resolving the coordination and neighboring species of In in InN and In_2O_3 alloys

      We have previously studied the local structures of indium oxynitride (InO_xN_{1-x}) with varied O contents have been studied by using the combination of first-principles calculations and synchrotron x-ray absorption near edge structures (XANES) [24]. The InO_xN_{1-x} samples were characterized by indium L3-edge XANES measurements at Synchrotron Light Research Institute in Thailand. The measurements were compared favorably with the simulations of wurtzite InN, wurtzite $InN_{0.6}O_{0.4}$, and bixbyite In_2O_3 crystals. Because the spectrum of the sample containing ~40% of O ($InN_{0.6}O_{0.4}$) is almost identical to that of pure InN, we concluded that O can substitute on the N site in the wurtzite structure up to 40% before the crystal structure changed.

      In this program, we focus our attentions on understanding the source of the features in the calculated XANES. In the calculations we have full control to place the neighboring atom around the In and can simulate the spectrum for each case. For wurtzite InN, each In atom is surrounded by four N. When O substitute for N in the wurtzite structure, an In atom can have one, two, three or four O substitute for its N neighbors. We have simulated for each specific case and found that the general features of the spectrum remain similar to that of pure InN except that the first peak becomes lower as more O substitute for N. For In_2O_3 which is a Bixbyite structure, In atoms are surrounded by six O neighbors. We found that the XANES spectrum of In in the Bixbyite structure is clearly differed from that of wurtzite. We have also studied the effects of replacing the O neighbor by N. To understand the source of the changes in the XANES spectra in each case, the decomposed electron density of states are studied. Further details of this work can be found in an attached manuscript [P3].
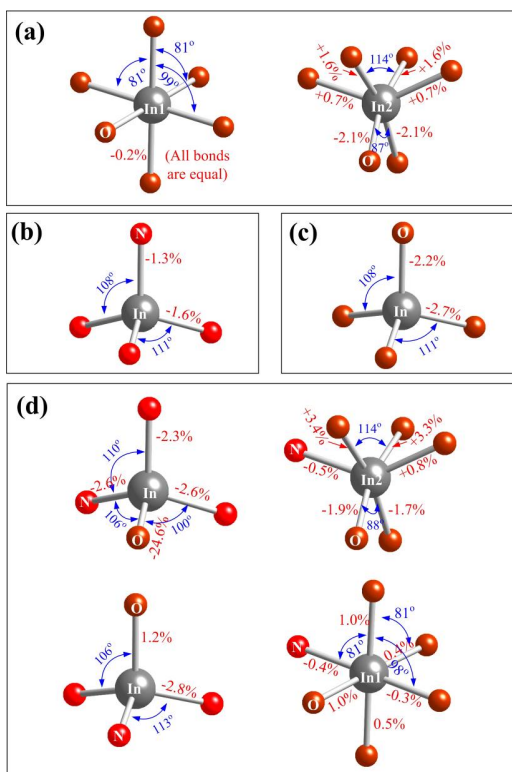
Fig. 5 The local structures around In atoms in (a) bixbyite In_2O_3, (b) wurtzite InN, (c) wurtzite InN with four surrounding N atoms replaced by O atoms, and (d) wurtzite InN with one surrounding N atom replaced by an O atom (left) and bixbyite In_2O_3 with one O atom replaced by a N atom (right). All bond distances are given as a percentage difference from an average In_2O_3 bond distance (d_{calc} = 2.170 Å).
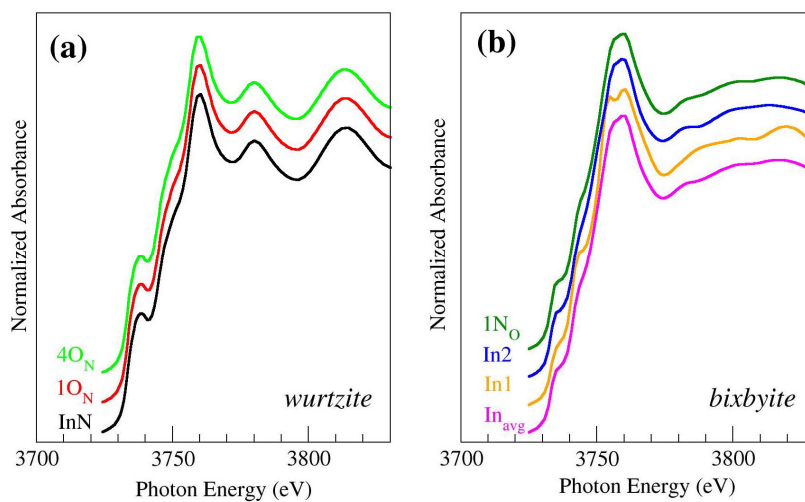

Fig. 6 (a) The simulated In L_3-edge XANES spectra of In atoms in wurtzite InN (bottom), in wurtzite InN with one N replaced by O (middled), and in wurtzite InN with four N replaced by O (top). (b) The spectra In atoms in bixbyite In_2O_3 (bottom three curves) and in bixbyite In_2O_3 with one O replaced by N (top).

<u>Hydrogen in In$_2$O$_3$</u>

In addition to the study of InN and In$_2$O$_3$ alloys, we have also studied H in In$_2$O$_3$ with the final goal to study H in the alloys (H in InN have been previously studied [25]). In$_2$O$_3$ is one of a few transparent materials that can be doped to a very high carrier concentration without significantly degrading their transparencies. The most widely used transparent conductor is tin-doped In$_2$O$_3$, known as Indium Tin Oxide (ITO), which is used as a transparent electrode for optoelectronic devices such as solar cells and light emitting diodes (LEDs). Recently, Koida *et al.* showed that hydrogen-doped In$_2$O$_3$ can have mobility exceeding 100 cm^2/Vs at carrier densities of ~10^{20} cm^{-3} and exhibits good transparency even at near infrared (NIR) wavelengths [26]. In most semiconductors H$_i$ is amphoteric, acting as a donor in *p*-type samples and as an acceptor in *n*-type samples. If H$_i$ is amphoteric, it can never be the cause of conductivity since it self-compensates. There are exceptions, though. For example, in ZnO H$_i$ was proposed, based on first-principles calculations [27], to act exclusively as a donor, a prediction which was soon confirmed by experiments [28]. Whether H is amphoteric impurity like most semiconductors or is acting exclusively as a donor in In$_2$O$_3$ like ZnO, is detrimental for the understanding its conductivity.
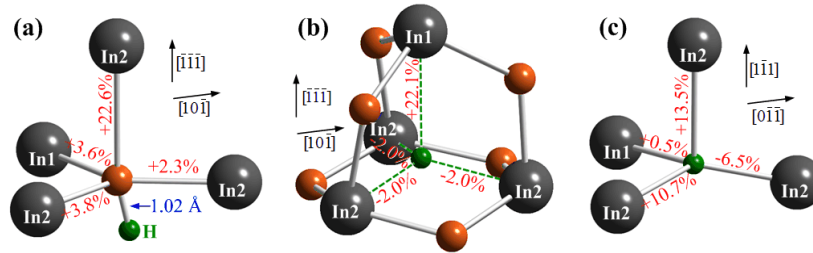

Fig. 7 Schematic illustration of hydrogen defects in In$_2$O$_3$, (a) H$_i^+$ at the oxygen anti-bonding site, (b) H$_i^-$ at the 16*c* site, and (c) H$_O^+$.

In this program, we employed first-principles calculations using density functional theory within the local density approximation (LDA), as implemented in the Vienna *ab initio* simulation (VASP) package [29] to study H in In$_2$O$_3$. Ion-electron interactions were treated using projector augmented wave potentials (PAW) [30]. The electron wave functions were described using a plane-wave basis set with an energy cutoff of 400 eV.

To study H impurities, a supercell approach with the supercell size of 80 atoms was used. We found that H_i is a shallow donor in In_2O_3, and can therefore also be the cause of n-type conductivity (similar to ZnO). In addition, H atoms can also occupy substitutional oxygen sites (H_O) and also act exclusively as donors in this configuration. Substitutional hydrogen was recently described as a multicenter bond and found to be stable in a number of oxides and some nitride materials [31-33]. In order to explore the stability of H_O, we also performed calculations for oxygen vacancies (V_O) in In_2O_3. Our findings confirm that hydrogen acts as source of n-type conductivity in In_2O_3.

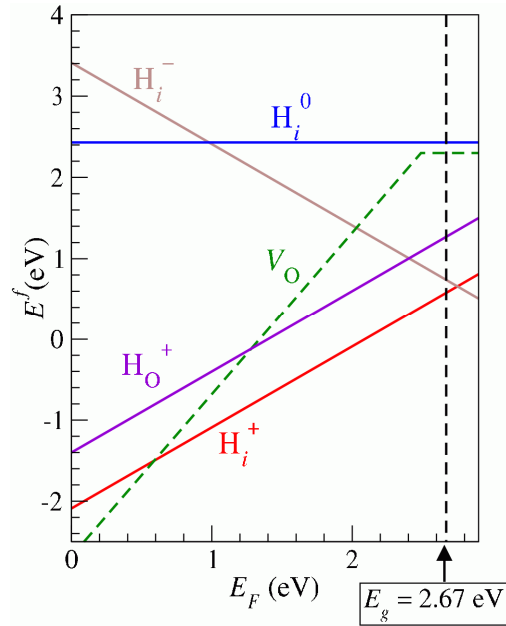Further details of this work can be found in an attached manuscript [P6].

Fig. 8 Calculated formation energies of hydrogen defects and oxygen vacancies in In_2O_3 as a function of Fermi energy. In-rich conditions are assumed.

High pressure study of GaN, InN, and other wurtzite semiconductors

In actual devices, several layers of different semiconductors are generally required to be stacked up together. This often leads to large strain while most of the first principles studies are assumed strain free. In order to pave the way to include strain effects, we study the elastic constants and sound velocities as function of direction and pressure in various wurzite crystals. These include GaN and InN as well as other wurtzite semiconductors, i.e. SiC, ZnO, and CdSe. We did not limit our study to just III-V compounds because we would like to systematically study the trend of the elastic constants and sound velocities with respect to the ionicity of material.

In this program, to obtain all total energies required for the calculation of the elastic constants we use the Kohn-Sham density functional theory [34, 35] in the local density approximation with the Perdew-Zunger parametrization of exchange and correlation.[36] The total energies are calculated using the fullpotential linearized muffin-tin orbital method as described by Methfessel and van Schilfgaarde.[37] Well converged double basis sets are utilized and the Brillouin zone integrations are done using a $4 \times 4 \times 4$ Monkhorst-Pack sampling set.[38]

The elastic constants and sound velocities in wurtzite GaN and InN as well as other wurtzite semiconductors (SiC, ZnO, and CdSe) as functions of pressure are calculated. We found interesting nonlinear behavior of the elastic constants and sound velocities with pressure that is quite different in the different materials. We also showed that the elastic constants are lower in materials with higher ionicity. Generally, the sound velocities follow the same trend as the elastic constants, i.e., lower in materials with higher ionicity. The pressures at which the C_{44} and C_{66} shear elastic constants cross are investigated. When C_{66} becomes lower, it should be easier to excite the symmetry breaking strain mode related to the wurtzite-to-rocksalt phase transition. We found that the crossover pressure is generally higher than the experimental transition pressure and explained it by the fact that finite temperature fluctuations make it possible to excite the required modes even before the two sound velocities cross. We proposed the average of the crossover and calculated equilibrium transition pressures to be a good estimate for the experimental transition pressure in cases where there is a significant transition enthalpy barrier. Of course, the details near the transition point, the height of the barrier, and the

coupling of the in and out of plane acoustic modes, which are both required to reach the transition point, are important factors for the crystal phase transformation.

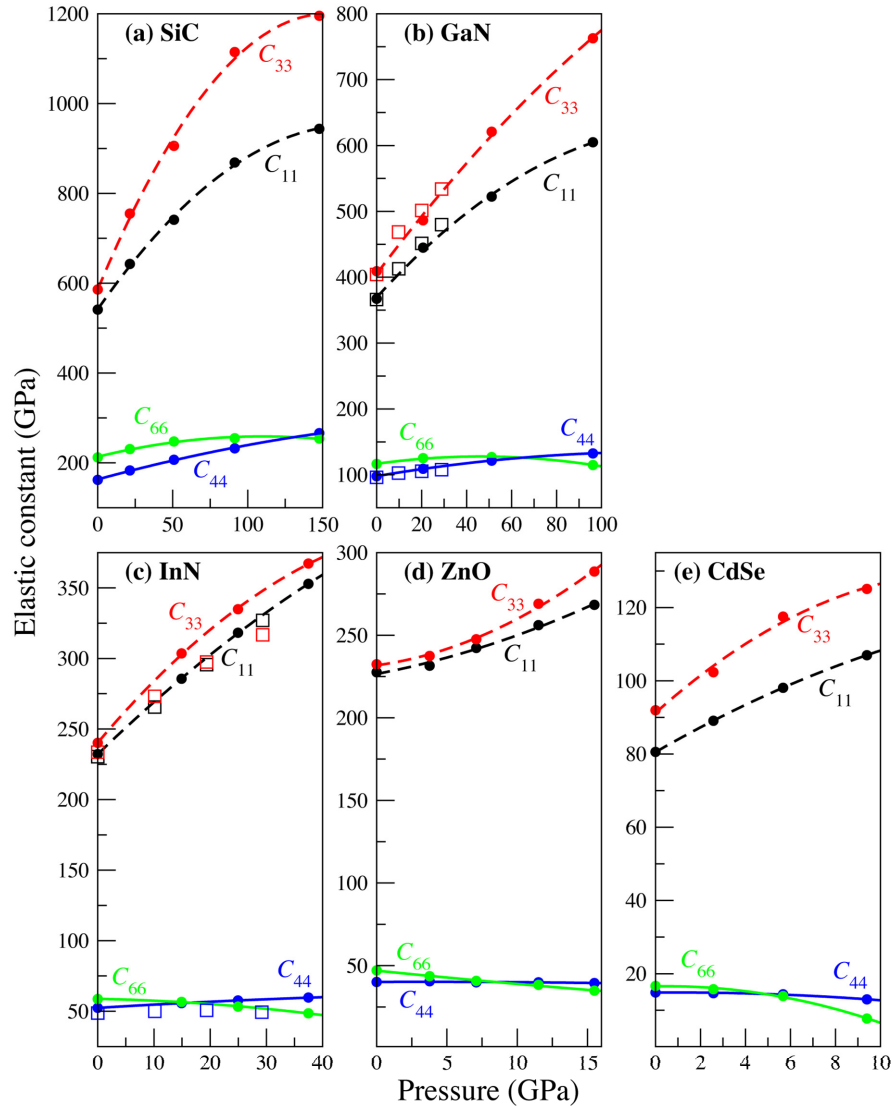Further details of this work can be found in an attached manuscript [P2].

Fig. 9 Calculated pressure dependence of the elastic constants in (a) SiC, (b) GaN, (c) InN, (d) ZnO, and (e) CdSe. In (b) and (c), the square symbols show the calculated results by Łepkowski *et al.*[39]

Properties of phase separated Zn_3P_2 in ZnO

Acceptor doping of ZnO has proved highly challenging. Various dopants have been tried with limited experimental reports of success. While *p*-type conductivity has been reported in ZnO doped with group-V acceptors such as P, As and Sb, computational studies have systematically produced large values for the corresponding acceptor ionization energies, rendering it unlikely that these elements would act as shallow dopants. In this program, propose a mechanism that may give rise to the measurements of hole conductivity in acceptor-doped samples. When P is used as an acceptor dopant, the intent is to introduce large concentrations of the impurity into ZnO. Under such conditions, the solubility limit may be exceeded and a phase separated Zn_3P_2 might be formed.

Based on on density functional theory in the local density approximation, we investigated phase separated Zn_3P_2 in ZnO. (Ultrasoft pseudopotentials with a plane-wave basis set – energy cutoff 300 eV – as implemented in the VASP code [29] were used.) We found that the presence of Zn_3P_2 can lead to measured hole conduction in two ways. First, the Zn_3P_2 itself exhibits a tendency towards *p*-type conductivity. Second, we demonstrated that at the interface between ZnO and the Zn_3P_2 there is a strong tendency for a hole accumulation layer to form.

Further details of this work can be found in an attached manuscript [P1].
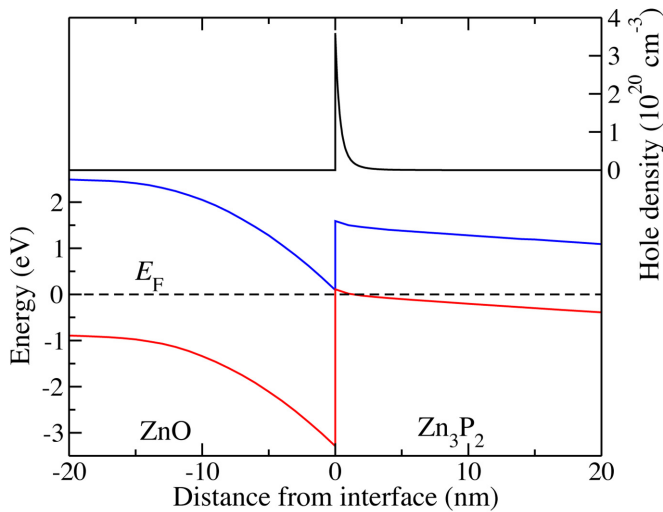

Fig. 10 Calculated hole accumulation layer at the ZnO//Zn3P2 interface due to the unusual low valence band of ZnO

Oxygen defects in CdTe

Recently, local vibrational modes (LVM) related to oxygen impurities in CdTe have been experimentally studied using Fourier transform infrared (FTIR) spectroscopy [40, 41]. Depending on the growth and doping conditions, low temperature FTIR measurements reveal three LVMs related to oxygen: one low frequency mode at 350 cm^{-1} and two high frequency modes at $\nu_1 = 1097$ and $\nu_2 = 1108$ cm^{-1}. As the measuring temperature is increased, the two high frequency modes merge into one at room temperature. Chen *et al.* assigned the low frequency mode to an oxygen substituting on the Te site (O_{Te}), and the two high frequency modes to a complex formed by an oxygen substituting on a Te site and a neighboring Cd vacancy (O_{Te}-V_{Cd}) [40, 41].
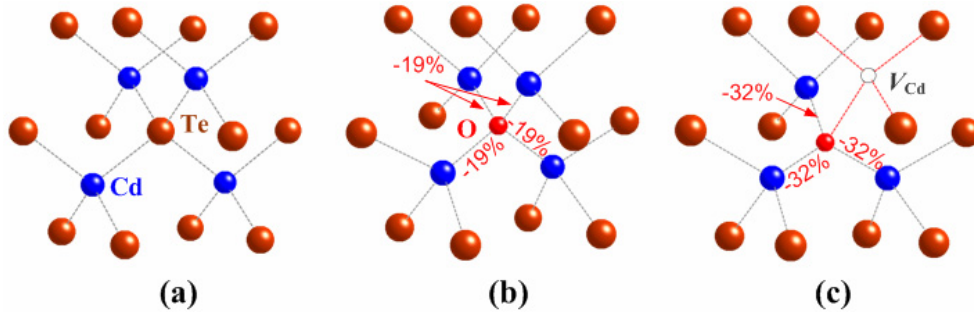

Fig. 11 The local structures of (a) Bulk CdTe, (b) O_{Te}, and (c) O_{Te}-V_{Cd} complex in CdTe.

To understand these vibrational modes, we have investigated O-related centers in CdTe using density functional calculations. Our work is based on density functional theory within the local density approximations (LDA). For the electron-ion iteractions, we used projector augmented wave potentials [23], as implemented in the VASP code [42, 43], with an energy cutoff of 500 eV for the plane-wave basis set. The LVM frequencies of O_{Te} and O_{Te}-V_{Cd} defects were calculated by using force-response matrix (dynamical matrix) calculations. The harmonic approximation is used. We found that the calculated LVM of O_{Te} is consistent with the experimental value. However, the calculated LVM frequencies of O_{Te}-V_{Cd} are much lower than the ν_1 and ν_2 modes observed by Chen *et al*. The calculations clearly showed that the O_{Te}-V_{Cd} complex is not the correct model to explain the observed LVMs. Preliminary results of our work have

been published as a Comment.[44]   In this program, we laid out the computational method and details of the LVMs.   The two high frequencies observed by Chen *et al.* should be attributed to other defects related to the introduction of O in CdTe, not to O_{Te}-V_{Cd}.   We note that the high value of the frequency makes hydrogen (which could be related to the introduction of O during growth) a prime candidate.

Further details of this work can be found in an attached manuscript [P4].
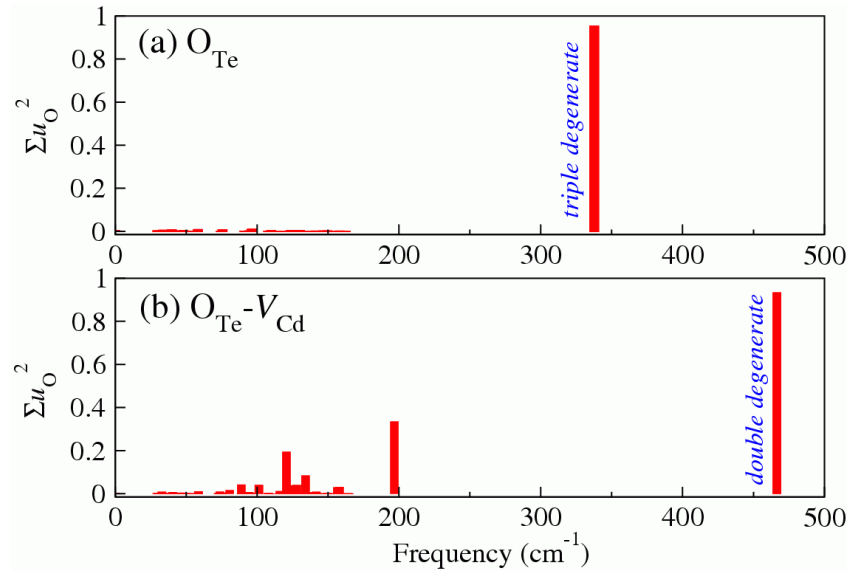
Fig. 12 The sum-square of the three eigenvector components associated with the O atom for all vibrational modes for (a) O_{Te}, and (b) the O_{Te}-V_{Cd} complex (in a 64-atom CdTe supercell).   While the calculated frequency of O_{Te} is in agreement with the observed value, the calculated frequencies of O_{Te}-V_{Cd} are much lower than the observed values of ~1100 cm^{-1}; suggesting that the model proposed by Chen *et al.* is invalid.

Effects of unit cell size for studying alloy properties

Studying alloys by first principles calculations is a very challenging task. This is because, for a given alloy concentration, there are virtually infinite ways to arrange atoms. Since first principles calculations can handle a system of the order of 100 atoms and not much more, alloys are generally studied by the supercell approach. This means the supercell unit is repeated and, strictly speaking, the system is ordered. In order to simulate disordered alloys, many configurations have to be calculated and some averaging schemes have to be employed.
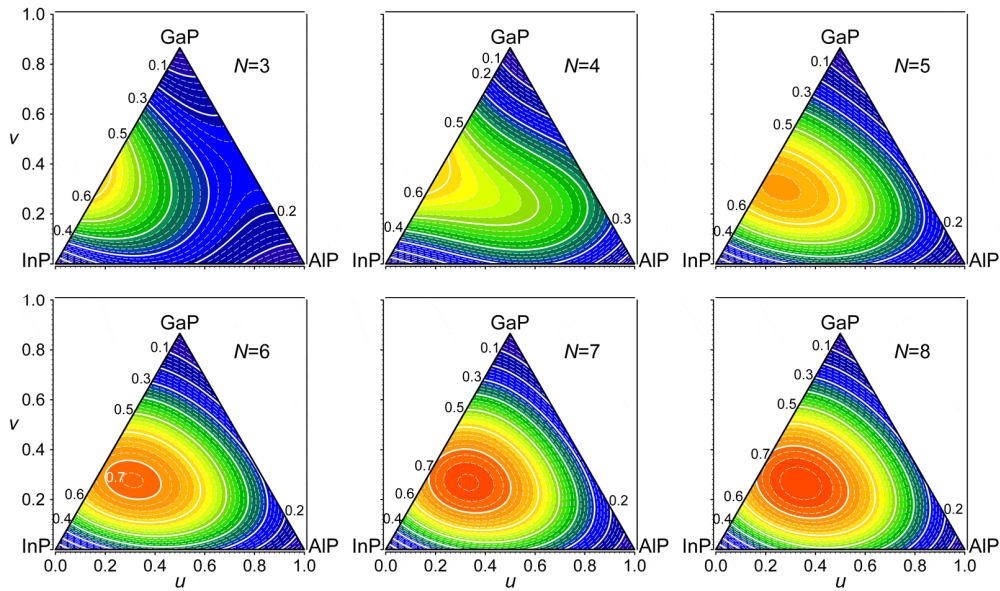

Fig. 13 The contour plots of the calculated bandgap ranges of pseudoternary AlGaInP as a function of alloy compositions ($u = x + y/2$ and $v = \sqrt{3}y/2$). Each figure shows the results of the calculation with a different N_{max}.

One of the most studied properties of alloys is the band gap. For III-V alloys, the cation alloys, for examples $Al_xGa_yIn_{1-x-y}N$, $Al_xGa_yIn_{1-x-y}As$, or $Al_xGa_yIn_{1-x-y}P$ are widely studied both experimentally and theoretically. It is interesting that experimental results from different growth techniques are often in disagreement even when the same or similar alloy compositions are compared. We have suggested that one of the cause of these disagreements might be the fact that samples from different techniques have different alloy orderings [45]. In this program, we focused our attentions in studying a complete set of theoretical possible arrangements within a given cell size. These

complete results allow us to investigate how the band properties relate to the atomic arrangements. Note, however, that many of the configurations studied might have very high energy and difficult to fabricate. While a larger cell size provides more possible configurations – allowing a more complete study – and finer composition steps, the computational demand is increased rapidly. Therefore, it is important to investigate the size of unit cell that sufficiently gives the converged results. In this work, we used the quaternary alloys $Al_xGa_yIn_{1-x-y}P$ as an illustration case. The general results should, however, be applied to other alloy systems. We found that it is sufficient to use the supercell size as small as 5 cation atoms to yield reasonable results; providing that all possible cell shapes are included. The bandgap range of AlGaInP alloy is reported (in the form of a polynomial function). It is found that the bandgap range for AlGaInP alloy system is large (~0.8 eV) for the compositions near the middle of the composition space (slightly shifted toward the low Al composition side).

Further details of this work can be found in an attached manuscript [P5].

References

[1]   G. Kresse and J. Furthmüller, Computational Materials Science **6**, 15 (1996).

[2]   J. P. Perdew, K. Burke, and M. Ernzerhof, Physical Review Letters **77**, 3865 (1996).

[3]   J. Heyd, G. E. Scuseria, and M. Ernzerhof, The Journal of Chemical Physics **118**, 8207 (2003).

[4]   A. V. Krukau, O. A. Vydrov, A. F. Izmaylov, and G. E. Scuseria, The Journal of Chemical Physics **125**, 224106 (2006).

[5]   http://leonardo.phys.washington.edu/feff/.

[6]   H. Morkoc, S. Strite, G. B. Gao, M. E. Lin, B. Sverdlov, and M. Burns, Journal of Applied Physics **76**, 1363 (1994).

[7]   F. A. Ponce and D. P. Bour, Nature **386**, 351 (1997).

[8]   S. Nakamura, M. Senoh, S.-i. Nagahama, N. Iwasa, T. Yamada, T. Matsushita, H. Kiyoku, and Y. Sugimoto, Japanese Journal of Applied Physics **35**, L74 (1995).

[9]   C. G. Van de Walle, S. Limpijumnong, and J. Neugebauer, Physical Review B (Condensed Matter and Materials Physics) **63**, 245205 (2001).

[10]   S.-H. Wei, Computational Materials Science **30**, 337 (2004).

[11]   C. H. Park, S. B. Zhang, and S. H. Wei, Physical Review B **66**, 73202 (2002).

[12]   C. Stampfl and C. G. Van de Walle, Physical Review B **65**, 155212 (2002).

[13]   Y. Zhang, W. Liu, and H. Niu, Physical Review B **77**, 035201 (2008).

[14]   Á. Szabó, N. T. Son, E. Janzén, and A. Gali, Applied Physics Letters **96**, 192110 (2010).

[15]   Y. Taniyasu, M. Kasu, and T. Makimoto, Nature **441**, 325 (2006).

[16]   Q. Yan, P. Rinke, M. Scheffler, and C. G. Van de Walle, Applied Physics Letters **95**, 121111 (2009).

[17]   D. C. Look, D. C. Reynolds, J. W. Hemsky, J. R. Sizelove, R. L. Jones, and R. J. Molnar, Physical Review Letters **79**, 2273 (1997).

[18]   D. C. Look, Materials Science and Engineering B **80**, 383 (2001).

[19]   Z. Q. Fang, J. W. Hemsky, D. C. Look, and M. P. Mack, Applied Physics Letters **72**, 448 (1998).

[20]   K. H. Chow, G. D. Watkins, A. Usui, and M. Mizuta, Phys. Rev. Lett. **85**, 2761 (2000).

[21] L. S. Vlasenko, C. Bozdog, G. D. Watkins, F. Shahedipour, and B. W. Wessels, Phys. Rev. B **65**, 205202 (2002).

[22] D. Look, D. Reynolds, Z. Fang, J. Hemsky, J. Sizelove, and R. Jones, Materials Science and Engineering B **66**, 30 (1999).

[23] G. Kresse and D. Joubert, Physical Review B **59**, 1758 (1999).

[24] J. T-Thienprasert, J. Nukeaw, A. Sungthong, S. Porntheeraphat, S. Singkarat, D. Onkaw, S. Rujirawat, and S. Limpijumnong, Applied Physics Letters **93**, 051903 (2008).

[25] S. Limpijumnong and C. G. Van De Walle, Physica Status Solidi B-Basic Research **228**, 303 (2001).

[26] T. Koida, H. Fujiwara, and M. Kondo, Japanese Journal of Applied Physics **46**, L685 (2007).

[27] C. G. Van de Walle, Phys. Rev. Lett. **85**, 1012 (2000).

[28] D. M. Hofmann, A. Hofstaetter, F. Leiter, H. Zhou, F. Henecker, B. K. Meyer, S. B. Orlinskii, J. Schmidt, and P. G. Baranov, Phys. Rev. Lett. **88**, 045504 (2002).

[29] G. Kresse and J. Furthmüller, Comput. Mater. Sci. **6**, 15 (1996).

[30] P. E. Blöchl, Phys. Rev. B **50**, 17953 (1994).

[31] A. Janotti and C. G. Van de Walle, Nature Mater. **6**, 44 (2007).

[32] A. Janotti and C. G. Van de Walle, Appl. Phys. Lett. **92**, 032104 (2008).

[33] A. K. Singh, A. Janotti, M. Scheffler, and C. G. Van de Walle, Phys. Rev. Lett. **101**, 055502 (2008).

[34] P. Hohenberg and W. Kohn, Physical Review **136**, B864 (1964).

[35] W. Kohn and L. J. Sham, Physical Review **140**, A1133 (1965).

[36] J. P. Perdew and A. Zunger, Phys. Rev. B **23**, 5048 (1981).

[37] M. Methfessel, M. v. Schilfgaarde, and R. A. Casali, *Electronic Structure and Physical Properties of Solids. The Uses of the LMTO Method* (Springer Verlag, Berlin, 2000), Vol. 535.

[38] H. J. Monkhorst and J. D. Pack, Phys. Rev. B **13**, 5188 (1976).

[39] S. P. Łepkowski, J. A. Majewski, and G. Jurczak, Phys. Rev. B **72**, 245201 (2005).

[40] G. Chen, I. Miotkowski, S. Rodriguez, and A. K. Ramdas, Phys. Rev. Lett. **96**, 035508 (2006).

[41] G. Chen, I. Miotkowski, S. Rodriguez, and A. K. Ramdas, Phys. Rev. B **75**, 125204 (2007).

[42] G. Kresse and J. Furthmüller, Comput. Mat. Sci. **6**, 15 (1996).

[43] G. Kresse and J. Hafner, J. Phys.:Cond. Matt. **6**, 8245 (1994).

[44] L. Zhang, J. T-Thienprasert, M. H. Du, D. J. Singh, and S. Limpijumnong, Phys. Rev. Lett. **102**, 209601 (2009).

[45] S. Jungthawan, S. Limpijumnong, R. Collins, K. Kim, P. A. Graf, and J. A. Turner, Journal of Applied Physics **105**, 123531 (2009).

Related Activities:

Publications (attached)

[P1] "*Alternative sources of p-type conduction in acceptor-doped ZnO*"
S. Limpijumnong, L. Gordon, M. Miao, A. Janotti, and C.G. Van de Walle
Appl. Phys. Lett. **97**, 072112 (2010).

[P2] "*Pressure-dependent elastic constants and sound velocities of wurtzite SiC, GaN, InN, ZnO and CdSe and their relation to phase transition: First-principles study*"
K. Sarasamak, S. Limpijumnong, and W.R. L. Lambrecht
Phys. Rev. B **82**, 035201 (2010).

[P3] "*X-ray absorption spectroscopy of indium nitride, indium oxide, and their alloys*"
J. T-Thienprasert, S. Rujirawat, J. Nukeaw and S. Limpijumnong
Comput. Mater. Sci. **49**, S37 (2010).

[P4] "*Vibrational signatures of O_{Te} and O_{Te}-V_{Cd} in CdTe: A first-principles study*"
J. T-Thienprasert, S. Limpijumnong, A. Janotti, C.G. Van de Walle, L. Zhang, M.-H. Du and D.J. Singh
Comput. Mater. Sci. **49**, S242 (2010).

[P5] "*The effects of unit cell size on the bandgap range in the direct enumeration study of $Al_xGa_yIn_{1-x-y}P$ alloys*"
S. Jungthawan, K. Kim and S. Limpijumnong
Comput. Mater. Sci. **49**, S114 (2010).

[P6] "*Hydrogen doping in indium oxide: An ab initio study*"
S. Limpijumnong, P. Reunchan, A. Janotti, and C.G. Van de Walle
Phys. Rev. B **80**, 193202 (2009).

Presentations

[C1] <u>Sukit Limpijumnong</u> delivered an invited talk at the international Conference on Materials for Advanced Technologies (ICMAT 2009) [Symp. Q], Suntec Singapore International Convention & Exhibition Centre, Singapore, June 23 - July 3, 2009, entitled: *"Stability of crystal phases under different loading conditions"*.

[C2] <u>Sukit Limpijumnong</u> delivered an invited talk at the 5th Conference of the Asian Consortium on Computational Materials Science (ACCMS-5), Hanoi Melia Hotel, Hanoi, Vietnam, Sept 7-11, 2009, entitled: *"Local Structure Analysis by X-ray Absorption Spectroscopy and First Principles Calculations"*.

[C3] <u>Sukit Limpijumnong</u> delivered an invited talk at the Material Research Society Fall meeting (2009 MRS Fall), Symposium H: ZnO and related materials, Boston, MA, USA, Nov 30- Dec 4, 2009, entitled: *"Revealing Local Structures around dopants in ZnO by X-ray Absorption Spectroscopy"*.

[C4] <u>Sukit Limpijumnong</u> delivered an invited talk at the 4th General Meeting of Conference of the Asian Consortium on Computational Materials Science - Virtual Organization (ACCMS-VO) at Institute of Materials Research, Tohoku University, Sendai and Hotel Taikanso Matsushima, Japan, January 12-14, 2010, entitled: *"Local vibration modes as fingerprints of crystal defects"*.

[C5] *"Direct Enumeration Studies of Band-Gap Properties of $Al_xGa_yIn_{1-x-y}P$ Alloys"* at the International Conference on Materials for Advanced Technologies (ICMAT 2009) [Symp. Q], June 23 - July 3, 2009, Suntec Singapore International Convention & Exhibition Centre, Singapore

[C6] *"First Principles Study of Gallium-Frenkel Pairs in Gallium Nitride"* at the International Conference on Materials for Advanced Technologies (ICMAT 2009) [Symp. Q], June 23 - July 3, 2009, Suntec Singapore International Convention & Exhibition Centre, Singapore

[C7] *"First Principles Study of Elastic Constants and Sound Velocities in Wurtzite Phase of SiC, GaN, InN, ZnO and CdSe and Their Relation to the High Pressure Phase Transition"* at the International Conference on Materials for Advanced Technologies (ICMAT 2009) [Symp. Q], June 23 - July 3, 2009, Suntec Singapore International Convention & Exhibition Centre, Singapore

[C8] *"X-Ray Absorption Spectroscopy of Indium Nitride, Indium Oxide, and Their Alloys"* at the International Conference on Materials for Advanced Technologies (ICMAT 2009) [Symp. Q], June 23 - July 3, 2009, Suntec Singapore International Convention & Exhibition Centre, Singapore

[C9] *"Carbon and Silicon impurities in $GaAs_{1-x}N_x$"* at the 5th Conference of the Asian Consortium on Computational Materials Science (ACCMS-5); Sept 7-11, 2009, Hanoi Melia Hotel, Hanoi, Vietnam

[C10] *"Vibration Signatures of O_{Te} and O_{Te}-V_{Cd} in CdTe: A First Principles Study"* at the 5th Conference of the Asian Consortium on Computational Materials Science (ACCMS-5); Sept 7-11, 2009, Hanoi Melia Hotel, Hanoi, Vietnam

Collaborations

1. Dr. D.C. Look (experiment), *Wright-Patterson Air Force Base, OH, USA*

2. Dr. S.B. Zhang (theory), *Rensselaer Polytechnic Institute, NY, USA*

3. Drs. S-H. Wei and K. Kim (theory), *National Renewable Energy Lab., CO, USA.*

4. Prof. Dr. Weimin Chen (experiment), *Linköpin University, Sweden.*

5. Prof. Dr. W.R.L. Lambrecht (theory), *Case Western Reserve Univ., OH, USA.*

6. Prof. Dr. C.G. Van de Walle (theory), *UC Santa Barbara, CA, USA.*

7. Prof. Dr. Jaejun Yu (theory), *Seoul National Univ.*, S. Korea

8. Assoc. Prof. Dr. J. Nukeaw (experiment), *KMITL, Thailand*

9. Assoc. Prof. Dr. Attera Worayingyong, *Kasetsart University*, Thailand

Honors/Awards

- Prof. Sukit Limpijumnong has been named *" 2008 TRF Advanced Research Scholar "* by the Thailand Research Fund (TRF)

- Prof. Sukit Limpijumnong has been appointed as *" APCTP General Council Member 2008-2010"* by the Asia Pacific Center for Theoretical Physics (APCTP), South Korea

- Prof. Sukit Limpijumnong has been appointed as *"TWAS Young Affiliate 2007-2012"* by the Third World Academy of Science (TWAS), Italy

Appendix

Publications

1) "*Alternative sources of p-type conduction in acceptor-doped ZnO*"
   S. Limpijumnong, L. Gordon, M. Miao, A. Janotti, and C.G. Van de Walle
   Appl. Phys. Lett. **97**, 072112 (2010).

2) "*Pressure-dependent elastic constants and sound velocities of wurtzite
   SiC, GaN, InN, ZnO and CdSe and their relation to phase transition:
   First-principles study*"
   K. Sarasamak, S. Limpijumnong, and W.R. L. Lambrecht
   Phys. Rev. B **82**, 035201 (2010).

3) "*X-ray absorption spectroscopy of indium nitride, indium oxide, and their alloys*"
   J. T-Thienprasert, S. Rujirawat, J. Nukeaw and S. Limpijumnong
   Comput. Mater. Sci. **49**, S37 (2010).

4) "*Vibrational signatures of O_{Te} and O_{Te}-V_{Cd} in CdTe: A first-principles study*"
   J. T-Thienprasert, S. Limpijumnong, A. Janotti, C.G. Van de Walle, L.
   Zhang, M.-H. Du and D.J. Singh
   Comput. Mater. Sci. **49**, S242 (2010).

5) "*The effects of unit cell size on the bandgap range in the direct
   enumeration study of $Al_xGa_yIn_{1-x-y}P$ alloys*"
   S. Jungthawan, K. Kim and S. Limpijumnong
   Comput. Mater. Sci. **49**, S114 (2010).

6) "*Hydrogen doping in indium oxide: An ab initio study*"
   S. Limpijumnong, P. Reunchan, A. Janotti, and C.G. Van de Walle
   Phys. Rev. B **80**, 193202 (2009).

Alternative sources of *p*-type conduction in acceptor-doped ZnO

Sukit Limpijumnong,[1,2] Luke Gordon,[1,3] Maosheng Miao,[1] Anderson Janotti,[1] and Chris G. Van de Walle[1,a)]

[1]*Materials Department, University of California, Santa Barbara, California 93106-5050, USA*
[2]*School of Physics, Synchrotron Light Research Institute, Suranaree University of Technology, Nakhon Ratchasima 30000, Thailand*
[3]*Theoretical Physics, University of Dublin, Trinity College, Ireland*

We report first-principles calculations and interface simulations for Zn_3P_2, a compound that may form during doping of ZnO with phosphorous. While P is a deep acceptor in ZnO and thus unable to produce *p*-type conductivity, we show that hole accumulation can occur at ZnO/Zn_3P_2 interfaces due to the unusual valence-band alignment between the two materials. This provides an explanation for the hole conductivity that has been observed in Hall measurements on phosphorous-doped ZnO. © 2010 American Institute of Physics. [doi:10.1063/1.3481069]

ZnO is a highly promising material for a wide variety of applications, including window layers for solar cells, transparent transistors, and sensors. Based on its band gap (3.4 eV) and large exciton binding energy (60 meV) it would also be an excellent material for light emitters. Acceptor doping of ZnO has proved highly challenging. There are by now a large number of reports in the literature (too numerous to cite) claiming observations of *p*-type conductivity in ZnO doped with different elements. The lack of follow-up reports and the scarcity of device demonstrations based on *p-n* junctions indicate that there are serious problems with reliability and reproducibility. In addition, fundamental questions have arisen about the ability of some of the acceptor dopants to actually yield hole conduction. In particular, while *p*-type conductivity has been reported in ZnO doped with group-V acceptors such as P,[1–4] As,[5] and Sb,[6] computational studies[7] have systematically produced large values for the corresponding acceptor ionization energies, rendering it unlikely that these elements would act as shallow dopants. In the case of nitrogen, estimates of ionization energies have been inconclusive, although recent computations indicate a very deep level.[8] Nitrogen is the element for which the most favorable results have been obtained;[9–11] still, the questions about reproducibility and reliability also apply in this case.

If these elements, when incorporated into ZnO, do not actually act as shallow acceptors, then why do Hall measurements yield a signal that seems indicative of hole conductivity? One possible cause, recently discussed by Ohgaki *et al.*[12] and by Bierwagen *et al.*[13] is the presence of inhomogeneities in the sample. It was demonstrated, based both on modeling and on explicit measurements for a known *n*-type sample, that lateral inhomogeneities in carrier concentrations can result in an incorrect assignment of the carrier type. Other mechanisms for explaining the hole conductivity have been proposed[14,15] but have no direct experimental confirmation.

In this letter, we propose and document another mechanism that may give rise to spurious measurements of hole conductivity in acceptor-doped samples. The mechanism will be illustrated with the example of P but it may also occur in the case of the other group-V impurities (N, As, and Sb). When P is used as an acceptor dopant, the intent is to introduce large concentrations of the impurity into ZnO. Under those conditions, the solubility limit may be exceeded, an issue that has been extensively discussed in the context of doping of other semiconductors (see Refs. 16 and 17 for a discussion of acceptors in ZnSe and ZnTe and Refs. 18 and 19 for GaN). Solubility limits arise because it becomes more favorable for the impurity to incorporate into an alternate phase rather than on a substitutional lattice site inside the semiconductor. The competing phase would typically manifest itself as precipitates inside the host material. Candidates for alternate phases can be identified by examining which compounds can be formed between the impurity and the host element. In the case of group-V impurities in ZnO, the prime candidates are the Zn_3X_2 compounds (where X=N, P, As, or Sb). We therefore perform an investigation of such compounds and their impact when they are incorporated as precipitates in ZnO. We will see that the presence of such compounds can lead to measured hole conduction in two ways. First, the compounds themselves exhibit a tendency toward *p*-type conductivity. Second, we will demonstrate that at the interface between ZnO and the Zn_3X_2 compound there is a strong tendency for a hole accumulation layer to form.

Our investigations of ZnO and Zn_3P_2 are based on first-principles calculations using density functional theory in the local density approximation. Ultrasoft pseudopotentials with a plane-wave basis set (energy cutoff 300 eV) as implemented in the VASP code[20] were used. Bulk calculations were performed for Zn_3P_2 in the $P42/nmc$ structure with a 40-atom unit cell. We obtained a calculated lattice constant of 7.897 Å, which compares favorably with the experimental value[21] of 8.097 Å. A $2 \times 2 \times 2$ Monkhorst–Pack *k*-point sampling was used in the Brillouin-zone integration.

Insight into band alignments as well as doping tendencies of the material can be provided by investigating the behavior of interstitial hydrogen.[22] We performed supercell calculations for a single hydrogen interstitial in Zn_3P_2 using 40-atom supercells and $2 \times 2 \times 2$ *k*-point sampling. The formation energy of H_i^q (q=−, 0, or +) is calculated according to the definition given in Ref. 23.

Consistent with general tendencies,[22] H in the positive charge state prefers a lattice location in a P-antibonding site,

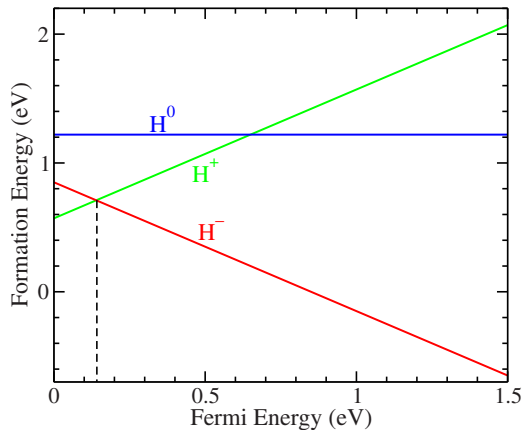a)Electronic mail: vandewalle@mrl.ucsb.edu.

FIG. 1. (Color online) Calculated formation energies of hydrogen interstitials in Zn_3P_2 as a function of Fermi level (referenced to the VBM). H_2 molecules are assumed as the reservoir.

FIG. 2. (Color online) (Bottom) Band diagram for a ZnO/Zn_3P_2 interface. (Top) Corresponding density of holes.

while in the negative charge state it prefers a Zn-antibonding site. The neutral charge state is never stable, as can be seen in Fig. 1. The $+/-$ transition level is found at 0.12 eV above the valence-band maximum (VBM).

Assuming the universal alignment discussed in Ref. 22 is valid, the position of the VBM with respect to the vacuum level is expected to be at approximately $-4.50-0.12 = -4.62$ eV. This is quite high, on an absolute energy scale, and will have consequences for the electronic behavior of interfaces between Zn_3P_2 and ZnO, as discussed below. Materials in which the VBM occurs at a high energy with respect to vacuum generally exhibit a tendency toward *p*-type conductivity, i.e., impurities that act as shallow acceptors will be more easily incorporated, and compensation effects due to donors suppressed. This tendency toward *p*-type conductivity may, in itself, explain why P-doped ZnO in which Zn_3P_2 precipitates occur could exhibit measurable hole conduction. However, as we will discuss below, it is not actually necessary for the Zn_3P_2 itself to be *p* type.

Another means of producing insight into the band alignment is by performing calculations for a Zn_3P_2 surface, which produce the position of the VBM with respect to the vacuum level. In principle, such alignments are sensitive to the details of the surface but for the qualitative purposes of the present work this is not a limitation. We performed surface calculations in a repeated-slab geometry with a slab thickness of nine layers (approximately 16 Å) along the nonpolar [010] surface and a vacuum spacing of 12 Å in between. On the unrelaxed surface, the VBM is found at -4.38 eV with respect to the vacuum level. This value changes to -4.48 eV when relaxations are included, indicating the value is not very sensitive to such effects. Gratifyingly, the latter value is in good agreement with the value for the Zn_3P_3 VBM position, at -4.62 eV, obtained from the hydrogen-level alignment.

We now turn to simulations of the ZnO/Zn_3P_2 interface. The purpose of this simulation is not to provide an atomistic depiction of the interface; indeed, because of the sizeable lattice mismatch, creating a coherent interface between ZnO and Zn_3P_2 would be challenging. As we will see, however, our conclusions do not depend on details of interfacial structure but only on qualitative values of band alignment. Therefore use of "natural band alignments," in this case based on the estimates obtained above for hydrogen-level alignments
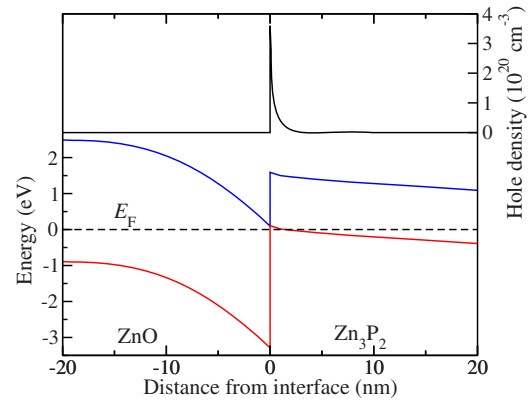
and surface calculations, will suffice. We focus on a simulation of band positions in the vicinity of the interface.

Our estimates above placed the VBM of Zn_3P_2 at around 4.5–4.6 eV below the vacuum level. Combined with information about the VBM of ZnO,[22] we estimate a valence-band offset between the two materials of about 3.4 eV. Interface-specific effects may affect this value at an actual heterojunction; however, we will demonstrate that our conclusions are not sensitive to the precise value of this offset (with a very wide tolerance). We note that, with a ZnO band gap of 3.40 eV, this estimated VB offset causes the VBM of Zn_3P_2 to lie at approximately the same level as the conduction-band minimum (CBM) of ZnO. This, in its own right, indicates that at an interface there may be a strong tendency for electrons from the Zn_3P_2 VBM to transfer to the ZnO CBM, thus leading to the formation of holes in Zn_3P_2.

We have backed up these qualitative insights with explicit Schrödinger–Poisson simulations[24] of a ZnO/Zn_3P_2 interface. For the purpose of the simulations some assumptions need to be made about doping of the two materials. (We will show below that our results are not sensitive to the details of these assumptions.) On the ZnO side, we assume that P is incorporated as a deep acceptor in ZnO with an ionization energy of 0.93 eV (Ref. 7). The simulation in Fig. 2 was performed assuming a deep acceptor concentration of 10^{19} cm^{-3}. With regards to doping of Zn_3P_2, as noted above we expect this material to have a tendency to be *p* type; however, for the purposes of the simulation we assumed a "worst-case" scenario, in which Zn_3P_2 is *n* type (with a donor concentration of 10^{17} cm^{-3}), thus making it very clear that the appearance of holes at the interface does not rely on the *p*-type nature of Zn_3P_2. A band gap of 1.5 eV was assumed for Zn_3P_2 (Ref. 25).

Figure 2(a) clearly shows that a hole accumulation layer is formed at the interface. Because the Zn_3P_2 VBM lies at a high energy, electrons in the Zn_3P_2 VB have a tendency to transfer to the ZnO, where they can find lower-energy states. If the ZnO were undoped or *n* type, these electrons would go into the ZnO conduction band (CB); the interface would then exhibit mixed conduction. But if the ZnO is doped with deep acceptors, the electrons can compensate those acceptors and free electrons are removed from the system. Figure 2(b) shows that a hole accumulation layer forms within a distance of a few nanometer from the interface, and with a density exceeding 10^{20} cm^{-3}. The corresponding charge density of the sheet is on the order of 10^{13} cm^{-2} (Fig. 3). We suggest
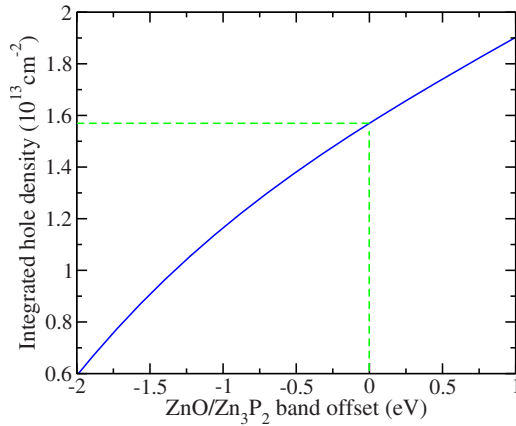
FIG. 3. (Color online) Dependence of integrated hole density in the hole accumulation layer at a ZnO/Zn_3P_2 interface on the value of the band offset between ZnO and Zn_3P_2. Zero offset (dashed line) refers to the situation where the ZnO CBM is lined up with the Zn_3P_2 VBM; positive values indicate that the VBM in Zn_3P_2 is raised with respect to ZnO.

that the presence of this sheet of charge, at interfaces embedded in the ZnO layer, may be responsible for measurements of hole conductivity in P-doped ZnO.

We have performed extensive checks to ensure that our qualitative conclusions are not sensitive to the details of our simulations. Decreasing the concentration of deep acceptors in ZnO leads to a decrease in the density of the hole accumulation layer, but as noted above, a *p*-type layer continues to form even if the ZnO is undoped or *n*-type. We have also checked the sensitivity to the band alignment. Figure 3, generated using parameters identical to those in Fig. 2 but with a variable band alignment, clearly shows that a hole accumulation layer continues to form, even if the Zn_3P_2 VBM is well below the ZnO CBM.

While our calculations are based on P-doped ZnO, we believe that the conclusions also apply to ZnO doped with other deep acceptors such as As or Sb. Indeed, explicit calculations for Zn_3As_2 showed that the VBM at its (relaxed) surface is located at -4.53 eV, a result very similar to that obtained for Zn_3P_2. Following the general trends between phosphides, arsenides, and antimonides,[22] we expect the VBM of Zn_3Sb_2 to lie at least as high as that of Zn_3P_2 and Zn_3As_2. The VBM of nitride compounds is expected to lie lower than that of P compounds. However, the fact that a hole accumulation layer can form even if the VBM of Zn_3P_2 is 2 eV below the CBM of ZnO, as shown in Fig. 3, is a strong indicator that the mechanism described here may also apply in the case of Zn_3N_2. This could be a potential explanation for the localized *p*-type conductivity phenomena observed in Ref. 26.

In summary, we have presented first-principles calculations for Zn_3P_2 and simulations of ZnO/Zn_3P_2 interfaces that provide a plausible explanation for the observed *p*-type conductivity in ZnO doped with group-V acceptors.

[1]T. Aoki, Y. Hatanaka, and D. C. Look, Appl. Phys. Lett. **76**, 3257 (2000).
[2]K.-H. Bang, D.-K. Hwang, M.-C. Park, Y.-D. Ko, I. Yun, and J.-M. Myoung, Appl. Surf. Sci. **210**, 177 (2003).
[3]K.-K. Kim, H.-S. Kim, D.-K. Hwang, J.-H. Lim, and S.-J. Park, Appl. Phys. Lett. **83**, 63 (2003).
[4]G. Hu, H. Gong, E. F. Chor, and P. Wu, Appl. Phys. Lett. **89**, 021112 (2006).
[5]Y. R. Ryu, S. Zhu, D. C. Look, J. M. Wrobel, H. M. Jeong, and H. W. White, J. Cryst. Growth **216**, 330 (2000).
[6]F. X. Xiu, Z. Yang, L. J. Mandalapu, D. T. Zhao, J. L. Liu, and W. P. Beyermann, Appl. Phys. Lett. **87**, 152101 (2005).
[7]C. H. Park, S. B. Zhang, and S.-H. Wei, Phys. Rev. B **66**, 073202 (2002).
[8]J. L. Lyons, A. Janotti, and C. G. Van de Walle, Appl. Phys. Lett. **95**, 252105 (2009).
[9]D. C. Look, D. C. Reynolds, C. W. Litton, R. L. Jones, D. B. Eason, and G. Cantwell, Appl. Phys. Lett. **81**, 1830 (2002).
[10]A. Tsukazaki, A. Ohtomo, T. Onuma, M. Ohtani, T. Makino, M. Suminya, K. Ohtani, S. F. Chichibu, S. Fuke, Y. Segawa, H. Ohno, H. Koinuma, and M. Kawasaki, Nature Mater. **4**, 42 (2005).
[11]B. T. Adekore, J. M. Pierce, R. F. Davis, D. W. Barlage, and J. F. Muth, J. Appl. Phys. **102**, 024908 (2007).
[12]T. Ohgaki, N. Ohashi, S. Sugimura, H. Ryoken, I. Sakaguchi, Y. Adachi, and H. Haneda, J. Mater. Res. **23**, 2293 (2008).
[13]O. Bierwagen, T. Ive, C. G. Van de Walle, and J. S. Speck, Appl. Phys. Lett. **93**, 242108 (2008).
[14]S. Limpijumnong, S. B. Zhang, S. H. Wei, and C. H. Park, Phys. Rev. Lett. **92**, 155504 (2004).
[15]W. J. Lee, J. Kang, and K. J. Chang, Phys. Rev. B **73**, 024117 (2006).
[16]C. G. Van de Walle, D. B. Laks, G. F. Neumark, and S. T. Pantelides, Phys. Rev. B **47**, 9425 (1993).
[17]D. B. Laks, C. G. Van de Walle, G. F. Neumark, and S. T. Pantelides, Appl. Phys. Lett. **63**, 1375 (1993).
[18]J. Neugebauer and C. G. Van de Walle, J. Appl. Phys. **85**, 3003 (1999).
[19]C. G. Van de Walle, S. Limpijumnong, and J. Neugebauer, Phys. Rev. B **63**, 245205 (2001).
[20]G. Kresse, Comput. Mater. Sci. **6**, 15 (1996).
[21]M. von Stackelberg and R. Paulus, Z. Phys. Chem. Abt. B **28B**, 427 (1935).
[22]C. G. Van de Walle and J. Neugebauer, Nature (London) **423**, 626 (2003).
[23]S. Limpijumnong, P. Reunchan, A. Janotti, and C. G. Van de Walle, Phys. Rev. B **80**, 193202 (2009).
[24]Nanodevice simulation software, www.nextnano.de/nextnano3.
[25]J. M. Pawlikowski, Phys. Rev. B **26**, 4711 (1982).
[26]A. Krtschil, D. C. Look, Z.-Q. Fang, A. Dadgar, A. Diez, and A. Krost, Physica B **376–377**, 703 (2006).

Pressure-dependent elastic constants and sound velocities of wurtzite SiC, GaN, InN, ZnO, and CdSe, and their relation to the high-pressure phase transition: A first-principles study

Kanoknan Sarasamak

College of KMITL Nanotechnology, King Mongkut's Institute of Technology Ladkrabang, Bangkok 10520, Thailand

Sukit Limpijumnong

School of Physics, Suranaree University of Technology and Synchrotron Light Research Institute, Nakhon Ratchasima 30000, Thailand
and Thailand Center of Excellence in Physics (ThEP Center), Commission on Higher Education, Bangkok 10400, Thailand

Walter R. L. Lambrecht

Department of Physics, Case Western Reserve University, Cleveland, Ohio 44106-7079, USA

Elastic constants and sound velocities calculated from first principles as function of pressure are presented for wurtzite SiC, GaN, InN, ZnO, and CdSe. The C_{11} and C_{33} elastic constants, which are involved in longitudinal sound waves along symmetry directions, are found to monotonically increase with pressure. The shear moduli C_{44} and C_{66}, which are involved in transverse sound waves along symmetry directions, either decrease with increasing pressure or initially increase from zero pressure but then turn over and start decreasing. Of special interest is the pressure at which the C_{44} and C_{66} elastic constants cross. At this pressure, the transverse acoustic waves in the basal plane, which are shown to be closely related to the symmetry breaking strain component that leads to the phase transition, become easier to excite than the ones with displacement along the c axis. It is found that this crossover pressure is an upper limit to the actual phase transition pressure. The average of the calculated equilibrium transition pressure and the crossover pressure is proposed as a good estimate for the actual transition pressure in cases where the transition is strongly kinetically hindered by an enthalpy barrier between the two phases. This occurs for SiC and GaN and is confirmed with literature data for AlN. For the remaining materials, all these pressures are close to each other. The trends of the elastic constants and sound velocities with the materials' Phillips scale ionicity are also reported.

I. INTRODUCTION

Most group-IV, III-V, and II-VI-semiconductors are well known to undergo a high-pressure phase transition from a tetrahedrally bonded phase to an octahedrally bonded phase. Most prior work has focused on determining the equilibrium transition pressure, at which the two phases have the same enthalpy. Recently, however, several studies have started to study the mechanism of transformation from one phase to the other. In particular, homogeneous transition paths have been proposed between wurtzite and rocksalt[1–3] and zincblende and rocksalt.[4–7] In such mechanisms, the transformation happens by a continuous deformation from one structure to the other by imposed strains. At each strain, the internal coordinates (i.e., atomic positions) are required to adjust to minimize the energy. For example, for the wurtzite to rocksalt transformation, the two strains correspond to a c/a reduction perpendicular to the basal plane and a strain in the basal plane along the $[10\bar{1}0]$ direction or any direction which is $\pm 60°$ or $\pm 120°$ from it, which we can call the b/a direction. On the experimental side, advanced diffraction techniques utilizing high brilliance synchrotron x-rays open up the opportunity to study crystal structures under high pressure in more detail.[8–11] Although the actual transition mechanism is likely to be more complex than a homogeneous transformation, as shown for example by molecular dynamics studies,[12] the homogeneous transformation path provides a useful simplified picture which may in reality happen locally in small

regions and determine the nucleation event of the transition. Sarasamak *et al.*[3] studied the enthalpy landscapes in this space of strains driving the homogeneous transformation. Such enthalpy landscapes can be constructed at different hydrostatic pressures. By constructing such enthalpy landscapes, one can gain insight in the behavior of the system along various paths from one phase to the other within the strain coordinates. The local curvatures in different directions for example will tell us in which direction the system will initially most easily deform. The elastic constants are closely related to the local shape of this enthalpy landscape. In fact, they essentially determine the curvatures near the minima on this energy landscape. It is thus of interest to determine the elastic constants as function of pressure to better understand the initial stages of phase transition.

The elastic constants are also closely related to the sound velocities. Thus studying the sound velocities as function of pressure provides possibly an experimental way to determine the pressure dependence of the elastic constants. In fact, homogeneous strains are simply the long-wavelength limit of the acoustic phonon modes. The relation between sound waves in specific directions and the strains involved in the zincblende and wurtzite to rocksalt transition were previously pointed out by Prikhodko *et al.*[13]

Here, we study the elastic constants and sound velocities as function of direction and pressure in various wurzite crystals: SiC, GaN, InN, ZnO, and CdSe. Our choice of materials includes a IV-IV, two III-V, and two II-VI compounds. These

materials also have varied transition pressures. As will be seen, rather different behavior is obtained for different materials. Because we have systematically studied several materials, we can investigate the trend of the elastic constants and sound velocities with respect to the ionicity of material.

The paper is organized as follows. In Sec. II, we give the expressions for the sound velocities in different direction as function of the elastic constants. The calculation of elastic constants as function of pressure is also discussed. Essentially, they are obtained by calculating the total energy as function of a set of strains. Details of the computational method used to calculate the total energies from first principles are given in Sec. III. The results for the elastic constants and sound velocities in specific high-symmetry directions as function of pressure are presented in Sec. IV. In this section, the trend of the elastic constants and sound velocities with respect to the ionicity of material with also be presented. A summary of the main results is given in Sec. V.

II. THEORY

A. Sound velocities

The acoustic vibrational modes of a solid in the long-wavelength limit are obtained from the Christoffel equation,[14]

$$\rho\omega^2 u_i = M_{il}u_l, \tag{1}$$

where ρ is the mass density, ω the vibrational angular frequency, u_i the displacement amplitudes and summation convention is used for repeated Cartesian indices. The matrix M_{il} is given by

$$M_{il} = c_{ijkl}k_jk_k, \tag{2}$$

where c_{ijkl} is the elastic constant tensor elements, and k_j the wave vector components of the vibrational wave. Using Voigt notation, in the case of an hexagonal crystal (will be explained later), the M_{il} matrix reduces to

$$\begin{bmatrix} C_{11}k_x^2 + C_{66}k_y^2 + C_{44}k_z^2 & (C_{12} + C_{66})k_xk_y & (C_{13} + C_{44})k_xk_z \\ (C_{12} + C_{66})k_xk_y & C_{66}k_x^2 + C_{11}k_y^2 + C_{44}k_z^2 & (C_{13} + C_{44})k_yk_z \\ (C_{13} + C_{44})k_xk_z & (C_{13} + C_{44})k_yk_z & C_{44}(k_x^2 + k_y^2) + C_{33}k_z^2 \end{bmatrix}. \tag{3}$$

For any direction the eigenvectors will be a quadratic function of $k = |\mathbf{k}|$ and hence $\omega = c_n(\hat{k})k$ with $c_n(\hat{k})$ the sound velocity for polarization n and direction $\hat{k}$. The results for hexagonal crystals were reported before by Rosen and Klimker.[15] For example, for $\mathbf{k}$ along [001], $k_x = k_y = 0$ and $k_z = k$, the sound velocities become

$$c_{TA}([001]) = \sqrt{C_{44}/\rho}, \quad \text{with twofold degeneracy}$$

$$c_{LA}([001]) = \sqrt{C_{33}/\rho}, \tag{4}$$

where TA and LA stand for transverse and longitudinal acoustic.

Similarly, for any acoustic wave with wave vector in the basal plane, the sound velocities are given by the results for the [100] wave vector direction,

$$c_{LA}([100]) = \sqrt{C_{11}/\rho},$$

$$c_{TA[010]}([100]) = \sqrt{C_{66}/\rho},$$

$$c_{TA[001]}([100]) = \sqrt{C_{44}/\rho}, \tag{5}$$

where the first TA mode has displacements in-plane and the second one has displacements perpendicular to the basal plane. The results are independent of direction in the plane because we diagonalized a quadratic form representing an ellipsoid. Since this ellipsoid must have sixfold symmetry about the z axis, it must be an ellipsoid of revolution.

For a wave vector of the form $k_x = k \sin\theta$, $k_y = 0$, $k_z = k \cos\theta$, the sound velocities are given by

$$\rho c_t(\theta)^2 = C_{66}\sin^2\theta + C_{44}\cos^2\theta,$$

$$\rho c_\pm(\theta) = \frac{C_{11}\sin^2\theta + C_{33}\cos^2\theta + C_{44}}{2} \pm \sqrt{\left[\frac{(C_{11} - C_{44})\sin^2\theta + (C_{44} - C_{33})\cos^2\theta}{2}\right]^2 + (C_{13} + C_{44})^2\cos^2\theta\sin^2\theta}. \tag{6}$$

TABLE I. Calculated equilibrium lattice constants of studied wurtzite semiconductors compared to experimental values.

		SiC	GaN	InN	ZnO	CdSe
$a(\text{Å})$	Present	3.05	3.19	3.52	3.21	4.28
	Expt.	3.079[a]	3.19[b]	3.54[c]	3.26,[d] 3.253[a]	4.30,[e] 4.302[f]
c/a	Present	1.64	1.63	1.61	1.60	1.63
	Expt.	1.64[a]	1.627[b,g]	1.609[c]	1.60[a]	1.63[e,f]
u	Present	0.38	0.38	0.38	0.38	0.38
	Expt.	0.376[a]			0.382[a]	
$V(\text{Å}^3)$	Present	40.56	44.59	61.03	45.66	111.52

[a]XRD experiment by Schulz and Thiemann (Ref. 22).
[b]Synchrotron EDXD experiment by Xia *et al.* (Ref. 8).
[c]XRD experiment by Osamura *et al.* (Ref. 23).
[d]Synchrotron EDXD experiment by Desgreniers (Ref. 9).
[e]X-ray powder method by Hotje *et al.* (Ref. 24).
[f]XRD experiment by Sowa (Ref. 25).
[g]XAS experiment by Perlin *et al.* (Ref. 26).

This reduces to the in-plane limit for $\theta = \pi/2$ and along c limit for $\theta = 0$.

As will be seen below, at zero pressure, we find for all wurtzite crystals studied here that $C_{44} < C_{66}$. Hence, the lowest TA sound velocity occurs for polarization along c and a wave vector in the plane or a wave vector along c and polarization in the plane. Obviously C_{11} and C_{33} corresponding to the longitudinal sound velocities are significantly higher.

B. Relation to strains and phase transition

To see the relation between specific sound waves to the wurtzite-to-rocksalt phase transitions, we analyze the strains related to the phase transitions and strains induced by related sound waves. A pure c/a strain can be written as

$$\begin{bmatrix} -\epsilon/2 & 0 & 0 \\ 0 & -\epsilon/2 & 0 \\ 0 & 0 & \epsilon \end{bmatrix}. \tag{7}$$

For $\epsilon < 0$, it corresponds to a compression along c combined with an expansion in the plane in all directions such that the volume is preserved. This strain maintains the hexagonal symmetry of the crystal. As discussed, elsewhere, this transformation by itself could transform the wurtzite into the so-called HX-structure.[1,3] The latter differs from wurtzite by the fact that the layers become unbuckled or flat. At some critical value of this strain, the internal coordinate finds a minimum

energy for $u = 1/2$. Here, u is the conventional wurtzite internal parameters. The structure is fivefold coordinated from that point on.

The b/a distortion can be written as

$$\begin{bmatrix} -\epsilon & 0 & 0 \\ 0 & \epsilon & 0 \\ 0 & 0 & 0 \end{bmatrix}. \tag{8}$$

For $\epsilon > 0$, it corresponds to a compression along the chosen **b** direction and a corresponding expansion perpendicular to it in the plane and no distortion along **c**. This is a pure in-plane shear strain and corresponds to the limit of a transverse sound wave at 45° from it. In fact, for a wave written as $u_y(x) = u_y^0 \exp(ik_x x)$, the strain matrix has the form

$$\begin{bmatrix} 0 & \epsilon & 0 \\ \epsilon & 0 & 0 \\ 0 & 0 & 0 \end{bmatrix}, \tag{9}$$

which when diagonalized, gives a strain of the form of Eq. (8) with eigenvectors rotated 45° from the original axes in the plane. This means that the in-plane transverse acoustic sound waves at an angle 45° from the **b** directions correspond exactly to the symmetry breaking strain involved in the wurtzite to rocksalt transition, the strain we usually call the b/a strain. Thus the excitation of such sound waves could be viewed as the initial step in creating a b/a strain.

TABLE II. Bulk moduls B, its pressure derivative B' and elastic constants (in GPa) for wurtzite SiC (2H-SiC) compared with experimental data on 6H-SiC.

	B (GPa)	B'	C_{11}	C_{12}	C_{13}	C_{33}	C_{44}	C_{66}
Present	229	3.6	541	117	61	586	162	212
Expt.[a]	220		501	111	52	553	163	195

[a]Brillouin scattering experiment by Kamitani *et al.* (Ref. 27).

TABLE III. Bulk moduls B, its pressure derivative B' and elastic constants (in GPa) for wurtzite GaN compared with other calculations and experimental data.

	B (GPa)	B'	C_{11}	C_{12}	C_{13}	C_{33}	C_{44}	C_{66}
Present	207	4.2	367	135	98	409	98	116
Other[a]	207	4.5	346	148	105	389	76	99
Other[b]	202		367	135	103	405	95	116
Other[c]	201	4.3	366	139	98	403	97	
Expt.[d]	210		390	145	106	398	105	122
Expt.[e]	188	3.2						
Expt.[f]	245	4.0						
Expt.[g]	237	4.3						

[a]DFT(LDA) calculation by Kim *et al.* (Ref. 28).
[b]DFT(LDA) calculation by Wright (Ref. 16).
[c]DFT(LDA) calculation by Łepkowski *et al.* (Ref. 29).
[d]Brillouin scattering experiment by Polian *et al.* (Ref. 30).
[e]Synchrotron EDXD experiment by Xia *et al.* (Ref. 8).
[f]XAS experiment by Perlin *et al.* (Ref. 26).
[g]XRD experiment by Ueno *et al.* (Ref. 31).

The elastic constant defining the sound velocity for this type of acoustic sound waves is C_{66}. On the other hand, sound waves in the plane with displacement along the **c** axis or with wave vectors along **c** involve C_{44}. Now, because $C_{44} < C_{66}$, we can see that sound waves producing the b/a distortion are not the easiest to excite. For any finite wave vector, they require a bit higher energy. However, as we will see at some pressure the situation reverses and the C_{66} becomes the lower one. It is thus of interest to check whether the pressure where this crossing happens is in some ways related to the initiation of the phase transition.

III. COMPUTATIONAL METHOD

A. Elastic constant calculation

First, we briefly recall how to calculate elastic constants. The elastic energy (per unit volume) can be written as

$$U = \frac{1}{2}\epsilon_{ij}c_{ijkl}\epsilon_{kl}. \quad (10)$$

In Voigt notation, this becomes a matrix equation

$$U = \frac{1}{2}e_\lambda C_{\lambda\mu}e_\mu, \quad (11)$$

where $e_1 = \epsilon_{xx}$, $e_2 = \epsilon_{yy}$, $e_3 = \epsilon_{zz}$, $e_4 = 2\epsilon_{yz}$, $e_5 = 2\epsilon_{zx}$, and $e_6 = 2\epsilon_{xy}$. The elastic constants follow a similar contraction of indices rule, e.g., $C_{12} = c_{xxyy}$, $C_{44} = C_{yzyz}$, etc. Since for a hexagonal material there are 5 independent elastic constants, we can choose 5 independent strains, calculate their elastic energy per unit volume and write it in terms of the appropriate combination of elastic constants. We will obtain 5 equations with 5 unknowns from which the elastic constants can be extracted. Following Wright *et al.*,[16] we can use the following strains and obtain the combination of elastic constants corresponding to each of them:

$$e = (\epsilon, \epsilon, 0, 0, 0, 0) \rightarrow U = (C_{11} + C_{12})\epsilon^2,$$

$$e = (\epsilon, \epsilon, -2\epsilon, 0, 0, 0) \rightarrow U = (C_{11} + C_{12} - 4C_{13} + 2C_{33})\epsilon^2,$$

$$e = (0, 0, \epsilon, 0, 0, 0) \rightarrow U = \frac{1}{2}C_{33}\epsilon^2,$$

TABLE IV. Bulk moduls B, its pressure derivative B' and elastic constants (in GPa) for wurtzite InN compared with other calculations and experimental data.

	B (GPa)	B'	C_{11}	C_{12}	C_{13}	C_{33}	C_{44}	C_{66}
Present	151	4.8	232	115	96	239	52	59
Other[a]	147	3.4	220	120	91	249	36	50
Other[b]	141		223	115	92	224	48	54
Other[c]	146	3.9	229	120	95	234	49	
Expt.[d]	125	12.7						

[a]DFT(LDA) calculation by Kim *et al.* (Ref. 28).
[b]DFT(LDA) calculation by Wright (Ref. 16).
[c]DFT(LDA) calculation by Łepkowski *et al.* (Ref. 29).
[d]XRD experiment by Ueno *et al.* (Ref. 31).

TABLE V. Bulk moduls B, its pressure derivative B' and elastic constants (in GPa) for wurtzite ZnO compared with other calculations and experimental data.

	B (GPa)	B'	C_{11}	C_{12}	C_{13}	C_{33}	C_{44}	C_{66}
Present	162	4.0	227	133	118	232	40	47
Other[a]			217	117	121	225	50	50
Other[b]			231	111	104	183	72	60
Expt.[c]			206	118		211	44.3	44.6
Expt.[d]	181	4.0	209.7	121.1	105.1	210.9	42.47	44.3
Expt.[e]	206	4.0	207	117.7	106.1	209.5	44.8	44.65

[a]DFT(LDA) calculation by Gopal and Spaldin (Ref. 32); for C_{66} we used the value from $(C_{11}-C_{12})/2$.
[b]Atomistic simulation techniques based on the shell model calculation by Zaoui and Sekkal (Ref. 33).
[c]Brillouin scattering experiment Carlotti *et al.* (Ref. 34).
[d]B and B' from Synchrotron EDXD experiment by Decremps *et al.* (Ref. 10), C_{ij} from Ultrasound measurements by Bateman (Ref. 35).
[e]B and B' from Synchrotron EDXD experiment by Wu *et al.* (Ref. 11), C_{ij} from Kobiakov (Ref. 36).

$$e = (0,0,0,0,0,\epsilon) \rightarrow U = \frac{1}{4}(C_{11} - C_{12})\epsilon^2,$$

$$e = (0,0,0,\epsilon,\epsilon,0) \rightarrow U = C_{44}\epsilon^2. \qquad (12)$$

Note that for the calculations under each of these strains the internal coordinates are allowed to relax. Also, note that in the latter two cases, the hexagonal symmetry is broken by the distortion. Now, we want to calculate all these elastic constants as functions of pressure. We first determine the undistorted structure total energy as function of volume, and from $p = -\partial E/\partial V$ determine the pressure corresponding to each volume. In practice, we fit the Murnaghan equation of state to the $E(V)$ results and invert it to obtain volume as function of pressure.

At each pressure, and the corresponding volume, we apply the strains defined in Eq. (12) and, thus, obtain the elastic energy and consequently the pressure dependent elastic constants. Although some of these strains are volume conserving, e.g., the second and last two, the others are not and contain a hydrostatic component. Still, we use the volume at pressure p before applying the distortion in defining the energy per unit volume in those cases, which is sufficient because we only consider linear elasticity theory. In other words, we make a quasiharmonic approximation.

B. Computational details

To obtain all total energies required for the calculation of the elastic constants we use the Kohn-Sham density functional theory[17,18] in the local density approximation with the Perdew-Zunger parametrization of exchange and correlation.[19] The total energies are calculated using the full-potential linearized muffin-tin orbital method as described by Methfessel and van Schilfgaarde.[20] Well converged double basis sets are utilized and the Brillouin zone integrations are done using a $4 \times 4 \times 4$ Monkhorst-Pack sampling set.[21]

IV. RESULTS

A. Elastic constants and sound velocities at zero pressure

First, we give our results obtained for the equilibrium properties of the materials investigated here compared to experimental results. Table I shows the wurtzite lattice constants a, c/a, internal parameter u and the volume of the unit cell. Excellent agreement is obtained in all cases.

Tables II–VI give our results for the elastic constants at zero pressure compared with literature values. Overall, good agreement is obtained both with experimental and calculated values by others. For SiC, the wurtzite phase, which is usually called 2H-SiC is difficult to grow and, therefore, no experimental data on elastic constants of 2H-SiC are avail-

TABLE VI. Bulk moduls B, its pressure derivative B' and elastic constants (in GPa) for wurtzite CdSe compared with other calculations and experimental data.

	B (GPa)	B'	C_{11}	C_{12}	C_{13}	C_{33}	C_{44}	C_{66}
Present	60	4.6	80	47	40	92	15	17
Expt.[a]			74.9	46.09	39.36	84.51	13.15	14.40
Expt.[b]	53.3	4.0	74.1	45.2	39.3	83.6	13.17	14.45

[a]Ultrasound measurements by Cline *et al.* (Ref. 37).
[b]B and B' from XRD experiment by Sowa (Ref. 25), C_{ij} from resonance measurement by Berlincourt *et al.* (Ref. 38).

TABLE VII. The second-order polynomials describing the pressure dependence of selected elastic constants for SiC, GaN, InN, ZnO, and CdSe. The polynomials were obtained from a fit to the calculated results at discrete pressures. The pressure, P, is in GPa and the ranges used for the fit are shown in the last column.

	Elastic constant (GPa)	P range (GPa)
SiC	$C_{11}=542+4.79P-0.0140P^2$	0–150
	$C_{33}=586+8.02P-0.0262P^2$	
	$C_{44}=163+0.91P-0.0015P^2$	
	$C_{66}=213+0.83P-0.0038P^2$	
GaN	$C_{11}=369+3.74P-0.0135P^2$	0–100
	$C_{33}=405+4.54P-0.0083P^2$	
	$C_{44}=98+0.58P-0.0023P^2$	
	$C_{66}=117+0.48P-0.0052P^2$	
InN	$C_{11}=232+3.86P-0.017P^2$	0–40
	$C_{33}=240+4.72P-0.036P^2$	
	$C_{44}=52+0.24P-0.001P^2$	
	$C_{66}=58-0.08P-0.005P^2$	
ZnO	$C_{11}=227+1.62P+0.073P^2$	0–16
	$C_{33}=232+1.16P+0.165P^2$	
	$C_{44}=40+0.03P-0.005P^2$	
	$C_{66}=47-0.86P+0.006P^2$	
CdSe	$C_{11}=81+3.53P-0.075P^2$	0–10
	$C_{33}=91+5.49P-0.197P^2$	
	$C_{44}=15+0.05P-0.026P^2$	
	$C_{66}=17+0.11P-0.111P^2$	

able. However, one finds that the elastic constants for 4H and 6H SiC, two slightly different polytypes, are very close to each other. We thus compare with the values for 6H.

The sound velocities at zero pressure extracted from these at zero pressure are given in Tables VIII for wave vector directions along [001] and [100]. As discussed above, the sound velocities for wave vectors in the plane are independent of the direction angle in the plane. For wave vectors that are intermediate between in-plane and perpendicular to the basal plane, the sound velocities have a well defined angular dependence given in Eq. (6).

B. Pressure dependent elastic constants and sound velocities

In Figs. 1 and 2, we show the pressure dependence of the elastic constants and sound velocities, respectively. The dots show the first principles results for the given pressures. The lines are the second-order polynomial fit to the results. The fitting results (quadratic equations) for the elastic constants are shown in Table VII. We can see quite different behaviors depending on the material and the elastic constants considered. The compressional moduli, C_{11} and C_{33} are increasing with pressure but for most materials we see that C_{33} curves downward at higher pressures. The exception is ZnO, where it curves upward. For SiC and GaN, the shear type elastic constant C_{66} initially increases but goes through a maximum and then bends down. For InN, ZnO, and CdSe, it monotoni-

cally decreases with increasing pressure starting from zero pressure. In ZnO, it slightly curves upward instead of downward. The C_{44} changes from increasing with pressure in SiC, GaN, and InN, to staying almost constant in ZnO and decreasing in CdSe. Since the sound velocities are directly derived from these elastic constants, similar behavior is also observed. Their behavior is, however, slightly different because the mass density involved in the sound velocity also changes as a function of pressure. To the best of our knowledge, no measurements of the sound velocities or elastic constants as function of pressure are available for these materials. Our calculations predict and interesting variety of behaviors, which would be beneficial to verify experimentally. The elastic constants as function of pressure were previously calculated using DFT by Łepkowski et al.[29] for GaN and InN. They extracted the linear and quadratic pressure coefficients. Their results for the two materials are comparable to ours (as shown in Fig. 1), but we considered a larger pressure range. For ZnO, the elastic constants as function of pressure were previously calculated by Zaoui and Sekkal[33] but using only pair potential shell model level of calculations. For CdSe, the elastic constants as a function of pressure were previously studied for only the zincblende phase by Deligoz et al.[41]

C. Relation to phase transition

As discussed in the introduction, it is of interest to consider the pressure where C_{44} crosses with C_{66}. Above this pressure, transverse sound waves in the basal plane should become easier to excite than sound waves related to c/a strains. The transverse sound waves are closely related to the symmetry breaking b/a strain leading to the phase transition, while the sound waves related to c/a strains preserve the hexagonal symmetry. In order to initiate the phase transition, it might seem important to break the symmetry.

We thus consider the pressures where these two shear elastic constants cross, or equivalently where the sound velocities cross. The values are summarized in Table IX along with the equilibrium phase transition pressure (the pressure where the calculated enthalpies of the rocksalt and wurtzite phases are equal) and the experimentally observed phase transition pressures. We estimate the uncertainty on these crossover pressures to be of the order a few GPa.

We can see that for SiC, GaN, and CdSe the cross-over pressure is higher than the actual transition pressure, while the equilibrium transition pressure is lower than the experimental value. The latter has been previously attributed to the existence of a barrier between the two phases at the transition pressure. It can be considered a kinetic effect. For InN, our calculated equilibrium transition pressure is in good agreement with the experimental value while the crossover pressure is higher. Note that, generally the InN crystal quality is quite poor so the measurement of this particular material might contain a sizable error bar. For ZnO, the calculated crossover pressure is slightly higher than the calculated equilibrium transition pressure. The observed experimental transition pressures of 9.1–10.5 GPa exceeds both of these values but by only ≈ 1 GPa, which is well within the computational error bar.

TABLE VIII. Sound velocities (in km/s) at zero pressure for SiC, GaN, InN, ZnO, and CdSe calculated from the elastic constants. $\hat{k}$ is the wave vector and $\boldsymbol{n}$ is the polarization. The Phillips ionicity parameters (f_i) are also listed.

	f_i	$\hat{k}\rightarrow$ $\boldsymbol{n}\rightarrow$	[100] [100]	[001]	[010]	[001] [001]	[100]
SiC	0.177	Present	12.8	7.0	8.0	13.4	7.0
		Other[a]	12.5	7.1	7.8	13.1	7.1
		Expt.[b]				12.21	7.69
		Expt.[c]				13.27	7.24
GaN	0.500	Present	7.67	3.96	4.32	8.10	3.96
		Other[d]	8.0	4.1	6.3	8.0	4.1
InN	0.578	Present	5.76	2.73	2.89	5.84	2.73
		Other[d]	5.3	1.2	2.5	5.2	1.2
ZnO	0.616	Present	6.23	2.61	2.83	6.30	2.61
		Other[e]	6.08	2.92	2.92	6.19	2.92
		Expt.[f]	6.08	2.73	2.79	6.10	2.73
CdSe	0.699	Present	3.76	1.62	1.71	4.02	1.62
		Expt.[g]	3.63	1.52	1.59	3.86	1.52

[a]Calculated from elastic constants by Kamitani *et al.* (Ref. 27).
[b]Ultrasound measurements by Schreiber *et al.* (Ref. 39).
[c]Raman measurements on various polytypes, Feldman *et al.* (Ref. 40).
[d]Calculated from elastic constants by Wright *et al.* (Ref. 16).
[e]Calculated from elastic constants by Gopal and Spaldin (Ref. 32).
[f]Ultrasound measurements by Bateman (Ref. 35).
[g]Ultrasound measurements by Cline *et al.* (Ref. 37).

As discussed before by Limpijumnong and Jungthawan,[42] for more ionic or softer tetrahedral semiconductors, the calculated transition pressures are close to the experimental ones, while for the stiffer ones, the calculated equilibrium transition pressures are significantly underestimated. The underestimation of the calculated transition pressure was attributed to the kinetic barrier in the actual transition. Here, we observe some relationship between the crossover pressure and the transition pressure. We find that the crossover pressure might serve as an upper limit of the transition pressure. In addition, we propose that in combination with the calculated equilibrium transition pressure it can be used to improve the prediction of the actual transition pressure, as will be described later. This observation is especially useful for the stiffer materials, for e.g., SiC and GaN in our present study, where the calculated transition pressure is significantly underestimated.

Above the crossover pressure, the transverse sound waves associated with C_{66} turn easier to excite than sound waves associated with C_{44}. However, even before the C_{66} and C_{44} cross, one may expect that as they approach each other it already become probable to excite the transverse acoustic waves at finite temperature and ultimately initiate the transition. Note that in this model, we consider the excitation of such modes as the triggering effect. Once the system starts exhibiting a strain of this type, the c/a distortion follows it through the anharmonic interactions between these two types of modes. This then leads the system toward the barrier transition point which separates the wurtzite from the rocksalt

valley as can be seen from the energy landscapes given in Sarasamak *et al.*[3] Note that the excitation energy of the phonon with the wavelength of about 1 nm can be estimated from $\hbar\omega=\hbar vk\approx 10\text{–}20$ meV, which is comparable to the thermal energy at room temperature. This means that within a nucleation region of about 1 nm the homogeneous transformation might be triggered already at room temperature and serves as a nucleus of the new phase.

From Table IX, it is clear that the calculated equilibrium transition pressure p_t generally underestimates the experimentally observed pressure p_u by about as much percentage wise as the crossover pressure overestimates it. Therefore, we propose that a good and simple approximation to the experimental pressure would be $(p_t+p_c)/2$. Our calculated values of $(p_t+p_c)/2$ are tabulated in Table IX and are very close the experimental values for SiC and GaN. As a further test that this gives a useful estimate in particular for cases where there is evidence of a significant transition kinetic barrier, we consider AlN. Based, on the data of Łepkowski *et al.*[29] for the pressure-dependent elastic constants, we obtain the crossover pressure to be 39.6 GPa. The calculated equilibrium transition pressure by Serrano *et al.*[43] is 9.2 GPa. This gives as estimate for the actual transition pressure ($p_t+p_c)/2=24.4$ GPa. The experimental value by Ueno *et al.*[44] is 22.9 GPa.

Note that the correlation found here between the sound wave excitations of a particular symmetry and the transition pressures is suggestive but not a complete proof of their roles in the actual transition processes. The actual transition re-
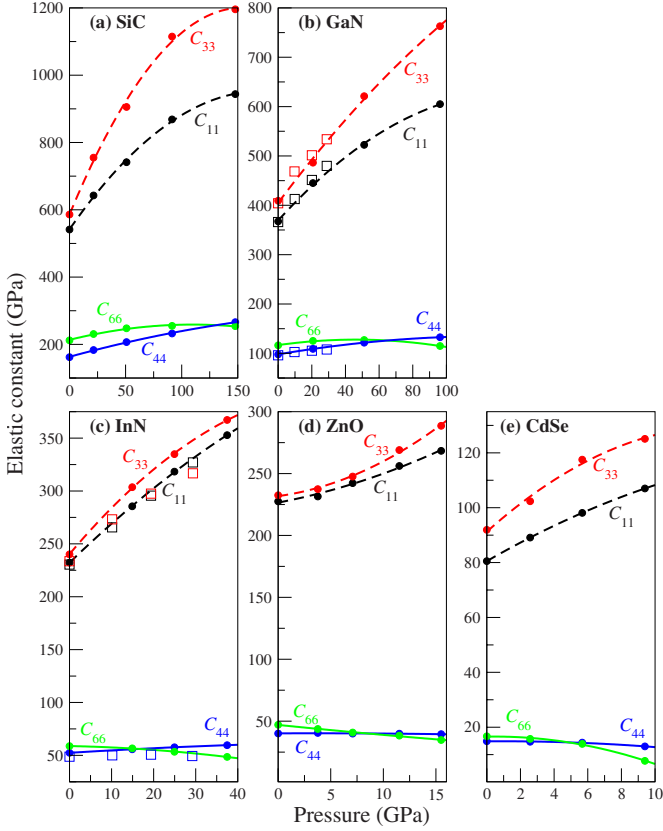
FIG. 1. (Color online) Calculated pressure dependence of the elastic constants in (a) SiC, (b) GaN, (c) InN, (d) ZnO, and (e) CdSe. In (b) and (c), the square symbols show the calculated results by Łepkowski *et al.* (Ref. 29).

FIG. 2. (Color online) Calculated pressure dependence of the sound velocities in (a) SiC, (b) GaN, (c) InN, (d) ZnO, and (e) CdSe.

quires the occurrence of both in-plane and perpendicular to the plane types of strain to reach the transition barrier. The transition barrier height[42] and the overall enthalpy landscape[3] therefore play a significant role in the phase transformation process.

D. Trends with ionicity

Because we have systematically calculated several wurtzite crystals, i.e., SiC, GaN, InN, ZnO, and CdSe, that spanned a wide range of ionicity, we can study the trend of the elastic constants and sound velocities with the material's ionicity. To quantify the ionicity of these materials, we choose to use Phillips' ionic scale[45] (f_i) which has the range between 0 (completely covalent) and 1 (completely ionic). This scale is based on optical properties of the semiconductors and has been shown in the past to be related to the preference for octahedral and tetrahedral bonding and the transition pressures.[46,47] The values of f_i for the materials studied are listed in Table VIII. In Fig. 3(a), we plotted the elastic constants as a function of f_i at zero pressure. We can see that all four elastic constants monotonically decrease as f_i increases. The same holds true at finite pressures. For the sound velocity, the general trend also follows that of the elastic constant because the sound velocity is proportional to the square root of the corresponding elastic constant as
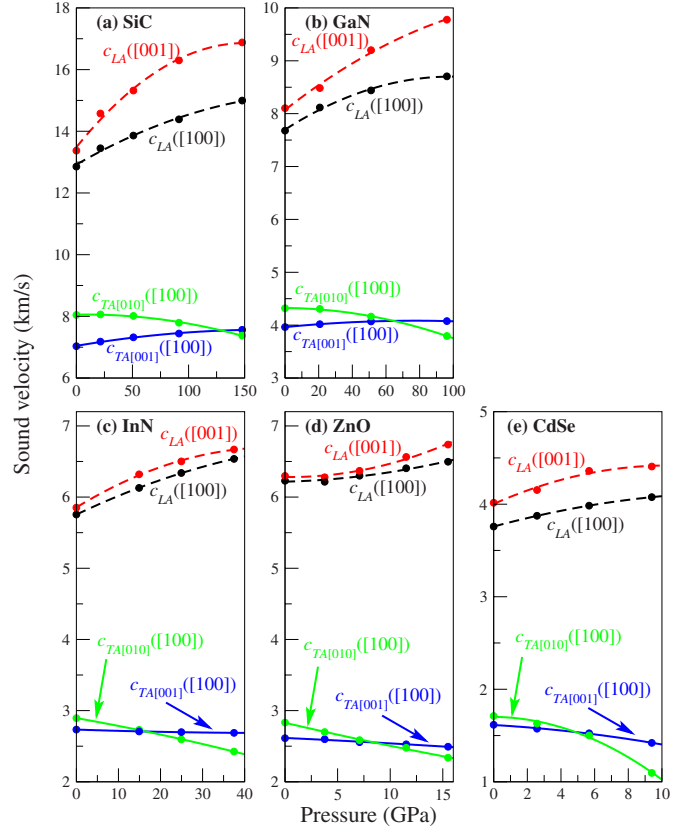
shown in Eq. (4) and (5). In Fig. 3(b), the sound velocities are shown as a function of f_i. We note that in both the LA sound velocities and compressional elastic constants, InN dips a bit below the trend lines. This may be indicative of the

TABLE IX. Crossover pressure p_c where $C_{44}=C_{66}$, calculated equilibrium phase transition pressure p_t (taken from Ref. 3, except for AlN) and experimental transition pressures p_u for wurtzite-to-rocksalt transition, all in GPa, for SiC, GaN, AlN, InN, ZnO, and CdSe.

	p_c	p_t	$(p_t+p_c)/2$	p_u
SiC	131.1	64.9	98.0	100[a]
GaN	65.5	44.1	54.8	52.2[b]
AlN	39.6[c]	9.2[d]	24.4	22.9[e]
InN	15.7	12.2	13.9	12.1[b]
ZnO	8.8	8.2	8.4	9.1[f], 10.5[g]
CdSe	5.2	2.2	3.7	4.0[h]

[a]XRD experiment by Yoshida *et al.* (Ref. 50).
[b]XRD experiment by Ueno *et al.* (Ref. 31).
[c]Calculated here from data of Łepkowski *et al.* (Ref. 29).
[d]From Serrano *et al.* (Ref. 43).
[e]From Ueno *et al.* (Ref. 44).
[f]Synchrotron XRD experiment by Desgreniers (Ref. 9).
[g]Synchrotron EDXD experiment by Kumar *et al.* (Ref. 51).
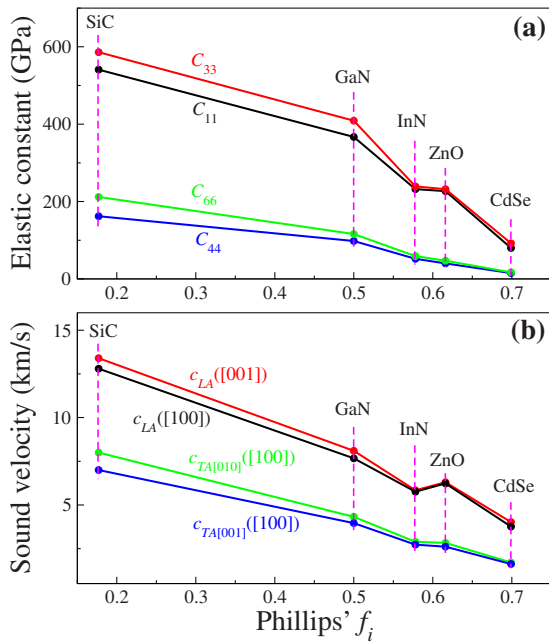[h]Synchrotron XRD experiment by Wang *et al.* (Ref. 52).

FIG. 3. (Color online) Calculated (a) elastic constants and (b) sound velocities as a function of ionicity (Phillips' scale) at zero pressure ($P=0$ GPa).

fact that the ionicity of InN is underestimated by the Phillips scale. InN has a larger ionicity in the Garcia scale.[48] The ionicities of the III-nitrides were discussed in Ref. [49]

V. CONCLUSIONS

We presented the calculated elastic constants and sound velocities in wurtzite SiC, GaN, InN, ZnO, and CdSe as functions of pressure. We found interesting nonlinear behavior of the elastic constants and sound velocities with pressure that is quite different in the different materials. We also showed that the elastic constants are lower in materials with higher ionicity. Generally, the sound velocities follow the same trend as the elastic constants, i.e., lower in materials with higher ionicity. The pressure at which the C_{44} and C_{66} shear elastic constants cross are investigated. When C_{66} becomes lower, it should be easier to excite the symmetry breaking strain mode related to the wurtzite-to-rocksalt phase transition. We found that the crossover pressure is generally higher than the experimental transition pressure and explained it by the fact that finite temperature fluctuations make it possible to excite the required modes even before the two sound velocities cross. We proposed the average of the crossover and calculated equilibrium transition pressures to be a good estimate for the experimental transition pressure in cases where there is a significant transition enthalpy barrier. The results suggest that the in-plane transverse sound waves could play a significant role in triggering the phase transition. Of course, the details near the transition point, the height of the barrier, and the coupling of the in and out of plane acoustic modes, which are both required to reach the transition point, are also important for the transition to take place.

[1] S. Limpijumnong and W. R. L. Lambrecht, Phys. Rev. Lett. **86**, 91 (2001a).

[2] S. Limpijumnong and W. R. L. Lambrecht, Phys. Rev. B **63**, 104103 (2001b).

[3] K. Sarasamak, A. J. Kulkarni, M. Zhou, and S. Limpijumnong, Phys. Rev. B **77**, 024104 (2008).

[4] M. Catti, Phys. Rev. Lett. **87**, 035504 (2001).

[5] M. S. Miao, M. Prikhodko, and W. R. L. Lambrecht, Phys. Rev. Lett. **88**, 189601 (2002).

[6] M. S. Miao, M. Prikhodko, and W. R. L. Lambrecht, Phys. Rev. B **66**, 064107 (2002).

[7] M. S. Miao and W. R. L. Lambrecht, Phys. Rev. Lett. **94**, 225501 (2005).

[8] H. Xia, Q. Xia, and A. L. Ruoff, Phys. Rev. B **47**, 12925 (1993).

[9] S. Desgreniers, Phys. Rev. B **58**, 14102 (1998).

[10] F. Decremps, F. Datchi, A. M. Saitta, A. Polian, S. Pascarelli, A. Di Cicco, J. P. Itié, and F. Baudelet, Phys. Rev. B **68**, 104101 (2003).

[11] X. Wu, Z. Wu, L. Guo, C. Liu, J. Liu, X. Li, and H. Xu, Solid State Commun. **135**, 780 (2005).

[12] S. E. Boulfelfel, D. Zahn, Y. Grin, and S. Leoni, Phys. Rev. Lett. **99**, 125505 (2007).

[13] M. Prikhodko, M. S. Miao, and W. R. L. Lambrecht, Phys. Rev. B **66**, 125201 (2002).

[14] L. D. Landau and E. M. Lifschitz, *Theory of Elasticity, Course of Theoretical Physics* (Pergamon Press, New York, 1980), Chap. 3, Vol. 7.

[15] M. Rosen and H. Klimker, Phys. Rev. B **1**, 3748 (1970).

[16] A. F. Wright, J. Appl. Phys. **82**, 2833 (1997).

[17] P. Hohenberg and W. Kohn, Phys. Rev. **136**, B864 (1964).

[18] W. Kohn and L. J. Sham, Phys. Rev. **140**, A1133 (1965).

[19] J. P. Perdew and A. Zunger, Phys. Rev. B **23**, 5048 (1981).

[20] M. Methfessel, M. van Schilfgaarde, and R. A. Casali, in *Electronic Structure and Physical Properties of Solids. The Uses of the LMTO Method, Lecture Notes in Physics*, edited by H. Dreyssé (Springer Verlag, Berlin, 2000), Vol. 535, p. 114.

[21] H. J. Monkhorst and J. D. Pack, Phys. Rev. B **13**, 5188 (1976).

[22] H. Schulz and K. H. Thiemann, Solid State Commun. **32**, 783 (1979).

[23] K. Osamura, S. Naka, and Y. Murakami, J. Appl. Phys. **46**, 3432 (1975).

[24] U. Hotje, C. Rose, and M. Binnewies, Solid State Sci. **5**, 1259 (2003).

[25] H. Sowa, Solid State Sci. **7**, 1384 (2005).

[26] P. Perlin, C. Jauberthie-Carillon, J. P. Itie, A. San Miguel, I. Grzegory, and A. Polian, Phys. Rev. B **45**, 83 (1992).

[27] K. Kamitani, M. Grimsditch, J. C. Nipko, C.-K. Loong, M. Okada, and I. Kimura, J. Appl. Phys. **82**, 3152 (1997).

[28] K. Kim, W. R. L. Lambrecht, and B. Segall, Phys. Rev. B **56**, 7018 (1997).

[29] S. P. Łepkowski, J. A. Majewski, and G. Jurczak, Phys. Rev. B **72**, 245201 (2005).

[30] A. Polian, M. Grimsditch, and I. Grzegory, J. Appl. Phys. **79**, 3343 (1996).

[31] M. Ueno, M. Yoshida, A. Onodera, O. Shimomura, and K. Takemura, Phys. Rev. B **49**, 14 (1994).

[32] P. Gopal and N. A. Spaldin, J. Electron. Mater. **35**, 538 (2006).

[33] A. Zaoui and W. Sekkal, Phys. Rev. B **66**, 174106 (2002).

[34] G. Carlotti, D. Fioretto, G. Socino, and E. Verona, J. Phys.: Condens. Matter **7**, 9147 (1995).

[35] T. B. Bateman, J. Appl. Phys. **33**, 3309 (1962).

[36] J. B. Kobiakov, Solid State Commun. **35**, 305 (1980).

[37] C. F. Cline, H. L. Dunegan, and G. W. Henderson, J. Appl. Phys. **38**, 1944 (1967).

[38] D. Berlincourt, H. Jaffe, and L. R. Shiozawa, Phys. Rev. **129**, 1009 (1963).

[39] E. Schreiber and N. Soga, J. Am. Ceram. Soc. **49**, 342 (2006).

[40] D. W. Feldman, J. H. Parker, W. J. Choyke, and L. Patrick, Phys. Rev. **173**, 787 (1968).

[41] E. Deligoz, K. Colakoglu, and Y. Ciftci, Physica B **373**, 124 (2006).

[42] S. Limpijumnong and S. Jungthawan, Phys. Rev. B **70**, 054104 (2004).

[43] J. Serrano, A. Rubio, E. Hernández, A. Munoz, and A. Mujica, Phys. Rev. B **62**, 16612 (2000).

[44] M. Ueno, A. Onodera, O. Shimomura, and K. Takemura, Phys. Rev. B **45**, 10123 (1992).

[45] J. C. Phillips, Rev. Mod. Phys. **42**, 317 (1970).

[46] J. R. Chelikowsky and J. K. Burdett, Phys. Rev. Lett. **56**, 961 (1986).

[47] N. E. Christensen, S. Satpathy, and Z. Pawlowska, Phys. Rev. B **36**, 1032 (1987).

[48] A. García and M. L. Cohen, Phys. Rev. B **47**, 4215 (1993).

[49] W. R. L. Lambrecht, in *Gallium Nitride (GaN) I, Semiconductors and Semimetals*, edited by J. I. Pankove and T. D. Moustakas (Academic Press, San Diego, 1998), Vol. 50.

[50] M. Yoshida, A. Onodera, M. Ueno, K. Takemura, and O. Shimomura, Phys. Rev. B **48**, 10587 (1993).

[51] R. S. Kumar, A. L. Cornelius, and M. F. Nicol, Curr. Appl. Phys. **7**, 135 (2007).

[52] Z. Wang, K. Finkelstein, C. Ma, and Z. L. Wang, Appl. Phys. Lett. **90**, 113115 (2007).

X-ray absorption spectroscopy of indium nitride, indium oxide, and their alloys

Jiraroj T-Thienprasert [a,b], Saroj Rujirawat [c], Jiti Nukeaw [d], Sukit Limpijumnong [b,c,*]

[a] Department of Physics, Faculty of Science, Kasetsart University, Bangkok 10900, Thailand
[b] Thailand Center of Excellence in Physics (ThEP Center), Commission on Higher Education, Bangkok 10400, Thailand
[c] School of Physics, Suranaree University of Technology and Synchrotron Light Research Institute, Nakhon Ratchasima 30000, Thailand
[d] Nanotechnology Research Center of KMITL and Department of Applied Physics, King Mongkut's Institute of Technology Ladkrabang, Bangkok 10520, Thailand

ARTICLE INFO

ABSTRACT

To investigate the local structure of InN, In_2O_3 and their alloys, synchrotron (In L_3-edge) X-ray absorption near edge structures (XANES) of indium oxynitride samples with varied O contents are used in conjunction with first-principles calculations. A good agreement between the measured and simulated spectra is obtained. It is found that the spectra are sensitive to the coordination number of the In atoms, i.e., four-fold for InN-like structures and sixfold for In_2O_3-like structures. Moreover, the spectra are quite insensitive to the species (N or O) around In. The calculated band structures and density of states are also presented and discussed.

© 2010 Elsevier B.V. All rights reserved.

1. Introduction

Indium oxynitride is an alloy between indium nitride (InN) and indium oxide (In_2O_3). The crystal structures of InN and In_2O_3 are very different, i.e., wurtzite for InN and bixbyite for In_2O_3. The band gap of InN has been mistaken to be ~1.9 eV for a long time (see the discussion in Refs. [1,2]). Recently, a high quality InN has been obtained by molecular beam epitaxy (MBE) and the actual InN bandgap of ~0.7 eV has been observed [3,4]. In addition, the bandgap of In_2O_3 remains contentious with the reported values ranging from ~3.6 eV [5] to below 3.0 eV [6]. The nitrogen incorporation in In_2O_3 can reduce the bandgap into the visible range, which will be beneficial for solar photocatalytic applications such as hydrogen production from water [7]. Because bandgap of indium oxynitride can vary in a very wide range, this class of alloys is widely used for optical coating applications despite its poor crystal quality, especially when it is grown by traditional techniques such as RF magnetron sputtering [8].

In alloys with low oxygen content, O atoms can substitute on the N site in the wurtzite InN crystal structure [9]. For alloys with high oxygen content, the crystal structure is still unclear. Note that the O content that can substitute on the N site in the wurtzite structure would depend strongly on the growth techniques and conditions. In the past, N K-edge XANES measurement has been performed to study the crystal structure of this class of alloys. Unfortunately, probing the local structure of anions in this alloy system is not very useful because the local structure of the anion in both wurtzite and bixbyite structures are fourfold coordinated. On the other hand, the local geometry of In in wurtzite and bixbyite structures are different, i.e., fourfold in InN and sixfold in In_2O_3. As we have previously illustrated [10], probing the local structure of In in this alloy system can give useful information on the local structure of the alloys. In our published Letter [10], we employed In L_3-edge XANES spectra in conjunction with *ab initio* XANES simulation to characterize the indium oxynitride thin films with varied compositions. We have shown that XANES is a powerful tool to determine the local structure of indium oxynitride films. Here, the detailed results that have not been presented in our Letter due to limited space and additional results on the simulation of In surrounded by both oxygen and nitrogen neighbors (mixed neighbors) are presented.

2. Methods

2.1. Experimental details

Indium oxynitride films were grown by RF magnetron sputtering at room temperature using a technique called reactive gas timing [11,12]. Before the growth process, the chamber was pre-evacuated to ~10^{-5} Pa. After that, the N_2 and O_2 gas were flown interchangeably at the flow rate of 10 standard cm^3 per minute (sccm) onto the 99.999% purity In target. The sputtering gas pressures were set at 0.34 Pa and 0.32 Pa for N_2 and O_2, respectively. The indium oxynitride samples with varied O and N contents can be obtained by controlling N_2 and O_2 gas timing [10]. The optical

bandgap and the O:In composition of all samples were measured by UV–visible and Auger electron spectroscopy (AES), respectively [10].

The In L_3-edge XANES measurements [10] were performed in the fluorescent mode with a 13-component Ge detector (Canbera) at the X-ray absorption spectroscopy beamline (BL-8) of the Siam Photon Source (electron energy of 1.2 GeV, beam current 120–80 mA), Synchrotron Light Research Institute, Thailand. A double crystal monochromator with Si (1 1 1) was used to scan the synchrotron X-ray with the photon energy step of 0.25 eV in the range of 3640–3950 eV, covering the XANES region of In L_3-edge.

2.2. Computational details

In order to understand the local microscopic structure of indium oxynitride, first-principles XANES simulations of wurtzite InN, bixbyite In_2O_3, and different alloy models of $(InN)_x(InO_{0.5})_{1-x}$ were performed. The detailed crystal geometries were optimized based on first-principles density functional calculations. The density functional theory with local density approximation (LDA) and ultrasoft Vanderbilt pseudo potentials (USPP) [13] as implemented in the VASP codes were used [14,15]. The cutoff energy for the plane wave basis set was 400 eV. For k-point sampling, Monkhorst–Pack scheme [16] was used for Brillouin zone integra-
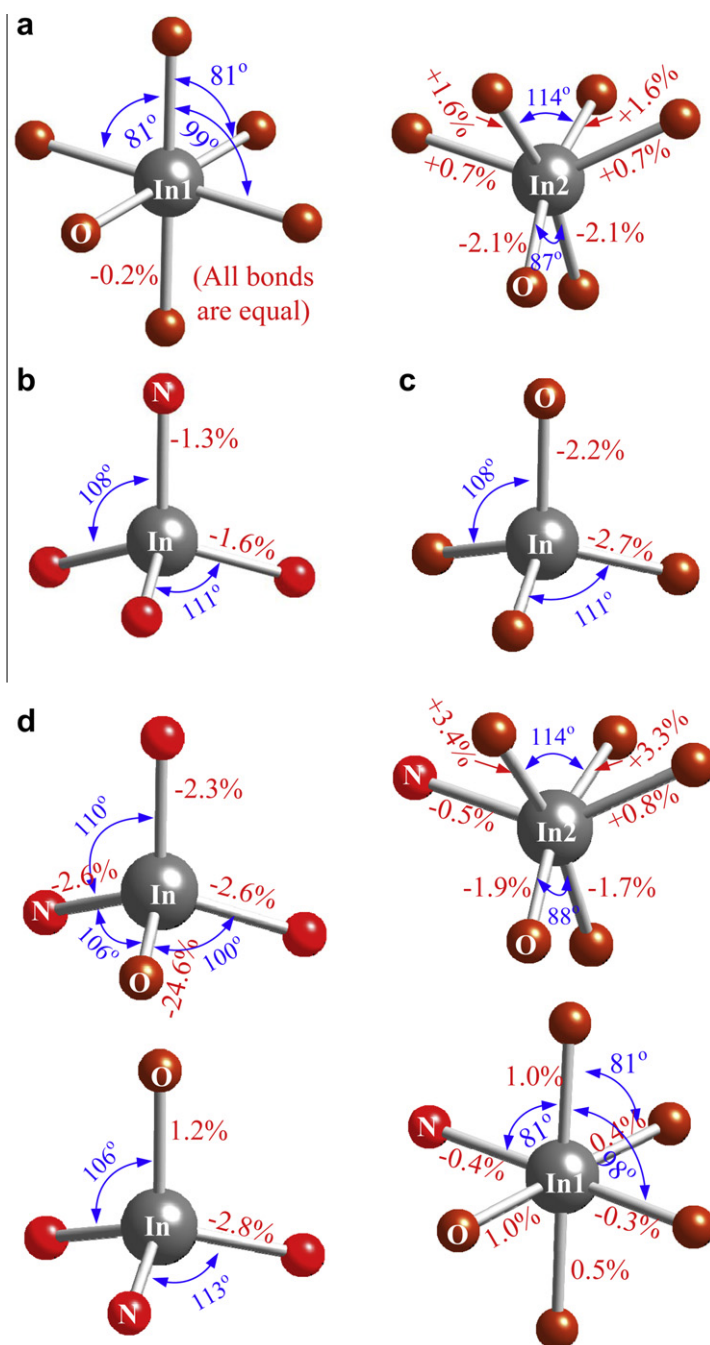

Fig. 1. The local structures around In atoms in (a) pure bixbyite In_2O_3, (b) pure wurtzite InN, (c) wurtzite InN with four surrounding N atoms replaced by O atoms, and (d) wurtzite InN with one surrounding N atom replaced by an O atom (left) and bixbyite In_2O_3 with one O atom replaced by a N atom (right). All bond distances are given as a percentage difference from an average In_2O_3 bond distance (d_{calc} = 2.170 Å).

tion ($7 \times 7 \times 7$ for four-atom wurtzite cell, $2 \times 2 \times 2$ for 72-atom wurtzite supercell, and $3 \times 3 \times 3$ for 40-atom bixbyite cell). All atoms were allowed to relax until the residue forces acting on each atom were less than 10^{-3} eV/Å. The volumes of the cells used in the calculations are based on the fully relaxed lattice constant of bulk wurtzite InN (or bixbyite In_2O_3). The relaxed local structures surrounding In atoms in InN, In_2O_3, and selected InN_xO_{1-x} alloy models are shown in Fig. 1. All In atoms in wurtzite InN crystal are equivalent. However, there are two species of In atoms in In_2O_3 (labeled In1 and In2) with the composition ratio of 1:3. For the alloys, a few selected local structure models surrounding an In atom were tested. For the first model, we replaced four N atoms surrounding an In atom with O atoms in a wurtzite-InN supercell. For the second model, only one N atom was replaced by an O atom in a wurtzite-InN supercell. For the third model, only one O atom was replaced by a N atom in a bixbyite In_2O_3 cell. These tests were performed to see the effect of neighboring specie on the simulated XANES spectrum. Note that, to obtain the proper local geometries, after the replacement of N by O (or O by N in the third model), all atoms in the cell were allowed to relax by first-principles calculations before they were further used in XANES calculations.

To simulate *ab initio* XANES of InN, In_2O_3, and InN_xO_{1-x} alloys, we used the FEFF8.2 codes [17,18]. The codes utilize a full multiple scattering approach based on *ab initio* overlapping muffin-tin potentials. The muffin-tin potentials used in FEFF codes are obtained using self-consistent calculations with Hedin–Lundqvist exchange–correlation function [19]. The self-consistent calculations were performed in the sphere radius 4 Å (containing approximately 40-atoms) around the absorber In atom. The full multiple scattering calculations include all possible paths within a larger cluster radius of 7.4 Å (containing approximately 140 atoms) [10].

The electronic transitions associated with the XANES measurements must follow the dipole selection rule. Consequently, L_3-edge XANES corresponds to the $(s + d)$-partial density of state (PDOS). As a result, PDOS can also be used to compare with the XANES mea-

surement [20]. An X-ray absorbance $\mu(\omega)$ is given by the Fermi's golden rule,

$$\mu \propto \sum_f |\langle f|D|i \rangle|^2 \delta(E_i - E_f + \omega), \tag{1}$$

where $|i\rangle$, $|f\rangle$, E_i, and E_f are the initial and final states and their energies, respectively. ω and D are the photon frequency and dipole operator.

3. Results and discussion

3.1. Electronic structures of InN, In_2O_3, and $InN_{1-x}O_x$ alloy

The calculated cell parameters of wurtzite InN are $a = 3.51$ Å and $c/a = 1.60$ Å (these are to compare with the experimental values of 3.533 Å and 1.611 Å, respectively [21]). We obtained a slightly negative bandgap using first-principles calculations as illustrated in Fig. 2a. The density of states (DOS) are shown in the top panel of Fig. 3 with site decomposed partial DOS of In and N in the middle panel and bottom panel, respectively. From PDOS, it is clear that the lowest narrow band centered at -13 eV is mainly composed of N s and the higher valence band (VB) states located at around -5 to 0 eV are composed of In s, p and N p with a small degree of In d. The lower conduction band (CB) states located at 0–12 eV are the mixing of In p and N p with some degree of In s and N s, whereas the higher CB states (above 12 eV) are mainly In d.

For In_2O_3, the bixbyite unit cell is composed of 40-atom with the calculated lattice constant of $\sim$10.07 Å (this is to compare with the experimental value of 10.117 Å [22]). We obtained the calculated bandgap of 1.26 eV which is in agreement with the calculation value of 1.21 eV obtained by Erhart [23]. The calculated bandgaps of InN and In_2O_3 are lower than those of experimental values because of the well know DFT problems. The band structure and the DOS are shown in Figs. 2b and 4, respectively. The symmetry points labeled in the band structure plot is used according to
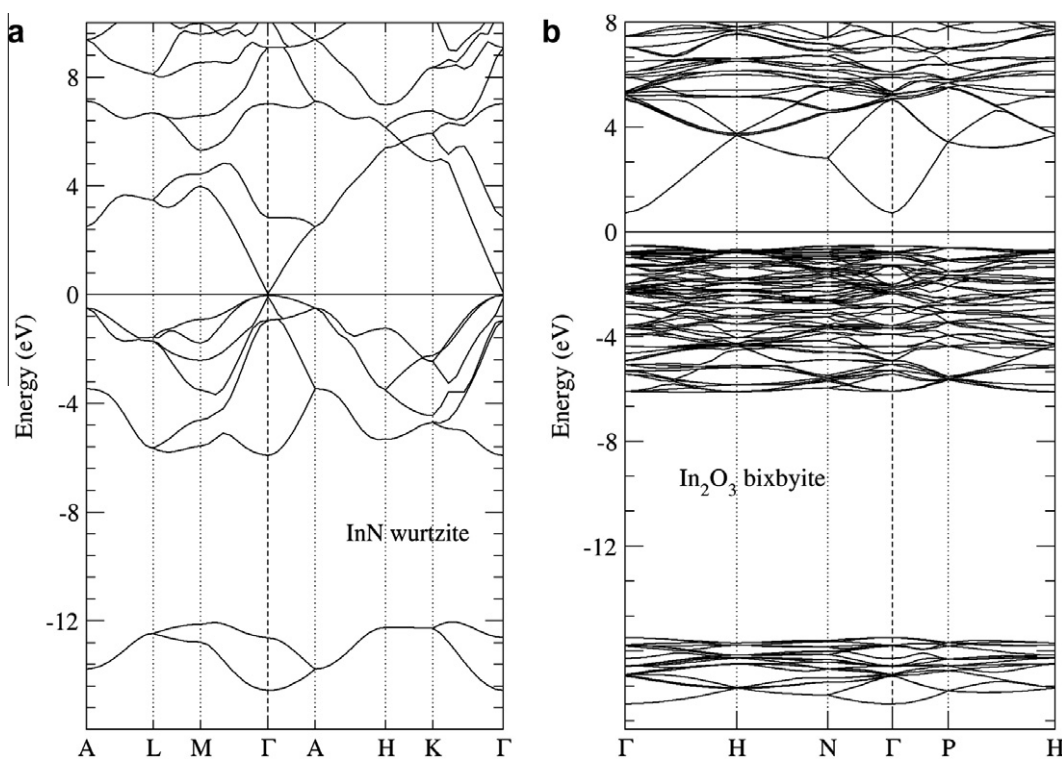

Fig. 2. Band structures of (a) wurtzite InN and (b) bixbyite In_2O_3. The energy is referenced to the Fermi level.
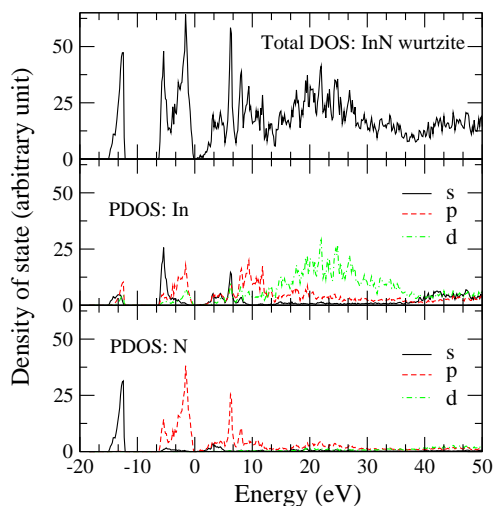
Fig. 3. The calculated density of states (DOS) of wurtzite InN: (top panel) the total DOS, (middle and bottom panels) the site and angular momentum projected partial density of states (PDOS) of In and N atoms.
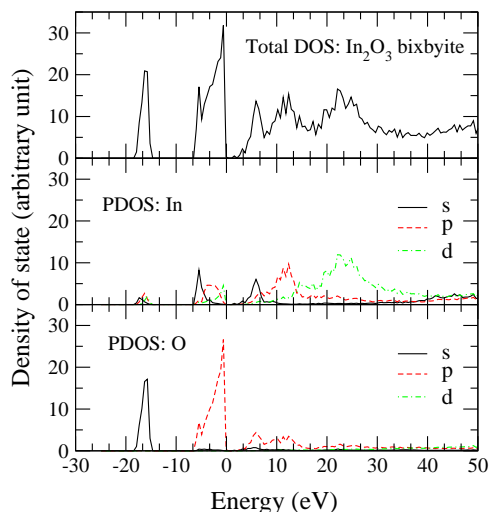

Fig. 4. The calculated DOS of bixbyite In_2O_3: (top panel) the total DOS, (middle and bottom panels) the site and angular momentum projected PDOS of In and O atoms.

Ref. [23]. Similar to the case of InN, the lowest narrow band centered at −17 eV is mainly O s and the higher VB located around −6 to 0 eV are mainly composed of O p with a small degree of In s, p and d. The lowest CB states located at 0–7 eV are mainly composed of O p hybridized with In s and p with a small degree of In d. The higher CB states (7–14 eV) are the mixing of O p and In p with a small degree of In d. The higher states (above 14 eV) are mainly In d.

For the alloy, we calculated the DOS of wurtzite $InN_{1-x}O_x$ alloy to determine the effects of O incorporation. Starting with a 72-atom wurtzite supercell of InN, we randomly replaced 14 (out of 36) nitrogen atoms with oxygen atoms without any site discrimination. This gives approximately 40% O content and the alloy will be referred to as $InN_{0.6}O_{0.4}$. In addition, we also calculated 20% oxygen content by replaced 7 nitrogen atoms with oxygen atoms. All atoms in the supercell were allowed to relax before calculating the DOS. Because a considerable fraction of N atoms were replaced by O atoms, the CB is partially occupied. To properly simulate XANES, only states above the Fermi level can contribute as a final state of the excitations. The DOS along with PDOS are shown in
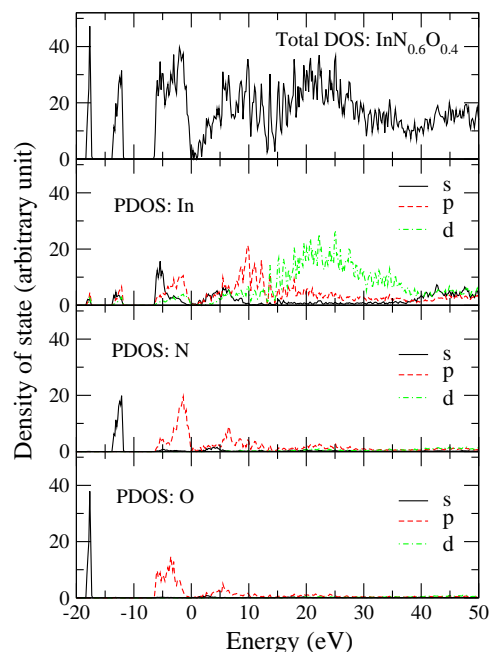

Fig. 5. The calculated DOS of $InN_{0.6}O_{0.4}$ alloy: (top panel) the total DOS, (bottom three panels) the site and angular momentum projected PDOS of In, N, and O atoms.

Fig. 5. It is clear that the DOS of the alloy is a mixture of InN DOS and In_2O_3 DOS. The two lowest narrow bands centered at −17 eV and −13 eV are O s and N s, respectively. The higher VB states located at around −6 to 0 eV are the mixing of N p, O p, In s and In p. Again, similar to the case of InN and In_2O_3, the lowest CB states located at 0–6 eV are mainly composed of O p and N p hybridized with In s and p with a small degree of In d. The higher CB states (6–14 eV) are the hybridization of N p (or O p) with In (mainly p and d) with a small degree of In s and N s (or O s). The higher states (above 14 eV) are mainly In d.

To compare the electronic states obtained from DFT method with In L_3-edge XANES spectra, we calculated In s + d PDOS and applied some broadening. The simulated spectra of InN and $InN_{0.6}O_{0.4}$ are shown in Fig. 6. It is not surprising that both spectra appear to be very similar. This is because the In atoms of both spectra are fourfolded. The main difference between the two simulated spectra is the reduction in the magnitude of the first peak located at around 10 eV (marked by an arrow in Fig. 6) above the Fermi energy. This reduction is expected because parts of the CB of $InN_{0.6}O_{0.4}$ alloy are occupied and cannot serve as final states of the absorption. Based on these PDOS, we expected that the L_3-edge
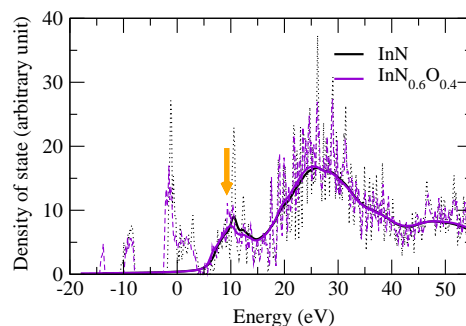

Fig. 6. The angular momentum ($s + d$) projected PDOS of In atoms of InN and $InN_{0.6}O_{0.4}$ alloy in the wurtzite structures. The dotted lines show the PDOS. The full thick lines show the smeared CB ($s + d$) states.

spectrum of wurtzite-$InN_{0.6}O_{0.4}$ remains similar to that of wurtzite InN except the reduction in the first peak. This reduction of the first peak is in a good agreement with the measured and simulated XANES spectra (based on the FEFF codes) that we previously presented [10] and will be briefly discussed again in the next section.

3.2. XANES spectra of InN, In_2O_3, and $InN_{1-x}O_x$ alloy

In our previous Letter [10], the In L_3-edge XANES were used to study the local structures of indium oxynitride thin films grown under different conditions. For completeness, the main content of the previous work will be briefly given here. Five samples of indium oxynitride alloys (N30/O0, N30/O5, N30/O10, N30/O20 and N0/O30, arranged from low to high O content) have been characterized. The names of the samples were given according to the gas timing ratio used to grow them. AES measurements show that the [O]:[N] ratio of the samples varied with the gas timing used (monotonically but not linearly). The measured XANES spectra and the FEFF simulations are shown in Fig. 7. The calculated XANES spectra of wurtzite-InN and bixbyite In_2O_3 are in full agreement with the measured spectra from N30/O0 and N0/O30 samples, respectively. This suggests that structurally In atoms in N30/O0 are mostly fourfold (as those in InN) and in N0/O30 are mostly sixfold (as those in In_2O_3). If we observe the change in the spectra while the oxygen content is increased (from the bottom curve to top curve), we can see that all five features marked by the arrows of the measured spectra are progressively evolved. However, the N30/O5 spectrum, which has 43% O content [10], is still almost identical to that of N30/O0 except the first shoulder, which is slightly reduced. This indicates that most of In atoms in this sample remained fourfold with some O atoms substituting on the N sites. The simulated spectrum of $InN_{0.6}O_{0.4}$ alloy in wurtzite structure was calculated using FEFF codes to test our assumption. The calculated spectrum is almost overlapped with that of (calculated) pure InN except the first shoulder is reduced; in full agreement with experimental observation and DFT PDOS discussed in previous section. As explained in the previous section, the reduction of the first shoulder occurs because parts of the CB are occupied. For samples with higher O contents (N30/O10 and N30/O20), the spectra show a mixed signature between those of wurtzite-InN and bixbyite In_2O_3. This means that there are both fourfold and sixfold In atoms in these samples. The excess O atoms above the substitutional solubility limit (assumed to be ∼40%) of InN can form a phase separated In_2O_3-like structure that lead to a formation of sixfold In atoms. Based on this model, the composition in the sample can be written as $(InN_{0.6}O_{0.4})_F(InO_{1.5})_{1-F}$, where the F values are 0.49 and 0.38 for N30/O10 and N30/O20, respectively [10]. The simulated spectra calculated using weight-averaged between $InN_{0.6}O_{0.4}$ and In_2O_3 are shown in Fig. 7. The simulated spectra based on this model are consistent with measured spectra (N30/O10 and N30/O20).

For In_2O_3, since there are two species of nonequivalent In atoms, the simulated spectrum shown in Fig. 7b (top curve) is obtained from the weight-averaged (In_{avg}) between the spectra of both In species (In1 and In2). As can be seen in Fig. 1a, the local structures are quite different (although both In1 and In2 are sixfolded), one might be curious how similar the spectra of In1 and In2 are. The spectra obtained from the two species of In atoms in In_2O_3 are quite similar, as shown in Fig. 8b. This further supports the fact that the shape of the spectra depends strongly on the coordination number (fourfold or sixfold) but only weakly on the detailed geometry distortion. For further test, the effects of the substitution of a neighboring N by O (or O by N) were studied. First, we replaced one N atom surrounding an In atom with an O atom in a wurtzite-InN supercell (72-atom). Second, all four N atoms surrounding the In atom were replaced by O atoms in a wurtzite-InN supercell. The simulated In L_3-edge XANES spectra of the In atoms that their neighbors were replaced are shown (labeled $1O_N$ and $4O_{4N}$ for the cases that one and four neighbors are replaced, respectively) in comparison with that of pure InN in Fig. 8a. It is clear that even all four N neighbors are replaced, the features of the spectrum still remain the same as those of pure InN. We have also tested the bixbyite (sixfold In) structure. We replaced one oxygen atom by a nitrogen atom in the In_2O_3 bixbyite structures. The simulated XANES spectrum of the In atom that its neighboring O was replaced by N, is shown (labeled $1N_O$) in comparison with that of pure In_2O_3 in Fig. 8b. It is clear that the XANES features are not very sensitive to anion substitutions but very sensitive to the coordination number of In (fourfold or sixfold).
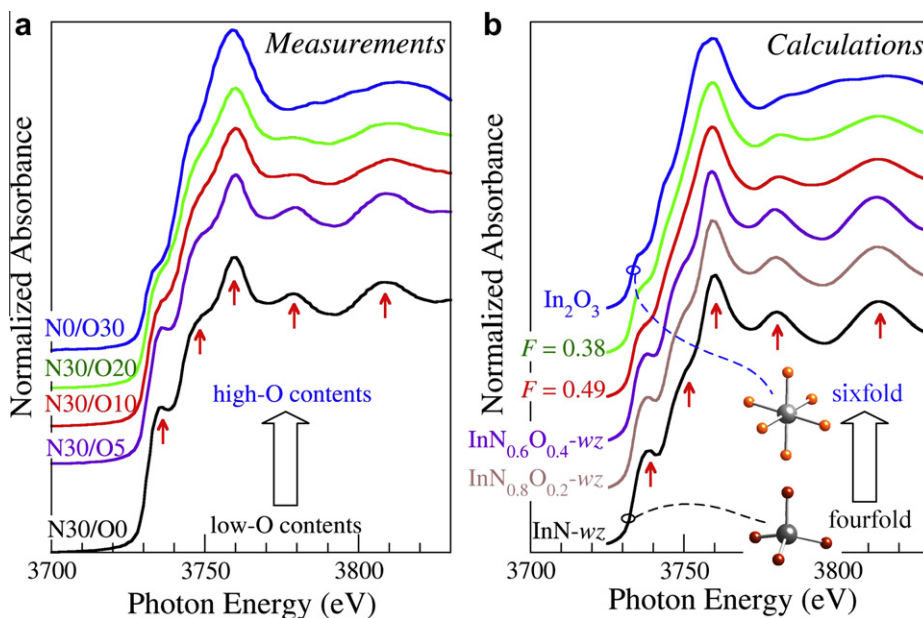

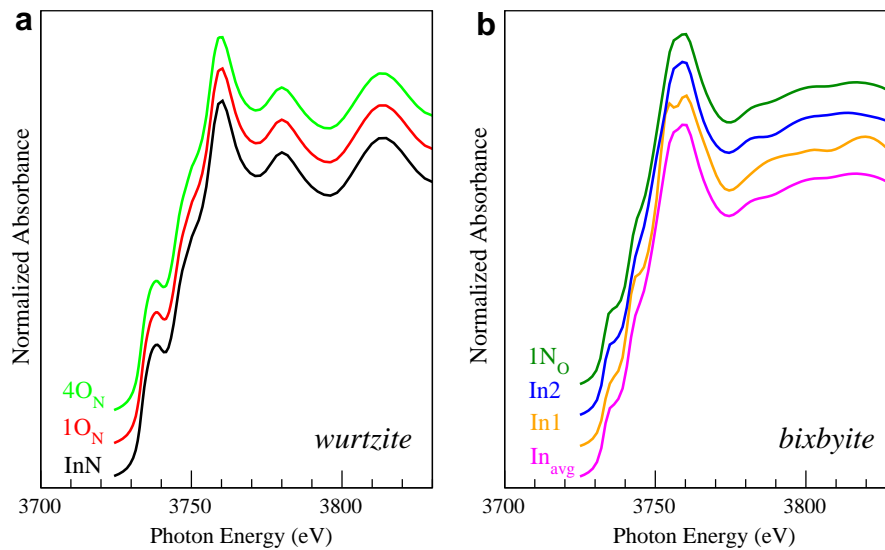**Fig. 7.** The measured and simulated In L_3-edge XANES spectra of all five samples.

Fig. 8. (a) The simulated In L_3-edge XANES spectra of In atoms in pure wurtzite InN (bottom), in wurtzite InN with one N replaced by O (middled), and in wurtzite InN with four N replaced by O (top). (b) The spectra In atoms in pure bixbyite In_2O_3 (bottom three curves) and in bixbyite In_2O_3 with one O replaced by N (top).

4. Conclusion

Synchrotron X-ray absorption near edge structures of In L_3-edge were used to study the local geometry of indium atoms in indium oxynitride thin films with varied O contents. Calculations showed that the spectra features are sensitive to the coordination number of the In atom (fourfold for wurtzite structure or sixfold for bixbyite structure) but not very sensitive to the species (O or N) of the first neighbors such that interchanging N with O leads to almost unnoticeable changes in the XANES spectra. The solubility limit of oxygen in wurtzite InN is estimated to be ~40% before the crystal structure drastically changed. The band structures and density of states of InN, In_2O_3, and their alloys are shown and discussed.

Acknowledgements

References

[1] S.-H. Wei, X. Nie, I.G. Batyrev, S.B. Zhang, Phys. Rev. B 67 (2003) 165209.
[2] J. Wu, W. Walukiewicz, S.X. Li, R. Armitage, J.C. Ho, E.R. Weber, E.E. Haller, H. Lu, W.J. Schaff, A. Barcz, R. Jakiela, Appl. Phys. Lett. 84 (2004) 2805.
[3] V.Y. Davydov, A.A. Klochikhin, V.V. Emtsev, S.V. Ivanov, V.V. Vekshin, F. Bechstedt, J. Furthmuller, H. Harima, A.V. Mudryi, A. Hashimoto, A. Yamamoto, J. Aderhold, J. Graul, E.E. Haller, Phys. Status Solidi B 230 (2002) r4.
[4] J. Wu, W. Walukiewicz, K.M. Yu, J.W. Ager Iii, E.E. Haller, H. Lu, W.J. Schaff, Y. Saito, Y. Nanishi, Appl. Phys. Lett. 80 (2002) 3967.
[5] A. Klein, Appl. Phys. Lett. 77 (2000) 2009.
[6] A. Walsh, J.L.F. Da Silva, S.-H. Wei, C. Körber, A. Klein, L.F.J. Piper, A. DeMasi, K.E. Smith, G. Panaccione, P. Torelli, D.J. Payne, A. Bourlange, R.G. Egdell, Phys. Rev. Lett. 100 (2008) 167402.
[7] K.R. Reyes-Gil, E.A. Reyes-Garcia, D. Raftery, J. Phys. Chem. C 111 (2007) 14579.
[8] Motlan, E.M. Goldys, T.L. Tansley, J. Crystal Growth 241 (2002) 165.
[9] M. Yoshimoto, H. Yamamoto, W. Huang, H. Harima, J. Saraie, A. Chayahara, Y. Horino, Appl. Phys. Lett. 83 (2003) 3480.
[10] J. T-Thienprasert, J. Nukeaw, A. Sungthong, S. Porntheeraphat, S. Singkarat, D. Onkaw, S. Rujirawat, S. Limpijumnong, Appl. Phys. Lett. 93 (2008) 051903.
[11] N. Kietipaisalsophon, W. Bunjongpru, J. Nukeaw, Int. J. Mod. Phys. B 16 (2002) 4418.
[12] A. Sungthong, S. Porntheeraphat, A. Poyai, J. Nukeaw, Appl. Surf. Sci. 254 (2008) 7950.
[13] D. Vanderbilt, Phys. Rev. B 41 (1990) 7892.
[14] G. Kresse, J. Furthmüller, Comput. Mater. Sci. 6 (1996) 15.
[15] G. Kresse, J. Hafner, J. Phys.: Condens. Mat. 6 (1994) 8245.
[16] H.J. Monkhorst, J.D. Pack, Phys. Rev. B 13 (1976) 5188.
[17] A.L. Ankudinov, C.E. Bouldin, J.J. Rehr, J. Sims, H. Hung, Phys. Rev. B 65 (2002) 104107.
[18] A.L. Ankudinov, B. Ravel, J.J. Rehr, S.D. Conradson, Phys. Rev. B 58 (1998) 7565.
[19] L. Hedin, S. Lundqvist, Solid State Phys. 23 (1969) 1.
[20] S. Limpijumnong, S. Rujirawat, A. Boonchun, M.F. Smith, B. Cherdhirunkorn, Appl. Phys. Lett. 90 (2007) 103113.
[21] Properties of Group-III Nitrides, in: J.H. Edgar (Ed.), EMIS Datareviews Series, IEE, London, 1994.
[22] ICSD, Inorganic Crystal Structure Database, Fachinformationszentrum Karlsruhe, Germany, 2002.
[23] P. Erhart, A. Klein, R.G. Egdell, K. Albe, Phys. Rev. B 75 (2007) 153205.

Contents lists available at ScienceDirect

Computational Materials Science

journal homepage: www.elsevier.com/locate/commatsci

Vibrational signatures of O_{Te} and O_{Te}–V_{Cd} in CdTe: A first-principles study

J. T-Thienprasert [a,b], S. Limpijumnong [c,*], A. Janotti [d], C.G. Van de Walle [d], L. Zhang [e], M.-H. Du [e], D.J. Singh [e]

[a] Department of Physics, Kasetsart University, Bangkok 10900, Thailand
[b] Thailand Center of Excellence in Physics (ThEP Center), Commission on Higher Education, Bangkok 10400, Thailand
[c] School of Physics, Suranaree University of Technology and Synchrotron Light Research Institute, Nakhon Ratchasima 30000, Thailand
[d] Materials Department, University of California, Santa Barbara, CA 93106, USA
[e] Oak Ridge National Laboratory, Oak Ridge, TN 37831, USA

ARTICLE INFO

ABSTRACT

Chen et al. [Phys. Rev. Lett. 96 (2006) 035508] experimentally observed vibrational signatures related to defects in oxygen-doped CdTe using ultrahigh resolution Fourier transform infrared (FTIR) spectroscopy. They observed an absorption peak at $350 \, cm^{-1}$. In addition, for samples grown under certain conditions, they observed two higher frequency peaks (1097 and $1108 \, cm^{-1}$) at low temperature that merged into one at room-temperature. They attributed the low-frequency peak ($350 \, cm^{-1}$) to the vibration of O_{Te} and the two higher frequency peaks to the vibrational modes of a O_{Te}–V_{Cd} complex. Subsequently, they reported similar modes around $1100 \, cm^{-1}$ in O-doped CdSe [Phys. Rev. Lett. 101 (2008) 195502] which were attributed to an O_{Se}–V_{Cd} complex. We employed first-principles DFT calculations to calculate the vibrational modes of O_{Te} and O_{Te}–V_{Cd} complex in CdTe. Our calculations show that the $350 \, cm^{-1}$ mode is consistent with O_{Te}. However, the frequencies of the modes around $1100 \, cm^{-1}$ are more than twice the expected frequencies for O_{Te}–V_{Cd} complexes in CdTe (or O_{Se}–V_{Cd} in CdSe), indicating that the O_{Te}–V_{Cd} complex cannot be the cause of the observed $1100 \, cm^{-1}$ modes. A search for a new defect model is in order.

© 2010 Elsevier B.V. All rights reserved.

1. Introduction

CdTe is recognized as a promising semiconductor because it can be doped both n-type and p-type. The role of defects in CdTe has been theoretically studied by Wei and Zhang [1]. CdTe and its alloys have been used for applications such as room-temperature X-ray and γ-ray detectors [2,3]. The Bridgman technique [4,5] can be used to grow high quality CdTe bulk crystal samples.

Recently, local vibrational modes (LVM) related to oxygen impurities in CdTe have been experimentally studied using Fourier transform infrared (FTIR) spectroscopy [4,6]. Depending on the growth and doping conditions, low temperature FTIR measurements reveal three LVMs related to oxygen: one low-frequency mode at $350 \, cm^{-1}$ and two high-frequency modes at $v_1 = 1097$ and $v_2 = 1108 \, cm^{-1}$. As the measuring temperature is increased, the two high-frequency modes (v_1 and v_2) merge into one at room-temperature. Chen et al. [4,6] assigned the low-frequency mode to an oxygen substituting on the Te site (O_{Te}), and the two high-frequency modes to a complex formed by an oxygen substituting on a Te site and a neighboring Cd-vacancy (O_{Te}–V_{Cd}) [4]. Later, they also found similar high-frequency modes around

$1100 \, cm^{-1}$ in O-doped CdSe [7] that they attributed to an O_{Se}–V_{Cd} complex. Chen et al. believe that when forming a complex with V_{Cd}, the frequency of O_{Te} can increase by almost a factor of three. They attributed the increase in the frequency to an increase in the bond strength between the O atom and its neighbors as the number of Cd neighbors is reduced from four (for O_{Te}) to three (for O_{Te}–V_{Cd}).

To understand these vibrational modes, we have investigated O-related centers in CdTe using density functional calculations. The LVM frequencies of O_{Te} and O_{Te}–V_{Cd} defects were calculated by using force–response matrix (dynamical matrix) calculations. The harmonic approximation is used. We will show that the calculated LVM of O_{Te} is consistent with the experimental value. However, the calculated LVM frequencies of O_{Te}–V_{Cd} are much lower than the v_1 and v_2 modes observed by Chen et al. [4]. Although the O–Cd bonds are slightly stronger, the frequency increases by only 38%, not by a factor of three. Therefore, it is clear that the O_{Te}–V_{Cd} complex is not the correct model to explain the observed LVMs. Preliminary results of our work have been published as a comment [5]. Here, we present the computational method and details of the LVMs. The two high frequencies observed by Chen et al. [4] should be attributed to other defects related to the introduction of O in CdTe, not to O_{Te}–V_{Cd}. We note that the high value of the frequency makes hydrogen (which could be related to the introduction of O during growth) a prime candidate.

* Corresponding author.
  E-mail address: sukit@sut.ac.th (S. Limpijumnong).

2. Calculations of local vibrational mode

Our work is based on density functional theory within the local density approximations (LDA). For the electron–ion interactions, we used projector augmented wave potentials [8], as implemented in the VASP code [9,10], with an energy cutoff of 500 eV for the plane-wave basis set. The calculated lattice constant of bulk CdTe is 6.421 Å, in good agreement with the experimental value of 6.477 Å [11]. To calculate the equilibrium lattice constant, calculations of bulk CdTe at various lattice constants were performed, and fitting to an equation of state [12] identifies the lowest energy structure.

For defects, a supercell approach is used [13]. In principle, to simulate an isolated defect, the larger supercell size, the better. Previously we have shown that a 32-atom is sufficient to suppress the interaction between the defect and its images [14]. Here, we used a 64-atom supercell, which is a $2 \times 2 \times 2$ repetition of the CdTe conventional 8-atom unit cell. All atoms in the supercell were allowed to relax until the Hellmann–Feynman forces [15] become less than 10^{-3} eV/Å. The Monkhorst–Pack scheme [16] with a sampling mesh of $2 \times 2 \times 2$ special k-points is used for k-space integrations.

The LVMs of O defects were calculated using the so-called frozen phonon approach [17]. First, for each defect configuration, the structure is allowed to fully relax. Then we slightly shifted each and every atom in the supercell along all three axes, one at a time, and the dynamical matrix can be constructed from the forces on all atoms in response to these displacements. Within the harmonic approximation, the total energy of a supercell with small displacements of atoms from their equilibrium positions can be written as

$$E = E_0 + \frac{1}{2} \sum_{i,j,\alpha,\beta} \Phi_{\alpha\beta}(i,j)\, d_\alpha(i)\, d_\beta(j), \tag{1}$$

where $d_\alpha(i)$ is the displacement of atom i from its equilibrium position in the direction α and $\Phi_{\alpha\beta}(i,j)$ is the real-space force constant matrix. A small displacement $d_\beta(j)$ of atom j in direction β induces a force on atom i in direction α described by

$$F_\alpha(i) = -\Phi_{\alpha\beta}(i,j)\, d_\beta(j). \tag{2}$$

Based on Eq. (2), we can construct the complete real-space force constant matrix $\Phi_{\alpha\beta}(i,j)$. This is done by creating a small displacement[1] d_0 (we use $d_\beta(j) = d_0 = 0.01 \times a$ where a is the lattice constant) of each atom j in the supercell in three orthogonal directions, $\beta = 1, 2, 3$, one atom and one direction at a time. For each calculation, the (Hellmann–Feynman) forces on all atoms in all three directions $F_\alpha(i)$ are recorded and the components of the force constant matrix can be obtained by using Eq. (2). To reduce from the impact of anharmonic effects, each component of the force constant matrix is obtained from an average of two calculations: one with $+d_0$ displacement and another with $-d_0$ displacement. The dynamical matrix can be easily calculated from the force matrix according to the equation,

$$D_{\alpha\beta}(i,j) = (M_i M_j)^{-1/2} \Phi_{\alpha\beta}(i,j), \tag{3}$$

where M_i is the mass of atom i. The diagonalization of the dynamical matrix yields the eigenvalues $e_k = \omega_k^2$, and eigenvectors $|u_k\rangle$. The eigenvalues are the frequencies of the vibrational modes. The eigenvector of each mode describes the displacements of each atom in the system.

3. Results and discussion

Fig. 1a shows the crystal structure of CdTe. The O_{Te} center is calculated by replacing one Te atom in the 64-atom CdTe supercell with an O atom (O_{Te}) and allowing full relaxation. We found that the O atom forms bonds with its four Cd neighbors with an equal distance (Fig. 1b). The bond distance of O–Cd is shorter than that of Cd–Te bond in bulk CdTe by 19%.

The complex between O_{Te} and a Cd-vacancy (O_{Te}–V_{Cd}) is created by removing a Cd neighbor of O_{Te}. Under n-type and semi-insulating conditions, we found that the O_{Te}–V_{Cd} complex is stable in the 2^- charge state. Because CdTe samples used in experiments are generally semi-insulating [4], we reported only the 2^- charge state in this paper (Note that other two possible charge states, i.e. neutral and 1^-, have very similar bond structures and vibration frequencies.). Since one Cd–O bond is missing, the O atom moves closer to the three remaining Cd neighbors. As a result the O atom is moved in the direction away from the center of the vacancy toward the center of the three remaining Cd neighbors, leading to shorter bond distances between the O atom and the three remaining Cd neighbors. The remaining three Cd–O bonds are equal in distance and 32% shorter than the Cd–Te distance in bulk CdTe (Fig. 1c). Note that the O atom is equidistant from the three Cd neighbors and only 0.26 Å away from the plane formed by those Cd atoms.

The LVM frequencies of O_{Te} and the O_{Te}–V_{Cd} complex were calculated by using the full dynamical matrix calculations for a 64-atom supercell as described in the previous section. To identify the modes localized on the O impurity, we calculated the sum-square of the three eigenvector components associated with the O atom ($\sum_{atom=O} u^2$ or, in short, $\sum u_0^2$). Note that the sum-square of all components is normalized to 1. The $\sum u_0^2$ for all modes are plotted as histograms in Fig. 2. For O_{Te}, we can clearly see that the triply degenerate mode at 338 cm^{-1} is localized on the O atom. The mode is triply degenerate because the O atom has fourfold symmetry. Under a simple harmonic approximation, the vibrations of the O atom in all three axes are therefore equivalent. An illustration of the set of eigenvectors describing these degenerate modes is shown in Fig. 3a. The value of $\sum u_0^2$ for this mode is 0.95, indicating a very strong localization of the mode. The calculated LVM frequency of 338 cm^{-1} is in good agreement with the observed value of 350 cm^{-1} [4]. For the O_{Te}–V_{Cd} complex (Fig. 2b), we find a doubly degenerate mode (at 467 cm^{-1}) and a singlet mode (at 197 cm^{-1}) that are localized on the O atom. The values of $\sum u_0^2$ are 0.94 and 0.34 for the doublet and singlet states, respectively. These modes are derived from the triply degenerate mode of O_{Te}. The introduction of V_{Cd} leads to a symmetry breaking that separates the modes into a doublet and a singlet. The doublet (467 cm^{-1}) is associated with the in-plane vibration; the O motion is illustrated in Fig. 3b. The singlet (197 cm^{-1}) is associated with the out-of-plane vibration of the O atom accompanied by the outward breathing of the surrounding Cd neighbors as illustrated in Fig. 3c. The increase in the frequency of the doublet (in comparison to that of O_{Te}) by 38% can be attributed to the stronger Cd–O bond in the complex. Similarly, the decrease in the frequency of the singlet (in comparison to that of O_{Te}) by 42% can be attributed to the missing Cd–O bond (in the direction of vibration) of the complex.

The calculated frequencies of 197 cm^{-1} for the out-of-plane vibration and 467 cm^{-1} for the in-plane vibration are completely inconsistent with the two high LVM frequencies of 1097 and 1108 cm^{-1} assigned by Chen et al. [4] for out-of-plane and in-plane vibration of the O_{Te}–V_{Cd} complex. While the presence of a Cd-va-

---

[1] The displacement should be large enough to allow an accurate determination of the energy increase (or response forces) in the calculations. However, it should be small enough to stay within the range of realistic vibrational amplitudes where the harmonic approximation is expected to be valid.
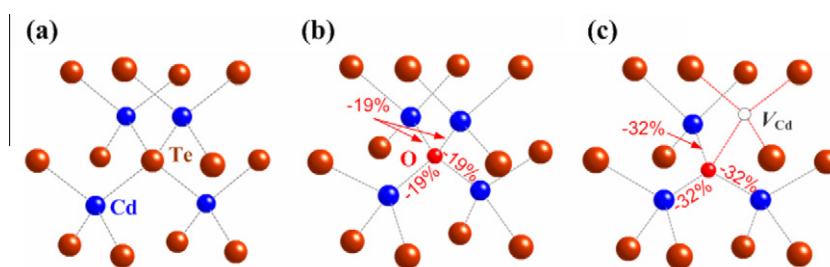
Fig. 1. The local structures of (a) bulk CdTe, (b) O_{Te}, and (c) O_{Te}–V_{Cd} complex in CdTe. The bond distances are given as percentage differences from the Cd–Te bond distance (calculated value = 2.781 Å) in bulk CdTe.
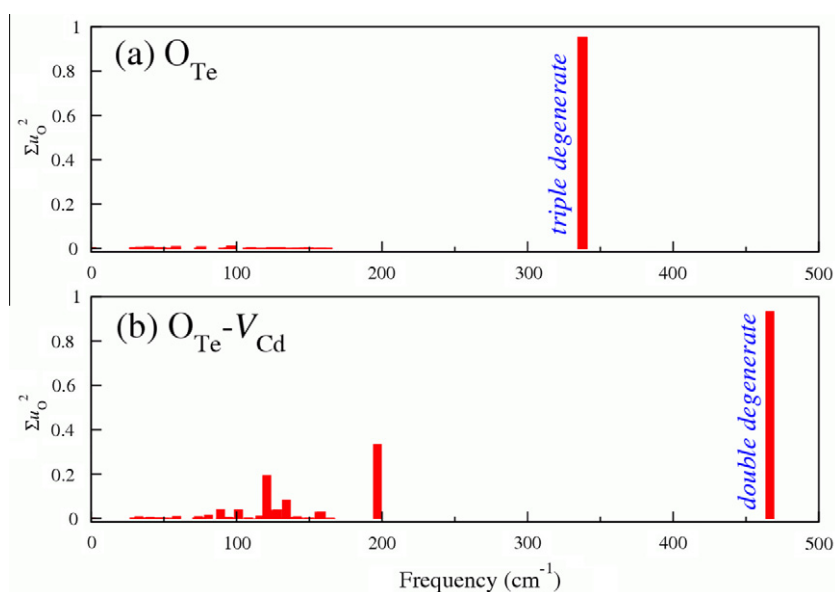

Fig. 2. The sum-square of the three eigenvector components associated with the O atom $\left(\sum_{atom=O} u^2\right)$ for all vibrational modes for (a) O_{Te} and (b) the O_{Te}–V_{Cd} complex in a 64-atom CdTe supercell.

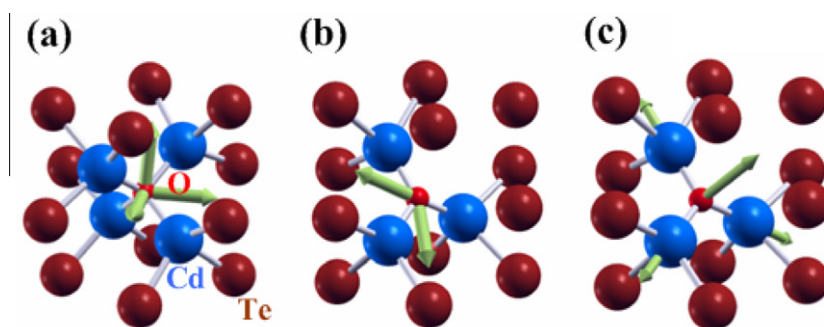**Fig. 3.** Schematic illustrations of the vibration vectors describing the local vibrational modes associated with O in O_{Te} and in the O_{Te}–V_{Cd} complex in CdTe. (a) The triply degenerate mode of O_{Te}. (b) The doubly degenerate mode and (c) the singlet mode of the O_{Te}–V_{Cd} complex in CdTe. In (a) and (b) each arrow represents the vibration vector of the O atom in each of the degenerate mode. Components on other atoms are small and not shown. In (c), the four arrows show the vibration vectors of the O atom and its Cd neighbors.

cancy near the substitutional oxygen indeed leads to an increase in the vibrational frequency of the in-plane vibrational mode, the magnitude of this increase is far smaller than Chen et al. assumed. The frequency is increased from 338 cm^{-1} to 467 cm^{-1}, a mere 38%, very different from the 228% assumed in Chen et al.'s attribution. Moreover, the out-of-plane frequency does not increase at all; instead, it is lowered to 197 cm^{-1}. Based on our calculations, we can therefore safely conclude that the high-frequency modes

(1097 and 1108 cm^{-1}) observed in the experiment of Chen et al. [4] are *not* associated with a O_{Te}–V_{Cd} complex.

More recently, similar LVM frequencies (1094, 1107, and 1126 cm^{-1}) were observed in oxygen-doped CdSe by the same experimental group [7]. They similarly assigned these LVM frequencies to an O_{Se}–V_{Cd} complex and explained that an additional mode (they observed three high-frequency modes instead of the two modes in the case of CdTe) is the result of the lower crystal

symmetry of CdSe. For completeness, we also calculated the vibrational frequencies of O_{Se} and the O_{Se}–V_{Cd} complex in CdSe using the same approach as for the O-related centers in CdTe. We obtained the LVM frequency of O_{Se} at 370 cm^{-1}, comparable to (and slightly higher than) that of O_{Te} in CdTe. For the O_{Se}–V_{Cd} complex, we obtained LVM frequencies of 512, 507, and 223 cm^{-1}, again comparable to (and consistently higher than) the corresponding calculated frequencies for the O_{Te}–V_{Cd} complex in CdTe. Because the calculated frequencies are inconsistent with the observed values of 1094, 1107, and 1126 cm^{-1}, we can again safely conclude that the observed modes are not associated with O_{Se}–V_{Cd} complex in CdSe.

We acknowledge that first-principles calculations of vibrational frequencies have error bars, but in general the calculated frequencies agree very well with experimental values [18–23]. Deviations from experimental values by more than 15% (or about 150 cm^{-1}) are very rare. The huge qualitative difference between the frequencies for the Cd-vacancy related complexes and the modes observed by Chen et al. [4,7] therefore clearly indicates that the attribution of these modes to $O_{Te\ (or\ Se)}$–V_{Cd} complexes cannot be correct.

4. Conclusion

Based on first-principles density functional calculations, the vibrational frequencies associated with O_{Te} and O_{Te}–V_{Cd} complexes in CdTe and O_{Se} and O_{Se}–V_{Cd} complexes CdSe were calculated and used to interpret recent experimental measurements by Chen et al. [4,6]. In the experiment, a low-frequency local vibrational mode (350 cm^{-1}) and two high-frequency modes (1097 and 1108 cm^{-1}) are observed in oxygen-doped CdTe samples. The low-frequency mode has been assigned to O_{Te} and the two high-frequency modes have been assigned to a O_{Te}–V_{Cd} complex. In a more recent experiment on CdSe by the same group, similar modes are observed and assigned to O_{Se} and O_{Se}–V_{Cd}. Our calculated frequency of O_{Te} in CdTe is 338 cm^{-1} which is in a reasonable agreement with the measured value of 350 cm^{-1}. However, the calculated frequencies of the O_{Te}–V_{Cd} complex are 197 and 467 cm^{-1}, far lower than the observed values (1097 and 1108 cm^{-1}) and strongly indicating that the assignment of the high-frequency modes to the O_{Te}–V_{Cd} complex is incorrect. The 1097 and 1108 cm^{-1} modes must come from other defects, possibly hydrogen related. Similar conclusions apply to the case of oxygen in CdSe.

References

[1] S.-H. Wei, S.B. Zhang, Phys. Rev. B 66 (2002) 155211.
[2] T.E. Schlesinger, J.E. Toney, H. Yoon, E.Y. Lee, B.A. Brunett, L. Franks, R.B. James, Mater. Sci. Eng. 32 (2001) 103.
[3] C. Szeles, Phys. Status Solidi B 241 (2004) 783.
[4] G. Chen, I. Miotkowski, S. Rodriguez, A.K. Ramdas, Phys. Rev. Lett. 96 (2006) 035508.
[5] L. Zhang, J. T-Thienprasert, M.-H. Du, D.J. Singh, S. Limpijumnong, Phys. Rev. Lett. 102 (2009) 209601.
[6] G. Chen, I. Miotkowski, S. Rodriguez, A.K. Ramdas, Phys. Rev. B: Condens. Matter Mater. Phys. 75 (2007) 125204.
[7] G. Chen, J.S. Bhosale, I. Miotkowski, A.K. Ramdas, Phys. Rev. Lett. 101 (2008) 195502.
[8] G. Kresse, D. Joubert, Phys. Rev. B 59 (1999) 1758.
[9] G. Kresse, J. Furthmüller, Comput. Mater. Sci. 6 (1996) 15.
[10] G. Kresse, J. Hafner, J. Phys.: Condens. Matter 6 (1994) 8245.
[11] D.R. Lide (Ed.), CRC Handbook of Chemistry and Physics, 88th ed., CRC Press/Taylor and Francis, Boca Raton, FL, 2008.
[12] J.H. Rose, J.R. Smith, F. Guinea, J. Ferrante, Phys. Rev. B 29 (1984) 2963.
[13] C.G. Van de Walle, J. Neugebauer, J. Appl. Phys. 95 (2004) 3851.
[14] S. Limpijumnong, J.E. Northrup, C.G. Van de Walle, Phys. Rev. Lett. 87 (2001) 205505.
[15] R.P. Feynman, Phys. Rev. 56 (1939) 340.
[16] H.J. Monkhorst, J.D. Pack, Phys. Rev. B 13 (1976) 5188.
[17] A.M. Teweldeberhan, S. Fahy, Phys. Rev. B: Condens. Matter Mater. Phys. 72 (2005) 195203.
[18] M.-H. Du, S. Limpijumnong, S.B. Zhang, Phys. Rev. B 72 (2005) 073202.
[19] X. Li, B. Keyes, S. Asher, S.B. Zhang, S.-H. Wei, T.J. Coutts, S. Limpijumnong, C.G. Van de Walle, Appl. Phys. Lett. 86 (2005) 122107.
[20] X.-B. Li, S. Limpijumnong, W.Q. Tian, H.-B. Sun, S.B. Zhang, Phys. Rev. B: Condens. Matter Mater. Phys. 78 (2008) 113203.
[21] S. Limpijumnong, X. Li, S.-H. Wei, S.B. Zhang, Appl. Phys. Lett. 86 (2005) 211910.
[22] S. Limpijumnong, J.E. Northrup, C.G. Van de Walle, Phys. Rev. B 68 (2003) 075206.
[23] S. Limpijumnong, P. Reunchan, A. Janotti, C.G. Van de Walle, Phys. Rev. B: Condens. Matter Mater. Phys. 77 (2008) 195209.

The effects of unit cell size on the bandgap range in the direct enumeration study of $Al_xGa_yIn_{1-x-y}P$ alloys

Sirichok Jungthawan [a,b,*], Kwiseon Kim [c], Sukit Limpijumnong [a,b]

[a] School of Physics, Institute of Science, Suranaree University of Technology and Synchrotron Light Research Institute, Nakhon Ratchasima 30000, Thailand
[b] Thailand Center of Excellence in Physics (ThEP Center), Commission on Higher Education, Bangkok 10400, Thailand
[c] National Renewable Energy Laboratory, Golden, Colorado 80401, USA

ARTICLE INFO

ABSTRACT

Direct enumeration method is an efficient way for scanning alloy properties by computing all possible configurations. This method thoroughly covers all possible configurations without bias and provides an informative trend of alloy properties on ordering patterns. In an actual study, the number of possible configurations increases rapidly with the size of the unit cell and usually a reasonable size that give a sufficiently large number of configurations are chosen. In this work, the convergence of the bandgap range with respect to the unit cell size of AlGaInP alloy is studied up to 8 cation atoms per unit cell. It is found that the bandgap range already converges to within 0.1 eV when the unit cell size is 4 cation atoms. Interestingly, we also found that the lowest bandgap value of GaInP alloy is achieved already in a small cell (2 cations in the unit cell). The cause for this special small bandgap case is discussed.

© 2010 Elsevier B.V. All rights reserved.

1. Introduction

Alloying provides a flexible way to engineer electronics and optical properties of semiconductors to suit the need of new generation device applications [1–3]. The properties of semiconductor alloys, especially those of III–V alloys, have been extensively studied in the last decade [1–4]. Several schemes were proposed to explain the relationship between the properties and the alloy composition. The simplest and most known scheme (the Vegard's rule) assumes a linear dependence between the interested property and the alloy composition [5,6]. In reality, most properties are not linearly dependent with the alloy composition. As a result, non-linear terms have been proposed to quantify the deviation from the Vegard's trend. The most known improved scheme added a bowing parameter [7]. However, neither the Vegard's rule nor its variants takes into account the ordering of the constituent atoms in the alloy. It is important to note that, for a given alloy composition, there are virtually infinite possible arrangements of the atoms in the alloy. From the theoretical point of view, the direct enumeration method (DEM) has been used to study alloy systems [8–11]. The important elements of the method are the algorithm to generate alloy configurations [10,12,13] and the practical method to calculate their properties [8,10,11,14–17]. The algorithm to generate alloy configurations for binary alloy with face-centered cubic (FCC) and body-centered cubic (BCC) lattice have been proposed by Ferreira et al. [10]. Later, an efficient algorithm for generating alloy configurations has been introduced by Hart and Forcade [18] where the run time scales linearly with the number of distinct configurations. Recently, an algorithm for generating alloy configurations of a non-primitive lattice and application to hexagonal close packed alloys have been developed [19]. The DEM has been used to study the bandgap properties calculated by empirical pseudopotential method (EPM) [14–17,20–23] of several classes of semiconductor alloys; including the ternary [9–11] and quaternary [24] alloys. An advantage of DEM is that it relates the interested property to the alloy configuration (atomic ordering) in additional to the composition. From EPM calculation, we have previously shown that the bandgap of AlGaInP alloy depends strongly on the atomic ordering in addition to the alloy composition [24]. In that work, we have also shown that most of the alloy configurations have the bandgaps that are smaller than the values predicted by the Vegard's rule. The ordering causes a reduction in the bandgap; pushing it below the Vegard's trend [24–26]. The lowering of the bandgap due to atomic arrangements emphasizes the role of the alloy configurations (in addition to the alloy composition) in bandgap engineering. In this work and our previous work [24], we focused our attentions in studying a complete set of theoretical

* Corresponding author at: School of Physics, Institute of Science, Suranaree University of Technology and Synchrotron Light Research Institute, Nakhon Ratchasima 30000, Thailand. Tel.: +66 44224319; fax: +66 44224651.
E-mail address: sirichok@sut.ac.th (S. Jungthawan).

possible arrangements within a given cell size. These complete results allow us to investigate how the band properties relate to the atomic arrangements. However, we should keep in mind that many of the configurations studied might have a very high energy and difficult to fabricate.

Because there are many distinct alloy configurations for a given alloy composition, DEM gives the possible range of properties (for e.g., the bandgap and the electron effective mass) at a given alloy composition, as well as the relationship between the ordering and a given property. While a larger cell size gives more possible configurations (allowing a more complete study) and finer composition steps, the computational demand is increased rapidly. Therefore, it is important to investigate the size of unit cell that sufficiently gives the converged results. In this work, we focus on the quaternary alloys $Al_xGa_yIn_{1-x-y}P$ (also called pseudoternary alloys that contain three mixed-cations in the FCC sublattice).

2. Calculation

The alloy configurations of AlGaInP are generated by applying DEM [9,11,24] to a zincblende-based alloy system. The possible number of alloy configurations for a unit cell containing N cation atoms is given by the *multichoose* formula [27], $\left(\begin{array}{c} n+N-1 \\ N \end{array} \right) = (n-1,N)!$, with n being the number of elements. For AlGaInP alloy, $n = 3$. A subroutine in the Alloy Theoretic Automated Toolkit (ATAT) package [28,29] was employed to systematically generate the configurations. The detail of alloy configurations generated by ATAT is described elsewhere [24]. Note that, some of the generated configurations are equivalent by symmetries and the redundant configurations were removed to reduce computation demand. Using the ATAT codes, the cell size of up to 8 cation atoms per unit cell ($N_{max} = 8$) provides a total of 9808 distinct configurations. They are composed of 1887 pseudobinary alloy configurations from the three parent binary compounds (3×629 AlGaP, GaInP and AlInP) and 7918 pseudoternary alloy configurations [see Ref. [24] (Table 1) for detail].

Because the composition of the $Al_xGa_yIn_{1-x-y}P$ alloys is defined by two variables (x and y), the composition space can be presented in a two-dimensional space. We have previously shown that the two-dimension composition space of this ternary alloy system is well described by using the transformed coordinates, $u = x + y/2$ and $v = \sqrt{3}y/2$ [24]. This leads to a regular triangle, as shown in Fig. 1. The parent compounds are located at the vertices and the circles represent the alloy compositions that can be obtained by each unit cell size.

To reduce the computation demand, alloy properties of all generated configurations are calculated by using EPM [14,15]. The structural relaxation was done by the valence force field method (VFF) [30–33]. In EPM, the electronic structures are obtained by solving the simplified Schrödinger equation
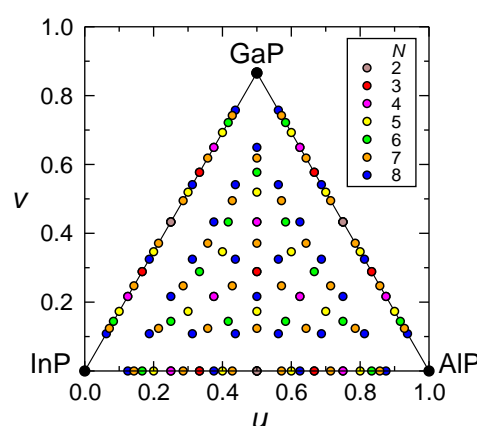

Fig. 1. The composition space of the pseudoternary alloy system. The colored circles show the possible compositions given by each unit cell size (i.e. N = 2, 3, 4, 5, 6, 7, and 8). Circles on the three edges of the triangle correspond to the pseudobinary alloys.

$$\left\{ -\frac{1}{2}\nabla^2 + \sum_{\alpha,n} V_\alpha(\mathbf{r} - \mathbf{R}_{\alpha,n}) \right\} \psi_i(\mathbf{r}) = \varepsilon_i \psi_i(\mathbf{r}) \quad (1)$$

where the effective pseudopotential is summed over all individual atoms n (α denotes atomic type). V_α is the screened potential for atomic type α and $\mathbf{R}_{\alpha,n}$ is the atomic position of atom n (type α) obtained after VFF relaxations. One advantage of EPM (over first-principles density functional calculations) is that it provides the bandgaps that do not need corrections. This is because the parameters are already fitted to the experimental bandgaps. The cutoff energy of the generated pseudopotentials is 68 eV. The details of the fitting parameters for the atomic potentials of AlP, GaP, and InP compounds can be found in Ref. [16]. Details of EPM method [14–16] and electronic structure computation are described elsewhere [24].

For each set of the configurations in a unit cell size, the maximum and the minimum bandgaps are determined. The possible range of bandgaps is the difference between the maximum and the minimum values at a given composition. Because the ordering of cation atoms can cause a bandgap reduction [24], the larger cell size, which facilitates more degree of ordering, is likely to provide a smaller minimum bandgap than the smaller cell size. However, it is expected that the minimum value of bandgap would converge at a sufficiently large cell. In this work, the largest cell size used is the unit cell with 8 cations. The bandgap minima are calculated for cell size of, N_{max} = 4, 5, 6, 7, and 8. The upper bound of bandgap is set by the Vegard's rule which represent the disordered alloys [24]. According to Vegard's rule, the (upper bound) bandgap of $Al_xGa_yIn_{1-x-y}P$ is

$$E_{gap}(x,y) = xE_{gap}(AlP) + yE_{gap}(GaP) + (1-x-y)E_{gap}(InP) \quad (2)$$

Table 1
The selected alloy configurations with ordering in the [1 1 1] directions. Only the positions of the cations are listed (the position of P atoms are shifted by (0.25, 0.25, 0.25) from the cation positions). The lattice vectors and the cation positions are in the Cartesian coordinates in the unit of lattice constant.

Alloy configuration	Lattice vector	Cation position	Alloy ordering
I	$(-0.5, 0.5, 1)$ $(-0.5, 1, 0.5)$ $(-1, 0.5, 0.5)$	Ga: $(-2, 2, 2)$ In: $(-1, 1, 1)$	$(GaP)_1\|(InP)_1$
II	$(-1.5, 1, 1.5)$ $(-1, 1.5, 1.5)$ $(-1.5, 1.5, 1)$	Ga: $(-1, 1, 1)$, $(-4, 4, 4)$ In: $(-2, 2, 2)$, $(-3, 3, 3)$	$(GaP)_2\|(InP)_2$
IIIa	$(-0.5, 0, -0.5)$ $(0, -0.5, 0.5)$ $(-2, 2, 2)$	Ga: $(-0.5, 0, 0.5)$, $(-1, 0.5, 0.5)$, $(-2.5, 1.5, 2)$ In: $(-1.5, 0.5, 1)$, $(-1.5, 1, 1.5)$, $(-2, 1.5, 1.5)$	$(GaP)_3\|(InP)_3$
IIIb	$(-0.5, 0, -0.5)$ $(0, -0.5, 0.5)$ $(-2, 2, 2)$	Ga: $(-0.5, 0, 0.5)$, $(-1.5, 0.5, 1)$, $(-2.5, 1.5, 2)$ In: $(-1, 0.5, 0.5)$, $(-1.5, 1, 1.5)$, $(-2, 1.5, 1.5)$	$(GaP)_1\|(InP)_1\|(GaP)_2\|(InP)_2$
IV	$(-2.5, 2.5, 3)$ $(-2.5, 3, 2.5)$ $(-3, 2.5, 2.5)$	Ga: $(-1, 1, 1)$, $(-3, 3, 3)$, $(-6, 6, 6)$, $(-8, 8, 8)$ In: $(-2, 2, 2)$, $(-4, 4, 4)$, $(-5, 5, 5)$, $(-7, 7, 7)$	$(GaP)_4\|(InP)_4$

Table 2
The calculated bandgap deformation coefficients and the interaction potential V_L for the alloy configurations in Table 1. The values in the parentheses are the experimental values of the coefficients reported in Ref. [41].

Configuration	$E(0)$ (eV)		α (meV/GPa)	β (meV/GPa^2)	V_L (eV)
InP	E_Γ = 0.525		74.1	−1.71	–
	E_L = 1.362		34.7	−0.80	
GaP	E_Γ = 1.822		89.7	−1.44	–
	E_L = 1.616		34.9	−0.62	
Disordered	E_Γ = 1.173		81.9 (92)	−1.57 (−3.3)	–
Ga$_{0.5}$In$_{0.5}$P	E_L = 1.489		34.8 (43)	−0.71	
I	E_- = 0.625		57.3	−1.47	0.71
II	E_- = 0.708		65.8	−1.70	0.60
IIIa	E_- = 0.762		55.9	−0.80	0.56
IIIb	E_- = 0.657		58.9	−1.95	0.68
IV	E_- = 0.662		50.3	−3.14	0.67

where $E_{\text{gap}}(\text{AlP})$, $E_{\text{gap}}(\text{GaP})$, and $E_{\text{gap}}(\text{InP})$ are the bandgaps of AlP, GaP, and InP, respectively. These bandgap values from EPM calculation along with the corresponding experimental values are given in Ref. [24] (Table 2). The convergence of bandgap range is studied by calculating the possible range of bandgaps as the cell size increased. Because the possible alloy composition of each cell-size is discrete in the composition space, a third-degree polynomial function of the form

$$\Delta E_{\text{gap}} = a + bx + cy + dx^2 + ey^2 + fxy + gx^3 + hy^3 + ixy^2 + jx^2y \tag{3}$$

is used to fit the calculated bandgap range by the least square method to generate fine-mesh data points for the contour plots. The contour plots of bandgap range for different N_{max} used are shown in Fig. 2. Note that the bandgap range at all three vertices are zero because there is only one possible configuration at those points.

3. Results and discussion

The ordering in the crystal structure induces the band interactions that can lower the bandgap. Because a larger cell size provides more degree of freedom of ordering, new configurations with lower bandgaps are expected as the cell size used in DEM is increased. The lowering of the minimum bandgap leads to the wider possible bandgap range. However, the range of the bandgaps is expected to converged (within a reasonable tolerance) with the cell size. The calculated bandgap range for each limited cell size as a function of alloy composition is shown in Fig. 2. We can see that the bandgap range is quite large (up to 0.8 eV) for the compositions near the middle of the composition space (slightly shifted toward the low Al composition side). The bandgap range is reduced as we move toward the vertices and goes to zero at the vertices. By visual observation, we can already see that the contour plots of the bandgap range for N_{max} = 5 and above are quite similar. The polynomial function for the contour plot of the largest cell size (N_{max} = 8) is given by

$$\Delta E_{\text{gap}} = 2.34x + 4.12y - 3.18x^2 - 6.98y^2 - 5.27xy + 0.84x^3 + 2.85y^3 + 2.36xy^2 + 1.32x^2y \tag{4}$$

where the bandgap reduction (ΔE_{gap}) is in eV and x, y are the alloy compositions of Al$_x$Ga$_y$In$_{1-x-y}$P.

To qualitatively determine the convergence of the bandgap ranges as a function of cell size, we compute the difference between the bandgap ranges of each N_{max} with those of the largest cell used (N_{max} = 8). This is done by calculating the average root-mean-square of the difference (Δ). The average is done over the entire composition space. First, a 200×200 uniform mesh in the composition space is created. Then, at each point in alloying composition (total of 20,301 points), the bandgap range for each N_{max} is calculated from the polynomial fitted function. The root-mean-
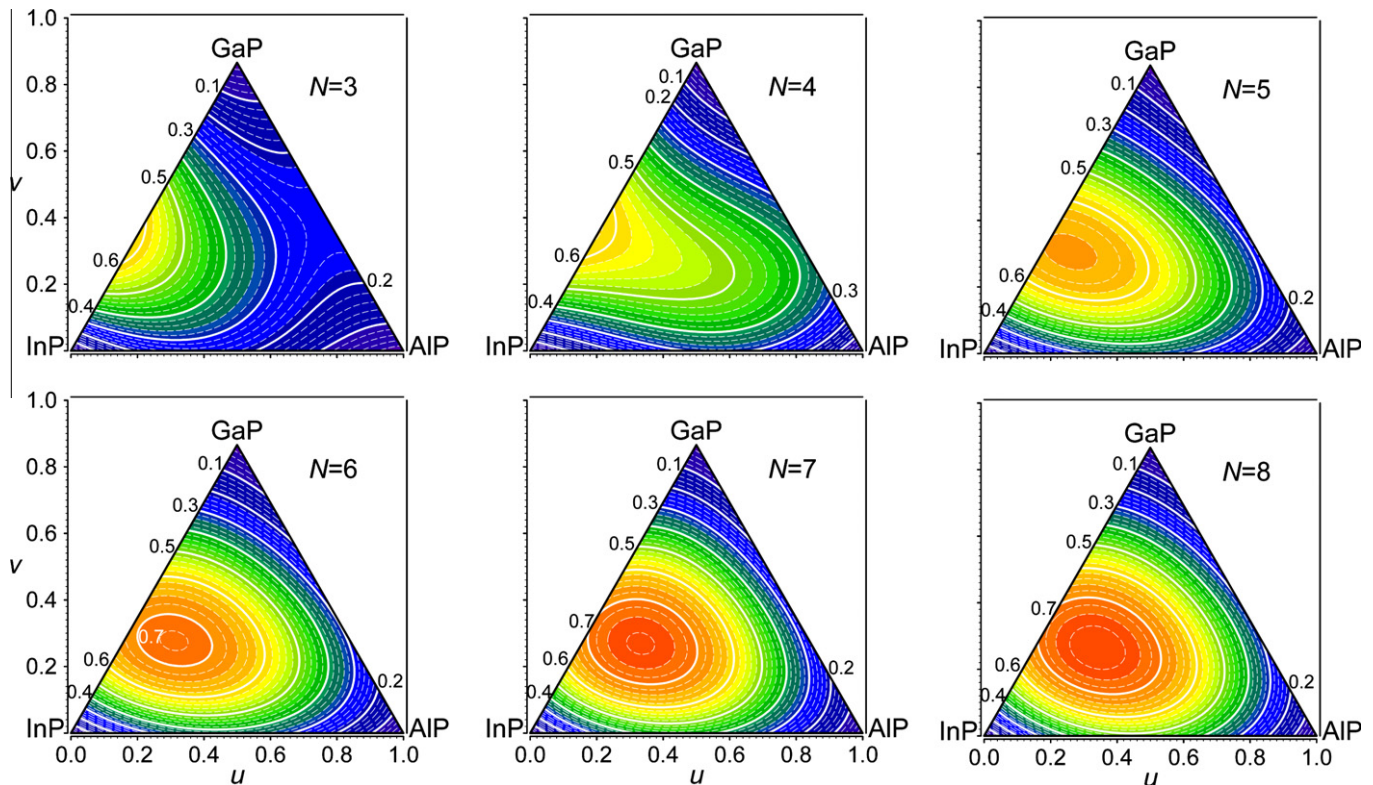

Fig. 2. The contour plots of the calculated bandgap ranges of pseudoternary AlGaInP as a function of alloy compositions ($u = x + y/2$ and $v = \sqrt{3}y/2$). Each figure shows the results of the calculation with a different N_{max}. Note that a third-degree polynomial function is used to fit to the calculated data, in order to generate the fine-mesh data for the plots.
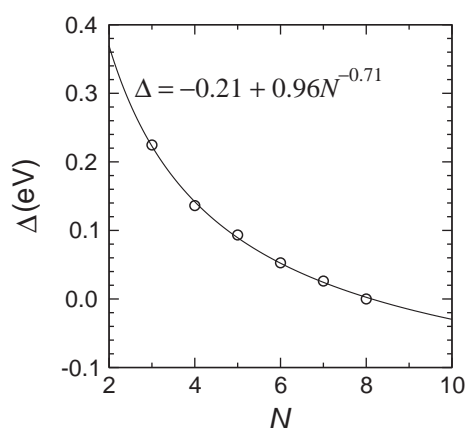
Fig. 3. The root-mean-square difference (Δ) of bandgap range for each cell sizes ($N_{\max}$), with respect to $N_{\max}$ = 8. The curve represents the fit to the data.

square of the difference (between that of interested $N_{\max}$ and that of $N_{\max}$ = 8) in bandgap range is calculated and the average (Δ) over all mesh points are calculated. In Fig. 3, Δ as a function of $N_{\max}$ along with the function (in the form of $\Delta = a + bN^c$) is shown. It is found that Δ started to converge (with the tolerant of ~0.1 eV referenced to the $N_{\max}$ = 8 calculation) already at the cell size containing 5 cation atoms.

For pseudobinary alloys, AlGaP tends to have a rather large bandgap range of ~0.5 eV (see Fig. 2 for $N_{\max}$ = 8). AlInP has an even larger bandgap range of ~0.6 eV. For GaInP, it is interesting that the large bandgap range of ~0.6 eV is already observed at a small cell $N_{\max}$ = 3. This indicates that an ordering that can significantly reduce the bandgap of GaInP alloy can be represented by a small cell size. It has been found that the ordering in [1 1 1] direction of the CuPt ordered structure can give a large bandgap reduction [9,24]. The crystal parameters of CuPt ordered structure consisting of 2 cations/cell is shown in Table 1. In general, we can expect more degree of freedom in ordering to give an increased bandgap range. As a result, the smaller bandgap configuration would occur in the large cell size. However, for this special case, the bandgap of GaInP reduction of CuPt ordered structure provides the minimum bandgap value for the 50% alloy ($Ga_{0.5}In_{0.5}P$). This occurs because the conduction state that folded onto the Γ point (from the L point) interacts strongly with the conduction band minimum at the Γ point. Because the folding that causes this interaction already took place in the small cell, increasing cell size (allow more flexibility of orderings) does not make the interaction stronger for this particular case. As a result, the bandgap range at this composition converges at a small cell size. To further investigate the band interaction for this particular case, first-principles calculations are performed.

We employed first-principles calculations to examine the electronic structures of several selected configurations ordering in the [1 1 1] direction. The crystal parameters and atomic coordinates of these configurations are shown in Table 1. The calculations were performed by the ultrasoft pseudopotential approach with the projector augmented wave (PAW) method [34,35] and a plane wave basis set (324 eV cutoff) as implemented in the VASP code [36–38]. The Γ-centered Monkhorst–Pack k-mesh is used for Brillouin zone integration.

To study the bandgap change as a function of pressure, for each of alloy configurations, bandgap at the Γ point is calculated at different volume (V). To relate the volume to the applied pressure, the total energy as a function of volume is fitted with the Rose equation of states [39]. For each configuration, the pressure dependence of bandgap (at Γ) can be described by the relationship

$E(P) = E(0) + \alpha P + \beta P^2$. The parameters α and β are obtained by the least square fit to the calculated (first-principles) results and tabulated in Table 2. The ordering in the [1 1 1] direction causes the conduction band minimum at L to fold to Γ (called L_{c1}). The nonlinearity of $E(P)$ is a result of the repulsion between the conduction states at Γ and L_{c1} [40]. Because the conduction state is pushed down, the bandgap in this configuration is reduced [25,26]. To study the effects of the interactions, the bandgaps of the ordered structures are compared with that obtained from the Vegard's rule (the linear interpolation between the bandgaps of parent compounds) which represents the case of completely disordered alloy. In Table 2, the bandgap of the disordered alloy is calculated by averaging the bandgaps of parent compounds (GaP and InP). The interaction between Γ and L_{c1} can be described by the first order perturbation theory. The perturbed energies of Γ and L_{c1} can be expressed as [41],

$$E_{\pm} = 1/2 \left[(E_L + E_\Gamma) \pm \sqrt{(E_L - E_\Gamma)^2 + 4V_L^2} \right] \qquad (5)$$

where E_+ and E_- are the energies of perturbed L_{c1} and Γ states. E_L and E_Γ are the energies of unperturbed Γ and L (obtained by Vegard's rule). If we assumed that the interaction potential (V_L) does not depend on the pressure, V_L can be calculated by fitting each sets of E_-, E_L, and E_Γ to Eq. (5). The values of V_L obtained by the least squares fit are shown in Table 2. The obtained values of V_L clearly show that GaP/InP monolayer superlattice (structure I with $N = 2$) has the strongest interaction (V_L = 0.71 eV). As a result, the configuration has the largest bandgap reduction among GaInP alloys [42].

4. Conclusions

The convergence of the bandgap range of AlGaInP alloys with respect to the cell size used in the direct enumeration method (DEM) is studied. By directly calculating a large number of alloy configurations, the bandgap range as a function of alloy compositions are determined by DEM using various unit cell size ($N_{\max}$ = 2–8). It is found that it is sufficient to use the cell size with 5 cation atoms ($N_{\max}$ = 5). The bandgap range of AlGaInP alloy is reported (in the form of a polynomial function). It is found that the bandgap range is large (~0.8 eV) for the compositions near the middle of the composition space (slightly shifted toward the low Al composition side). In addition to the convergence study, the source of the bandgap reduction of the alloy in the [1 1 1] superlattice configurations are investigated. It is found that the superlattice in this direction has strong interactions between the Γ and the folded L states and the GaP/InP monolayer superlattice has the strong interaction among studied configurations.

Acknowledgements

References

[1] A.S. Dissanayake, S.X. Huang, H.X. Jiang, J.Y. Lin, Phys. Rev. B 44 (1991) 13343.
[2] H.X. Jiang, G. Brown, J.Y. Lin, J. Appl. Phys. 69 (1991) 6701.
[3] S. Krishnamurthy, A. Sher, M. Madou, A.B. Chen, J. Appl. Phys. 64 (1988) 1530.
[4] M.F. Ling, D.J. Miller, Phys. Rev. B 38 (1988) 6113.
[5] L. Vegard, Z. Phys. 5 (1921) 17.
[6] L. Vegard, Z. Kristallogr. 67 (1928) 239.
[7] A. Ebina, Y. Sato, T. Takahashi, Phys. Rev. Lett. 32 (1974) 1366.
[8] A. Franceschetti, A. Zunger, Nature 402 (1999) 60.

[9] K. Kim, P.A. Graf, W.B. Jones, J. Comput. Phys. 208 (2005) 735.
[10] L.G. Ferreira, S.H. Wei, A. Zunger, Int. J. High Perform. Comput. Appl. 5 (1991) 34.
[11] P.A. Graf, K. Kim, W.B. Jones, G.L.W. Hart, Appl. Phys. Lett. 87 (2005) 243111.
[12] J. Rutherford, Acta Crystallogr. A 51 (1995) 672.
[13] J. Rutherford, Acta Crystallogr. A 48 (1992) 500.
[14] L.-W. Wang, A. Zunger, J. Chem. Phys. 100 (1994) 2394.
[15] A. Canning, L.-W. Wang, A. Williamson, A. Zunger, J. Comput. Phys. 160 (2000) 29.
[16] T. Mattila, L.W. Wang, A. Zunger, Phys. Rev. B 59 (1999) 15270.
[17] K.A. Mäder, A. Zunger, Phys. Rev. B 50 (1994) 17393.
[18] G.L.W. Hart, R.W. Forcade, Phys. Rev. B 77 (2008) 224115.
[19] G.L.W. Hart, R.W. Forcade, Phys. Rev. B 80 (2009) 014120.
[20] K.A. Mäder, A. Zunger, Phys. Rev. B 51 (1995) 10462.
[21] K.A. Mäder, L.-W. Wang, A. Zunger, Phys. Rev. Lett. 74 (1995) 2555.
[22] A. Franceschetti, A. Zunger, Phys. Rev. B 52 (1995) 14664.
[23] J. Kim, L.-W. Wang, A. Zunger, Phys. Rev. B 56 (1997) R15541.
[24] S. Jungthawan, S. Limpijumnong, R. Collins, K. Kim, P.A. Graf, J.A. Turner, J. Appl. Phys. 105 (2009) 123531.
[25] S.H. Wei, A. Zunger, Appl. Phys. Lett. 56 (1990) 662.
[26] L.C. Su, I.H. Ho, N. Kobayashi, G.B. Stringfellow, J. Cryst. Growth 145 (1994) 140.
[27] W. Feller, An Introduction to Probability Theory and its Applications, vol. 1, Wiley, New York, 1968.
[28] A. vandeWalle, M. Asta, G. Ceder, CALPHAD J. 26 (2002) 539.
[29] A. van de Walle, G. Ceder, J. Phase Equilib. Diff. 23 (2002) 348.
[30] P.N. Keating, Phys. Rev. 145 (1966) 637.
[31] R.M. Martin, Phys. Rev. B 1 (1970) 4005.
[32] J.L. Martins, A. Zunger, Phys. Rev. B 30 (1984) 6217.
[33] M.C. Schabel, J.L. Martins, Phys. Rev. B 43 (1991) 11873.
[34] P.E. Blöchl, Phys. Rev. B 50 (1994) 17953.
[35] G. Kresse, D. Joubert, Phys. Rev. B 59 (1999) 1758.
[36] G. Kresse, J. Furthmüller, Comput. Mater. Sci. 6 (1996) 15.
[37] G. Kresse, J. Furthmüller, Phys. Rev. B 54 (1996) 11169.
[38] G. Kresse, J. Hafner, J. Phys.: Condens. Matter 6 (1994) 8245.
[39] J.H. Rose, J.R. Smith, F. Guinea, J. Ferrante, Phys. Rev. B 29 (1984) 2963.
[40] T. Kobayashi, M. Ohtsuji, S. Deol, J. Appl. Phys. 74 (1993) 2752.
[41] J. Dong, Z. Wang, D. Lu, X. Liu, X. Li, D. Sun, Z. Wang, M. Kong, G. Li, Appl. Phys. Lett. 68 (1996) 1711.
[42] S.R. Kurtz, J. Appl. Phys. 74 (1993) 4130.

Hydrogen doping in indium oxide: An *ab initio* study

Sukit Limpijumnong,[1,2,3] Pakpoom Reunchan,[1,2] Anderson Janotti,[1] and Chris G. Van de Walle[1]

[1]*Materials Department, University of California, Santa Barbara, California 93106-5050, USA*

[2]*School of Physics, Suranaree University of Technology and Synchrotron Light Research Institute, Nakhon Ratchasima 30000, Thailand*

[3]*Thailand Center of Excellence in Physics (ThEP Center), Commission on Higher Education, Bangkok 10400, Thailand*

First-principles density-functional theory is employed to investigate the role of hydrogen impurities in In_2O_3. We find that both interstitial hydrogen (H_i) and substitutional hydrogen (H_O) act as shallow donors. Our results support recent experiments by Koida *et al.* [Jpn. J. Appl. Phys. **46**, L685 (2007)], which found hydrogen-doped In_2O_3 to be a good candidate for transparent conducting films.

Indium oxide (In_2O_3) is one of the few transparent materials that can be doped to a very high carrier concentration without significantly degrading their transparencies. The most widely used transparent conductor is tin-doped In_2O_3, known as indium tin oxide (ITO), which is used as a transparent electrode for optoelectronic devices such as solar cells and light emitting diodes. Recently, Koida *et al.*[1] showed that hydrogen-doped In_2O_3 can have mobility exceeding 100 cm^2/V s at carrier densities of $\sim 10^{20}$ cm^{-3} and exhibits good transparency even at near-infrared (NIR) wavelengths. Hydrogen-doped In_2O_3 is, therefore, a promising material to replace or improve upon ITO for applications in optoelectronic devices such as solar cells or photodetectors, in particular, when sensitivity in the NIR region is required.

In this Brief Report, we provide a detailed first-principles study of H in In_2O_3. In most semiconductors H_i is amphoteric, acting as a donor in *p*-type samples and as an acceptor in *n*-type samples. If H_i is amphoteric, it can never be the cause of conductivity since it self-compensates. There are exceptions though. For example, H_i was proposed, based on first-principles calculations,[2] to act exclusively as a donor in ZnO, a prediction which was soon confirmed by experiments.[3] Hydrogen is thus one of the causes of unintentional *n*-type conductivity in ZnO. In the present work we find that H_i is also a shallow donor in In_2O_3, and can, therefore, also be the cause of *n*-type conductivity. In addition, H atoms can also occupy substitutional oxygen sites (H_O) and also act exclusively as donors in this configuration. Substitutional hydrogen was recently described in terms of a multicenter bond and found to be stable in a number of oxides and some nitride materials.[4–6] In order to explore the stability of H_O, we also performed calculations for oxygen vacancies (V_O) in In_2O_3. Our findings confirm that hydrogen acts as the source of *n*-type conductivity in In_2O_3.

In_2O_3 has a fairly complicated crystal structure called *bixbyite* [space group $T_h^7 (Ia\bar{3})$] with 80 atoms in a conventional cell and 40 atoms in the primitive unit cell. Its large primitive unit cell, compared with conventional semiconductors (two atoms per cell for Si or GaAs), rendered first-principles calculations of this material prohibitively demanding in the past. Only in the last decade have first-principles calculations for In_2O_3 been attempted, starting with a linear muffin tin orbital method with atomic sphere approximations with a small basis set for an unrelaxed experimental structure by Odaka *et al.*,[7] followed by a more advanced full-potential linear muffin-tin-orbital calculation that included volume relaxation by Mryasov and Freeman.[8] Based on their investigation of the band structure, Mryasov and Freeman attributed the coexistence of conductivity and transparency to the unique characteristics of the conduction-band separation in In_2O_3. More recently, Medvedeva[9] used the full-potential linearized augmented plane-wave method and allowed full structural relaxations to calculate the band structures. To date, only a few impurities in In_2O_3 have been studied by first-principles calculations.[8–11]

We perform first-principles calculations using density-functional theory (DFT) within the local-density approximation (LDA), as implemented in the Vienna *ab initio* simulation package.[12] Electron-ion interactions are treated using projector augmented wave potentials.[13] The electron wave functions are described using a plane-wave basis set with an energy cutoff of 400 eV. Since In 4*d* electrons are not fully localized near the core and can play a role in the crystal bonding, they are treated as valence electrons and allowed to relax during the self-consistent calculations. A shifted $2 \times 2 \times 2$ *k*-point sampling based on the Monkhorst-Pack scheme[14] is employed for the Brillouin-zone integration. The calculated lattice constant of 10.073 Å is in good agreement with the experimental value of 10.117 Å.[15] The calculated band gap (1.17 eV) is much smaller than the experimental value due to the well-known DFT problem. In the past, the experimental band gap of In_2O_3 was widely believed to be 3.6 eV.[16] Only recently has the actual value of the band gap been established, at 2.67 eV for molecular-beam epitaxy (MBE)-grown samples[17] and a slightly higher value at 2.89 eV for rf magnetron sputtered samples.[18] We can overcome the band-gap underestimation inherent in LDA by performing LDA$+U$ calculations, allowing us to investigate the changes in the transition levels and formation energies as the band gap is increased. This approach has been successfully applied in the study of H in other oxides and nitrides.[4–6,19] To calculate H in various configurations, we follow a supercell approach with a conventional unit cell of 80 atoms as the supercell and the lattice constant fixed at the calculated bulk value (10.073 Å). All atoms are allowed to relax during the calculations. The formation energy of H_i^q ($q=-$, 0, or +) is defined as[20,21]

$$E^f(\mathrm{H}_i^q) = E_{\mathrm{tot}}(\mathrm{H}_i^q) - E_{\mathrm{tot}}(\mathrm{bulk}) - \mu_\mathrm{H} + qE_F, \qquad (1)$$

where $E_{\mathrm{tot}}(\mathrm{H}_i^q)$ is the total energy of the supercell containing H_i in charge state q, and $E_{\mathrm{tot}}(\mathrm{bulk})$ is the total energy of the perfect crystal in the same supercell. For a charged H_i ($q \neq 0$), electrons are exchanged with a reservoir with energy E_F, the Fermi energy of the system. μ_H is the hydrogen chemical potential, i.e., the energy of the reservoir with which H atoms are exchanged. We fixed the value of μ_H to half of the calculated energy of a free H_2 molecule. The formation energies of V_O and H_O are defined as

$$E^f(V_\mathrm{O}^q) = E_{\mathrm{tot}}(V_\mathrm{O}^q) - E_{\mathrm{tot}}(\mathrm{bulk}) + \mu_\mathrm{O} + qE_F, \qquad (2)$$

and

$$E^f(\mathrm{H}_\mathrm{O}^q) = E_{\mathrm{tot}}(\mathrm{H}_\mathrm{O}^q) - E_{\mathrm{tot}}(\mathrm{bulk}) + \mu_\mathrm{O} - \mu_\mathrm{H} + qE_F, \qquad (3)$$

where $E_{\mathrm{tot}}(V_\mathrm{O}^q)$ is the total energy of the supercell with one O removed, and $E_{\mathrm{tot}}(\mathrm{H}_\mathrm{O}^q)$ is the total energy of the supercell with one H substituted for O. For the purposes of presenting our results we assumed In-rich growth conditions, i.e., μ_In is fixed at the energy per atom of In metal, and μ_O is fixed at 3.66 eV below the energy of half an O_2 molecule, based on the calculated heat of formation of $\mathrm{In}_2\mathrm{O}_3$ (10.99 eV/f.u.). Values for other growth conditions can easily be obtained by referring back to Eqs. (2) and (3).

By symmetry, $\mathrm{In}_2\mathrm{O}_3$ in the bixbyite structure has two inequivalent In sites (8*b* and 24*d* in Wyckoff notation) and all oxygen sites are equivalent.[15] A quarter of all In atoms (labeled In1) occupy the 8*b* positions while the remaining three quarters (labeled In2) occupy the 24*d* positions. Both types of In atoms have a sixfold coordination with their O neighbors. The calculated local structures of In1 and In2 atoms are shown in Figs. 1(a) and 1(b), respectively. The local structure of In1 atom is quite symmetrical. All six In-O bonds are equivalent with a bond distance of 0.2% smaller than the average value of all In-O bonds. It has a shear distorted octahedral coordination as shown in Fig. 1(a). If all the bond angles were 90°, the structure would be a perfect octahedron. The In2 configuration is less symmetrical, as shown in Fig. 1(b). For In2, the six In-O bonds can be divided into three groups of two equivalent In-O bonds. The major difference between In1 and In2 is that In1 and its O neighbors form three sets of linear O-In-O bonds whereas no linear O-In-O bonds occur for In2. For the local structure of oxygen, each O atom forms distorted tetrahedral bonds with its neighboring In atoms (one In1 and three In2) as shown in Fig. 1(c). These four In-O bonds are inequivalent and have bond distances that differ from the average bond distance ($d_{\mathrm{In-O}}^{\mathrm{calc.}}$ =2.169 Å) by +2.0%, +0.5%, −0.2%, and −2.3%.

We have calculated H_i in three charge states: +, neutral, and −. Similar to other oxides[2,22] and nitrides,[20,23] H_i^+ prefers sites near the anions. In other oxides and nitrides, H_i^+ exhibits local minima at the bond center (BC) and anion antibonding (AB_O) sites. For $\mathrm{In}_2\mathrm{O}_3$ there are four inequivalent BC and four inequivalent AB_O sites, as illustrated in Fig. 1(d). We find that H_i^+ is not stable at the BC sites. It is spontaneously pushed away from the site and moves significantly off-axis (similar to the $\mathrm{OA}_\parallel$ site in Ref. 24). Indeed, two of the BC sites lead to configurations that are essentially the same as
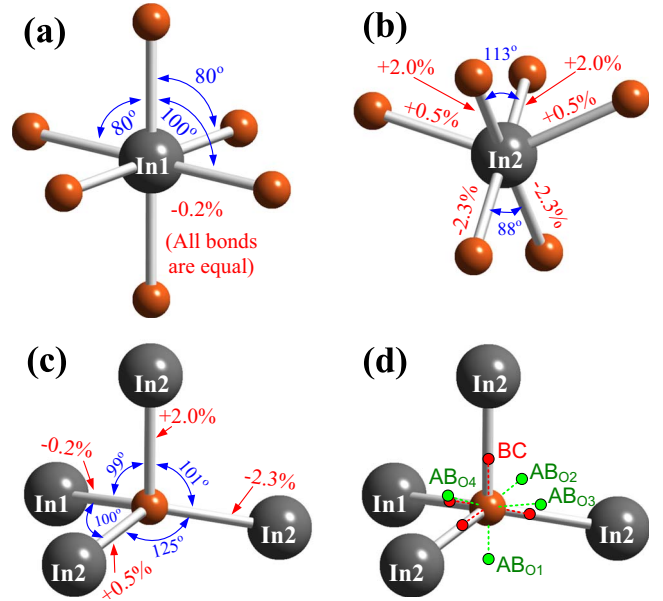

FIG. 1. (Color online) Schematic illustration of the coordination around In and O atoms in $\mathrm{In}_2\mathrm{O}_3$. The percentage numbers indicate the differences in bond length compared to the average of all In-O bonds (calculated value=2.169 Å). There are two In inequivalent sites, both surrounded by six O atoms. All O sites are equivalent and surrounded by four In atoms. (a) The 8*b* In site, (b) the 24*d* In site, (c) the O site, and (d) the possible sites for interstitial H.

the AB_O3 and AB_O4 sites. The calculated energies for H_i^+ at the four inequivalent AB_O sites are listed in Table I. It has been previously shown for the cases of ZnO (Ref. 2) and III-Nitrides[20,23] that when H occupies the AB site, the corresponding host-atom bond is significantly extended. We observe the same phenomenon in $\mathrm{In}_2\mathrm{O}_3$. This may explain why

TABLE I. Calculated formation energies E^f for H defects and O vacancies in $\mathrm{In}_2\mathrm{O}_3$. For some defects with an occupied gap state, a corrected value of E^f based on LDA+U and extrapolation (Ref. 19) (see text) is presented in square brackets. For charged defects we take the Fermi energy at the VBM. Equilibrium with bulk In metal (In-rich conditions) and with H_2 molecules at $T=0$ is assumed. Bond lengths for O-H bonds in the antibonding configurations of H_i^+ are also listed.

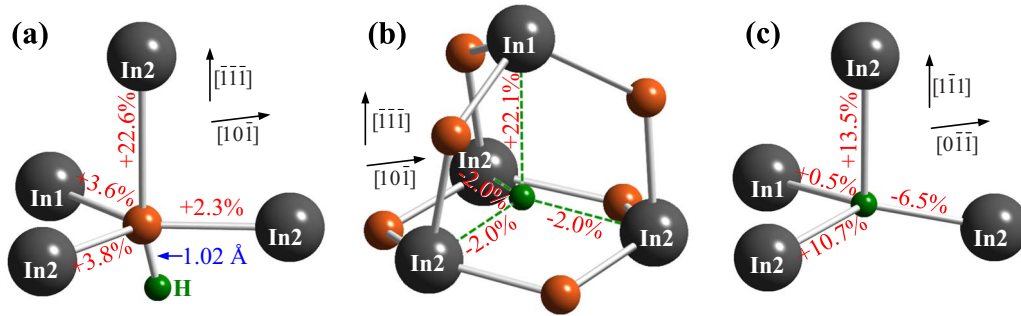| Defect	Location	E^f (eV)	$d_{\mathrm{O\text{-}H}}$ (Å)
H_i^+	AB_O1	−2.09	1.026
H_i^+	AB_O2	−1.66	1.015
H_i^+	AB_O3	−1.34	0.995
H_i^+	AB_O4	−1.35	0.996
H_i^0	16*c*	2.43	
H_i^-	16*c*	3.41 [4.27]	
H_i^-	8*a*	4.33	
H_O^+	O site	−1.40	
V_O^{2+}	O site	−2.68	
V_O^+	O site	−0.84[0.01]	
V_O^0	O site	0.96 [2.30]	

FIG. 2. (Color online) Schematic illustration of H defects in In_2O_3. H_i^+ at the AB_{O1} site in (a), H_i^- at the $16c$ site in (b), and H_O^+ in (c).

the AB_{O1} site is the preferred site for H_i^+, since its corresponding In-O bond is initially the longest. H_i^+ at the AB_{O1} site is lower in energy than the other (metastable) sites by at least 0.4 eV, rendering the occupation of those other sites negligible at reasonable temperatures. The fully relaxed geometry of H_i^+ at the AB_{O1} site is shown in Fig. 2(a). The O-H bond distances (d_{O-H}), as shown in Table I, are slightly longer than the O-H bond in H_2O. A similar trend was observed for the case of H_i in ZnO.[25]

In the negative charge state, H_i prefers interstitial sites closer to the cations.[20,23] In the bixbyite crystal, two such interstitial sites exist, which we will refer to as $8a$ and $16c$ following their Wyckoff notations.[15] We find that H_i^- and H_i^0 are stable at the $16c$ site with the single-electron level at ~ 1 eV above the valence-band maximum (VBM); the corresponding defect state is spatially localized on the H atom. The relaxed geometry of H_i^- at the $16c$ site is shown in Fig. 2(b). At the $8a$ site H_i^- is metastable with a formation energy that is higher by 0.9 eV than at the $16c$ site.

The formation energies for H_i^- and H_i^0 are shown in Table I, and a plot of formation energy as a function of Fermi-level position for all three charge states is shown in Fig. 3. Based on the LDA results, H_i is a negative-U defect (the neutral
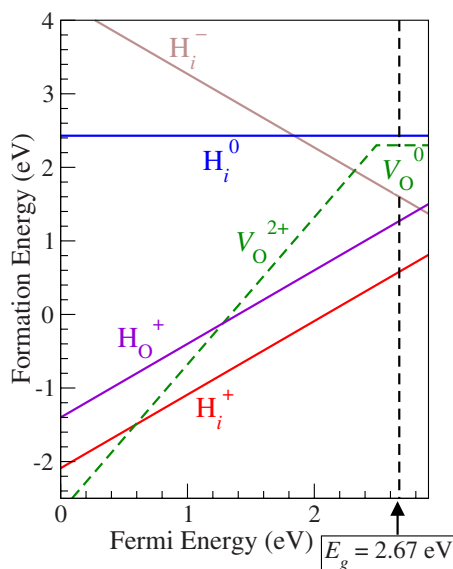

FIG. 3. (Color online) Calculated formation energies of hydrogen defects and oxygen vacancies in In_2O_3 as a function of Fermi energy. In-rich conditions are assumed.

charge state is never stable). H_i is stable in the + charge state for the range of Fermi energies from the VBM up to E_F ~ 2.75 eV above the VBM. Since the band gap of MBE-grown In_2O_3 has been reported to be 2.67 eV,[17] we can conclude that hydrogen behaves exclusively as a donor for Fermi levels within this gap.

The bare LDA results show that the +/− transition level (the Fermi-level value for which H_i^+ and H_i^- have equal formation energies) occurs at 2.75 eV above the VBM. Since this value is only slightly above the reported gap of 2.67 eV,[17] and since there may still be some uncertainty in this band-gap value (due to the band-gap renormalization and the potential residual strain in the thin films), it is worthwhile to obtain a more reliable value for the +/− transition level by going beyond the bare LDA results. LDA underestimates the band gap and, therefore, also the energy of H_i^-, which has an occupied state in the band gap. Correction of the band gap may shift this state upward and hence increase the energy of H_i^-. To estimate this correction, we performed LDA+U calculations as described in Ref. 19 with $U=4$ eV for the In $4d$ states. The LDA+U calculation for bulk In_2O_3 produces a slightly reduced lattice constant (by 1.4%) and raises the band gap by 0.47 eV compared to LDA. To obtain a complete band-gap correction, further extrapolation is needed.[19] Based on the calculations of bulk band gap, we can see that the correction has to be scaled up by $(2.67-1.17)/0.47$ $=3.19$ times to get the full band-gap correction. The LDA+U calculations of H_i^- raise the +/− level by 0.14 eV; therefore, the corrected transition level would occur at 2.75 $+0.14 \times 3.19 = 3.20$ eV, which is well above the conduction-band minimum (CBM). The corrected formation energy of H_i^- is shown in Fig. 3.

In addition to H_i, we have studied H substitution on the O site, finding that H_O is also exclusively a donor. It always exists in + charge state without any defect level inside the band gap. The fully relaxed geometry of H_O^+ is shown in Fig. 2(c), and the calculated formation energy of H_O is included in Table I and plotted in Fig. 3. The formation energy of H_O is slightly higher than that of H_i, but low enough to lead to a significant incorporation of substitutional hydrogen. We also performed calculations for oxygen vacancies in order to investigate the stability of H_O with respect to the dissociation into H_i and V_O. We find that V_O is a deep donor in In_2O_3. Our calculations show that V_O is stable in two charge states: 2+ and neutral; the + charge state is never stable. We again used the LDA+U extrapolation scheme; formation energies based on LDA and LDA+U are listed in Table I, and the corrected

formation energies are shown in Fig. 3. Our calculated 2 +/0 level, referenced to the VBM, is in good agreement with that calculated by Lany and Zunger.[26] (Note that in Lany and Zunger's work, the transition level for V_O appears to be much deeper in the gap because they used a larger In_2O_3 bandgap of 3.50 eV.) The binding energy between V_O and H_i to form H_O can be calculated from the formation energies of the three defects, shown in Fig. 3. Under n-type conditions the binding energy is 1.82 eV, a large value which is indicative of the stability of the substitutional hydrogen.

Recently, Koida *et al.*[1] prepared and characterized rf magnetron sputtered In_2O_3 samples doped with various concentrations of hydrogen. They reported an optimized carrier density of 3×10^{20} cm^{-3} and mobility as high as 130 cm^2/V s for a sample doped with ~ 3 at. % of H. King *et al.*[27] performed muon spin rotation measurements to investigate the electrical behavior of hydrogen in In_2O_3. Their results indicate that hydrogen is a shallow donor, with the estimated +/− transition level at 0.6 eV above the conduction-band minimum.[27] These experimental results are consistent with our calculations, which indicate that both interstitial and substitutional hydrogen serve as donors in In_2O_3.

[1] T. Koida, H. Fujiwara, and M. Kondo, Jpn. J. Appl. Phys. **46**, L685 (2007).

[2] C. G. Van de Walle, Phys. Rev. Lett. **85**, 1012 (2000).

[3] D. M. Hofmann, A. Hofstaetter, F. Leiter, H. Zhou, F. Henecker, B. K. Meyer, S. B. Orlinskii, J. Schmidt, and P. G. Baranov, Phys. Rev. Lett. **88**, 045504 (2002).

[4] A. Janotti and C. G. Van de Walle, Nature Mater. **6**, 44 (2007).

[5] A. Janotti and C. G. Van de Walle, Appl. Phys. Lett. **92**, 032104 (2008).

[6] A. K. Singh, A. Janotti, M. Scheffler, and C. G. Van de Walle, Phys. Rev. Lett. **101**, 055502 (2008).

[7] H. Odaka, S. Iwata, N. Taga, S. Ohnishi, Y. Kaneta, and Y. Shigesato, Jpn. J. Appl. Phys. **36**, 5551 (1997).

[8] O. N. Mryasov and A. J. Freeman, Phys. Rev. B **64**, 233111 (2001).

[9] J. E. Medvedeva, Phys. Rev. Lett. **97**, 086401 (2006).

[10] H. Odaka, Y. Shigesato, T. Murakami, and S. Iwata, Jpn. J. Appl. Phys. **40**, 3231 (2001).

[11] O. Warschkow, D. E. Ellis, G. B. Gonzalez, and T. O. Mason, J. Am. Ceram. Soc. **86**, 1700 (2003).

[12] G. Kresse and J. Furthmüller, Comput. Mater. Sci. **6**, 15 (1996).

[13] P. E. Blöchl, Phys. Rev. B **50**, 17953 (1994).

[14] H. J. Monkhorst and J. D. Pack, Phys. Rev. B **13**, 5188 (1976).

[15] M. Marezio, Acta Crystallogr. **20**, 723 (1966).

[16] A. Klein, Appl. Phys. Lett. **77**, 2009 (2000).

[17] A. Bourlange, D. J. Payne, R. G. Egdell, J. S. Foord, P. P. Edwards, M. O. Jones, A. Schertel, P. J. Dobson, and J. L. Hutchison, Appl. Phys. Lett. **92**, 092117 (2008).

[18] A. Walsh, J. L. F. Da Silva, S.-H. Wei, C. Korber, A. Klein, L. F. J. Piper, A. DeMasi, K. E. Smith, G. Panaccione, P. Torelli, D. J. Payne, A. Bourlange, and R. G. Egdell, Phys. Rev. Lett. **100**, 167402 (2008).

[19] A. Janotti and C. G. Van de Walle, Phys. Rev. B **76**, 165202 (2007).

[20] S. Limpijumnong and C. G. Van de Walle, Phys. Status Solidi B **228**, 303 (2001).

[21] C. G. Van de Walle, S. Limpijumnong, and J. Neugebauer, Phys. Rev. B **63**, 245205 (2001).

[22] S. Limpijumnong and S. B. Zhang, Appl. Phys. Lett. **86**, 151910 (2005).

[23] S. Limpijumnong, J. E. Northrup, and C. G. Van de Walle, Phys. Rev. B **68**, 075206 (2003).

[24] S. Limpijumnong, J. E. Northrup, and C. G. Van de Walle, Phys. Rev. Lett. **87**, 205505 (2001).

[25] S. Limpijumnong, *Hydrogen in Semiconductors*, edited by N. H. Nickel. M. D. McCluskey, and S. B. Zhang, MRS Symposia Proceedings No. 813 (Materials Research Society, Pittsburg, 2004) p. H3.6.1.

[26] S. Lany and A. Zunger, Phys. Rev. Lett. **98**, 045501 (2007).

[27] P. D. C. King, R. L. Lichti, Y. G. Celebi, J. M. Gil, R. C. Vilao, H. V. Alberto, J. Piroto Duarte, D. J. Payne, R. G. Egdell, I. McKenzie, C. F. McConville, S. F. J. Cox, and T. D. Veal, Phys. Rev. B **80**, 081201(R) (2009).